THESIS FOR THE DEGREE OF DOCTOR OF PHILOSOPHY

Strong Light-Matter Coupling: the Road from Conventional to Cavity-Free Polaritons

ADRIANA CANALES RAMOS

Department of Physics
CHALMERS UNIVERSITY OF TECHNOLOGY
Göteborg, Sweden, 2023

STRONG LIGHT-MATTER COUPLING: THE ROAD FROM CONVENTIONAL TO CAVITY-FREE POLARITONS

Adriana Canales Ramos
ISBN 978-91-7905-961-3

© Adriana Canales Ramos, 2023

Doktorsavhandlingar vid Chalmers tekniska högskola
Ny serie nr 5427
ISSN 0346-718X

Division of Nano- and Biophysics
Department of Physics
Chalmers University of Technology
SE-412 96 Göteborg
Sweden

Cover:
True-color image of the Fourier plane of the light reflected from a 67 nm thick MoS_2 *slab. This experimental Fourier plane image is used to obtain the angular reflection spectra, which shows that the unpatterned slab is polaritonic and perfectly absorbs light simultaneously.*

Printed in Sweden by
Chalmers digital printing
Chalmers Tekniska Högskola
Göteborg, Sweden, 2023

CHALMERS UNIVERSITY OF TECHNOLOGY

Department of Physics

Strong Light-Matter Coupling: the Road from Conventional to Cavity-Free Polaritons

Adriana Canales Ramos

Abstract

The interaction between light and matter is fundamental in perceiving and understanding the world. The interaction is typically weak, meaning light only perturbs matter without changing its properties. When photons interact strongly with material resonances caused by electronic or vibrational transitions, hybrid light-matter states called *polaritons* emerge. Polaritons have gained significant attention because of their potential to modify and manipulate material properties, such as conductivity, energy transport, photochemistry, and chemical reaction rates. Obtaining polaritons used to require meticulous design and fabrication of cavities, but recent efforts have aimed to simplify the process using metallic microcavities and open plasmonic cavities to expand their potential applications. Regardless of the type of cavity used, *conventional* polaritons rely on an external cavity, making them a rare occurrence.

This thesis aims to study and simplify the process of obtaining polaritons in theory and experiment. It begins with the extensively studied conventional polaritons obtained with metallic microcavities. The focus is on their asymmetric decay rates, a less-studied and puzzling property. Surprisingly, the asymmetry is found to be a more general effect than previously considered, occurring even in bulk polaritons. Next, instead of fabricating them, metallic microcavities are formed by the balance between Casimir and electrostatic forces in gold flakes present in the solution. These metallic microcavities then self-assemble and hybridize with the excitons in a 2D semiconductor. These microcavities can be tuned by altering the ionic concentration in the solution or through dynamic laser irradiation. Finally, the rest of the thesis is devoted to removing the necessity of an external cavity, leading to *cavity-free* polaritons. In this case, optical modes are sustained by the material's geometry and hybridize without requiring an external cavity. The thesis includes experimental demonstrations of two geometries: 2D planar semiconductors sustaining exciton-polaritons and spherical water droplets sustaining vibrational polaritons. The existence of cavity-free polaritons reveals that polaritons are more common than previously thought, as even water droplets in mist are polaritonic. The findings presented here open the possibility of studying polaritonic properties in more straightforward and prevalent structures.

Keywords: Strong and ultrastrong coupling, decay rates, cavity-free polaritons, self-hybridized polaritons, Lorentz resonances, Mie modes, Fabry-Pérot microcavities, self-assembled microcavities, Casimir force, plasmons, 2D–crystals, water droplets.

List of publications

The following papers are included in this thesis:

I **Polaritonic linewidth asymmetry in the strong and ultrastrong coupling regime**
Adriana Canales, Therese Karmstrand , Denis G. Baranov,
Tomasz J. Antosiewicz & Timur O. Shegai
Nanophotonics **12, 21**, 4073-4086 (2023)

II **Tunable self-assembled Casimir microcavities and polaritons**
Battulga Munkhbat, Adriana Canales, Betül Küçüköz,
Denis G. Baranov & Timur O. Shegai
Nature **597**, 214–219 (2021).

III **Abundance of cavity-free polaritonic states in resonant materials and nanostructures**
Adriana Canales, Denis G. Baranov, Tomasz J. Antosiewicz
& Timur O. Shegai
The Journal of Chemical Physics **154**, 024701 (2021).

IV **Perfect absorption and strong coupling in supported MoS_2 multilayers**
Adriana Canales, Oleg V. Kotov & Timur O. Shegai
ACS Nano **17**,4, 3401-3411 (2023).

V **Fano combs in the directional Mie scattering of a water droplet**
Javier T. Marmolejo, Adriana Canales, Dag Hanstorp
& Ricardo Méndez-Fragoso
Physical Review Letters **130**, 043804 (2023).

VI **Self-hybridized vibrational–Mie polaritons in water droplets**
Adriana Canales, Oleg V. Kotov, Betül Küçüköz
& Timur O. Shegai
In revision. *ArXiv preprint arXiv:2309.06906* (2023).

Declaration of author contributions:

I: I fabricated the samples, did the calculations, performed all experiments, data analysis, led the discussions and was the main responsible for writing the manuscript.

II: I built the setup and led the Fourier microscopy characterization, assisted in optical experiments, co-wrote, and provided feedback on the manuscript.

III: I performed the calculations, led the discussions, and was main responsible for writing the manuscript.

IV: I fabricated the samples, did the calculations, performed all the optical characterization and data analysis, led the discussions, and was the main responsible for writing the manuscript.

V: I assisted with calculations, participated in the discussions, and provided feedback on the final manuscript.

VI: I performed all experiments and data analysis, did the calculations, lead the discussions, was the main responsible for writing the manuscript.

Supplementary papers not included in this thesis:

S.I Collective strong light-matter coupling in hierarchical microcavity-plasmon-exciton systems

Ankit Bisht, Jorge Cuadra, Martin Wersäll, Adriana Canales,
Tomasz J. Antosiewicz & Timur O. Shegai
Nano Letters **19(1)**, 189 – 196 (2019).

My contribution: I assisted in optical measurements, did part of the nanofabrication, and took part in discussions.

S.II Ultrastrong coupling between nanoparticle plasmons and cavity photons at ambient conditions

Denis G. Baranov, Battulga Munkhbat, Elena Zhukova, Ankit Bisht,
Adriana Canales, Benjamin Rousseaux, Göran Johansson,
Tomasz J. Antosiewicz & Timur O. Shegai
Nature Communications **11**, 2715 (2020).

My contribution: I assisted with the first samples for the project, the final theoretical analysis, and provided feedback on the manuscript.

S.III Rotational self-alignment of templated Casimir microcavities

Betül Küçüköz*, Oleg V. Kotov*, Adriana Canales*, Alexander Yu.
Polyakov, Abhay V. Agrawal, Tomasz J. Antosiewicz
& Timur O. Shegai
In Manuscript.

My contribution: I performed nanofabrication, built the fiber-bundle based set-up, assisted in measurements, took-part in discussions and provided feedback on the manuscript.

Acknowledgements

In life, our interactions with others hold a significant impact on shaping our journey. As such, this thesis is a product of my interactions with numerous people over the past five years, and I am immensely grateful for that. While it is challenging to name everyone, I will list as many people as possible. Please note that this list may be lengthy.

First, I would like to thank my supervisor, Timur Shegai, for giving me the time and resources to develop my skills. Despite initial challenges, we overcame obstacles together. You are a brilliant scientist with an infectious passion and a clear vision, but also a humane leader who always sees the best in your team members. I am very grateful for the freedom and trust you gave me to explore different projects and, most importantly, for the incredible opportunity to work and learn with your group over the years.

Mikael Käll, my examiner. Thank you for always giving me your honest opinion and advice. Also, for being a living example that science does not have to be our single passion to succeed in it.

Tomasz Antosiewicz, my co-supervisor. Thank you for all the FDTD simulations and calculations. Your dedication, experience, and intuitive understanding have been invaluable. I appreciate your patience and the extensive discussions that have enriched my understanding.

Denis G. Baranov, you have always been my co-co-supervisor in my eyes. Thank you for your kindness and support during moments of confusion. I learned much more than just theory from you. You are a true role model.

Betül Küçüköz, my dear office mate and friend. I feel incredibly lucky to have shared these five years with you. I doubt I could ever fully express my gratitude. Thank you for all the support, learning opportunities, laughter, mistakes, successes, gossip, tears, and, most importantly, for being who you are.

Javier Tello Marmolejo, I am very grateful for your trust in involving me in your project. Thanks to you, I started taking myself seriously as a scientist. Our scientific and life discussions have been invaluable to me, and I have grown a lot simply by chatting with you. You are the future academia needs, but I am confident you will succeed in whichever path you choose.

Oleg Kotov, it is always a pleasure to hear you discuss the basics of physics. Your ability to delve into details and communicate them effortlessly has clarified many questions for me. I am incredibly grateful for the calculations that inspired my best measurements.

Therese Karmstrand, I am so grateful for having you around as a fellow strong coupling PhD. Thank you for all the fun discussions. We could always revisit the basics without any fear of judgment. I greatly admire your determination to pursue your goals. I am confident that you will have a successful academic career and, most importantly, thoroughly enjoy it.

Ricardo Méndez Fragoso, alias the Random Professor Rich. I am grateful for our serious and fun discussions on life and science. Thank you for clarifying that sometimes, my confusion results from ambiguous literature and not from a lack of talent. I hope you come more often to visit us.

Daniel Andrén, thank you for sharing your PhD wisdom and teaching me EBL when I started. Also, thank you for trusting me with your swimming training and being such a fantastic human being. You will always be an Ironman.

Ankit Bisht, thank you for your patience in teaching me fabrication basics and optical measurements. The foundation of this thesis owes much to your expertise. I am grateful for your help even after you left academia and your friendship all these years later.

Battulga Munkhbat, thank you for the help with AFM and all the hard work in the Casimir project. It was great work. I am very happy to see you are a rising star in Denmark.

Martin Wersäll and Michael Strührenberg, thank you for the insight and advice as PhDs before me. Luis Martins, thank you for your assistance, even when you were unfamiliar with my setup. Thank you all for creating a strongly coupled group I was eager to join.

I am grateful for my amazing corridor mates, including the ex-BNP and NBP members. Especially to Emelie, Pantea, Steve, Mahdi, Gosha, Mindaugas, Sasha, Carlos, Abhay, Vasilii, Ruggero, Tom, Hana, Michaela, Adrian, Katya, and Ximin. Thank you for all the crazy random conversations we had during lunch and Fika. Every weird topic we discussed was delightful, and I wish I could always laugh as much.

A special thanks to the physics girls Ariadna, Hanna, Emelie, Pantea, Kajsa, Rebeka, Julia, and Martina. Together, we have formed a strong and supportive alliance on our journey for gender equality. I am happy that you will persist in advocating for positive change.

Thanks to Mathias, Ariadna, Andrea, Daniel, Björn, Yu-Wei, Sara, Agin, Junjie, Christopher (both), Yin, Michael, Yao, Martina, and everyone else involved in the doctoral student representative boards (DS, FFF, and CPPC). You were such incredible teammates in every project. I sincerely believe our efforts are essential, and we have made an impact. Keep up the good work!

I am grateful to Richard, Moyra, Deborah, Eva Olsson, and Timur for all the help and support during my sick leave and recovery. I would also like to thank my physiotherapists and swimming coach, Patty Kohlmann. Water pushed me forward when I literally could not stand on my own. I came back stronger than ever.

I must also mention my incredible friends Karen, Laura, Javier, Daniela, Simon, Emiliano, Martín, Diana, Erick, and Linn, who were like a second family to me and provided me with support and happiness on this journey. Thank you for always being there and never too tired to party.

Finally, I am deeply grateful to my family for all the support through all these years. I would not be where I am today without my parents, Paz and Adrián. Los amo, muchachones. I am also grateful to my amazing fiancé and COVID-officemate, Sean. You made this journey truly special. Sitting at that "Career Planning" table was a stroke of luck, as I could not have wished for a better life companion. I am excited for our bright future together. Jeg elsker deg, mi Chonis.

Adriana Canales Ramos

Göteborg, 2023

Contents

Abstract **iii**

List of publications **v**

Acknowledgements **ix**

1 Introduction **1**

2 Light-matter interactions **7**
2.1 Optical properties of matter 7
2.1.1 Drude-Lorentz model 8
2.1.2 Permittivities of real materials 10
2.2 Perfect absorption in thin MoS_2 layers 14
2.3 Optical resonators 17
2.3.1 Fabry-Pérot resonators 18
2.3.2 Plasmonic nanoresonators 20
2.3.3 Mie resonances in spheres 23
2.4 Fano resonances in a single water droplet 25
2.5 Self-assembled microcavities by Casimir forces 27

3 Conventional polaritons **31**
3.1 A short historical perspective on polaritons 31
3.2 Weak, strong and ultrastrong coupling 33
3.3 Plasmon – microcavity polaritons 40
3.3.1 Polaritonic eigenfrequencies in the complex frequency plane 42
3.3.2 Decay rates in plasmon – microcavity polaritons 43
3.4 Bulk polaritons 44
3.4.1 Asymmetric decay rates in bulk polaritons 46
3.5 Self-assembled Casimir polaritons 46

4 Cavity-free polaritons **49**
4.1 Polaritons in 2D slabs 49

4.1.1 Polaritons and perfect absorption in MoS_2 slabs 50
4.1.2 Polaritons in hBN slabs 52
4.2 Polaritons in 1D infinite cylinders 56
4.3 Polaritons in 0D geometries 56
4.3.1 Polaritons in hBN nanodisks 57
4.3.2 Polaritons in water droplets 59
4.4 Limits and applications for cavity-free polaritons 61
4.4.1 Critical size 61
4.4.2 Maximum Rabi splitting 62
4.4.3 Implications of cavity-free polaritons 63

5 Research methods 67
5.1 Analytical calculations 67
5.1.1 Quasinormal modes in open systems 67
5.1.2 Scattering matrix 68
5.2 Nanofabrication 72
5.2.1 Microcavities and plasmonic particles 72
5.2.2 Transfer and characterization of 2D materials 73
5.3 Optical characterization 74
5.3.1 Fourier microscopy and spectroscopy 74
5.3.2 Active modulation of self-assembled cavities 77
5.3.3 Fourier-Transform Infrared Spectroscopy 78
5.4 Optical levitation of water droplets 78

6 Concluding remarks 81
6.1 Summary of the appended papers 82
6.2 Outlook 87

Chapter 1

Introduction

You are probably reading this text on a screen. The screen emits light that enters your eyes and focuses on photoreceptors that convert it into electrical signals that your brain processes as words. This simple example highlights how the interaction between light and matter facilitates our ability to perceive and understand the world.

Most of these interactions are weak, where the energy is transferred only in one direction. For instance, when you look at a screen, your eye does not send photons back to the screen. Energy is transferred only from the photon to the receptors in your eye and not the other way around.

However, let us consider an example where energy transfer occurs both ways. Think of an atom that emits a photon. In the weak coupling regime, the atom cannot recover its energy once the photon is released into free space. But if the atom is placed between two perfectly reflective mirrors, they can ensure the photon stays around long enough until the atom reabsorbs it. This allows the energy back into the atom, enabling it to re-emit a photon and repeat the cycle. This process creates a reversible energy exchange, leading to a *strong* coupling interaction. At this point, light and matter hybridize, creating a quasi-particle called *polariton*.

If the mirrors are not perfect, the imperfections cause the photons to leak, thus losing energy in the optical cavity created by the mirrors. The energy loss rate is called the *decay rate*. Similarly, the atom has its own decay rate, given by, for example, energy loss to heat. In this case, strong coupling is reached if the energy exchange between light and matter is faster than the decay rate of both components.

Polaritons possess fascinating characteristics that distinguish them from their components. Their properties include new energy levels, new decay rates, and coherence. Studies reveal that polaritons can modify photophysics [1, 2], chemical reaction rates [3–5], charge transport [6], energy transfer [7], and more [8, 9]. Additionally, polaritons can facilitate coherence for quantum processing and polariton condensation [10–12]. If the coupling disappears, the material will regain its original properties.

Because polaritons are light-matter hybrids, their ingredients are a photonic mode and a resonance in a material. In the example of the atom in a cavity, the material resonance is given by the transition between electronic energy levels in the atom. However, the resonance can also result from an excitonic or a vibrational transition. **Chapter 2** explains the optical properties of the materials that sustain these resonances and how this thesis models them. In the same example, two mirrors formed a cavity that supported the photonic mode. Although two mirrors may be the simplest form of an optical resonator, they can take many different forms and variations. The same chapter describes the optical resonators in this thesis, including the well-known Fabry-Pérot resonators, plasmonic nanoresonators, and Mie resonances in spheres.

Once the ingredients are understood, **Chapter 3** introduces the discussion on strong light-matter interactions. The chapter begins with a historical overview of polaritons to understand their development over the years from two perspectives. The first perspective focuses on the quantum electrodynamics (QED) description of a single photon single atom interaction, which led to the terms "weak" and "strong" coupling. The work of Haroche follows this view [13], who won a Nobel prize in 2012 for the quantum control over single photon and single atom interactions [14]. The second perspective concentrates on the properties of solids when their interactions with light cannot be neglected. In this context, the term "polariton" was coined by Hopfield in 1958 [15] to refer to what is now known as bulk polariton [16].

In 1992, Weisbuch *et al.* [17] merged both perspectives by demonstrating microcavity exciton-polaritons in quantum wells. This discovery marked the beginning of the microcavity polariton era [18], which has since evolved into various platforms that utilize different materials and cavities. Among the materials used are quantum wells [18, 19], organic molecules [20], quantum dots [21, 22], perovskites [23], and 2D materials [24]. The cavity types include dielectric [18] and metallic [25] Fabry-Pérot microcavities, photonic crystals [21], surface plasmons [9, 26], single plasmonic

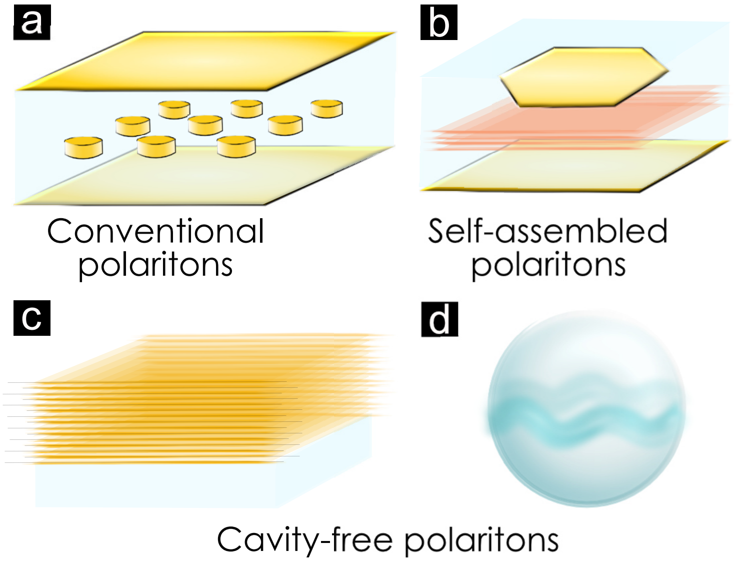

FIGURE 1.1: (a) Plasmons in metallic nanodisks coupled to photons in a metallic microcavity, therefore these are an example of conventional polaritons. (b) Excitons in WSe_2 strongly coupled to photonic modes in a self-assembled metallic microcavity comprised of a floating gold flake floating on top of a gold mirror. (c) Cavity-free polaritons in MoS_2 flakes by hybridizing its excitons to the photonic modes sustained by the geometry (planar dielectric cavity). (d) Vibrational modes self-hybridized to Mie modes sustained by spherical droplets.

particles [27, 28], and plasmonic arrays [29]. This thesis refers to all these as *conventional* polaritons, where a resonant material is coupled to an external cavity.

The first part of this thesis studies the decay rates of these conventional polaritons. Among all the possible platforms described above, **Chapter 3** describes one where plasmons (collective oscillations of electron density) in nanodisks are coupled to microcavity photons to study conventional polaritons, as shown in Figure 1.1a. Plasmonic nanoresonators are common in the strong coupling field but are usually the "light" part of a hybrid [9]. However, plasmons are collective excitations involving electromagnetic waves (photons) and charge carriers (electrons or holes) oscillations in a material. Therefore, they are already hybrids, so they can also serve as the "matter" part [30], as demonstrated in this thesis.

Using plasmonic nanoresonators gives us control over the coupling strength of the plasmon–microcavity hybrid [31]. In general, the coupling strength depends on the material transition's dipole moment, the electromagnetic field's confinement in the cavity (mode volume), and the number of molecules/emitters involved in the collective coupling [32]. Using plasmonic nanoresonators allows us to tailor both the dipole moment and the number of nanoparticles involved in the coupling, which enables control over the coupling strength. Thus, it is possible to reach the ultrastrong coupling regime [33], where the coupling strength is a fraction of the transition energy [19]. Even deep strong coupling has been accomplished with metallic nanoparticles [34], where the coupling strength is equivalent to the transition energy [35].

Because of their metallic nature, plasmonic resonators possess significant decay rates due to Ohmic losses given by the scattering of electrons in the impurities and to absorption of light by their interband transitions. Therefore, they are an interesting platform to study the behavior of polaritonic decay rates, a problem of interest since the 1990s [36, 37]. **Paper I** studies the behavior of plasmon–microcavity polaritonic decay rates under different interaction regimes [38]. The decay rates can be visualized in measurements by its resonances' broadening. However, in **Paper I**, we opted for calculating the quasinormal modes of the system in the complex frequency plane to obtain simultaneous information on the energies and decay rates of the polaritons, as described in **Chapter 5**. Surprisingly, the asymmetry is found to be a more general effect that occurs in bulk polaritons and is independent of the material's microscopic structure.

In conventional polaritonic works, optical cavities are typically tailored to the material they interact with, as in **Paper I**. The most common cavity design consists of two mirrors, but placing the material between them makes it difficult to reach it for further modifications. Open cavities, such as plasmonic particles, have been explored to overcome this limitation. However, adjusting them after fabrication can be challenging, even with open cavities.

To address this problem, **Paper II** proposes self-assembled cavities in solution [39]. In this approach, gold flakes float in a solution and form Fabry-Pérot cavities due to a balance between electrostatic and Casimir forces, as illustrated in Figure 1.1b. The salt in the solution can passively control the self-assembled microcavity, while laser radiation pressure can dynamically control it.

On the other hand, **Paper III** questions the need for an external cavity altogether [40]. Instead, it proposes hybridizing the macroscopic material's resonance to the photonic modes sustained by its geometry. These polaritons are called cavity-free or self-hybridized polaritons. Bulk polaritons inspired them, but instead of coupling to a plane wave in the material, they rely on confined photonic modes by the material itself. Moreover, **Paper III** shows that only if a material sustains bulk polaritons can it hybridize with external cavities and self-sustained modes.

Chapter 4 discusses materials that sustain cavity-free polaritons and focuses on my efforts to measure them. For instance, **Paper IV** aimed to experimentally probe polaritons in the planar geometry [41], as depicted in Figure 1.1c. Interestingly, MoS_2 slabs are not only polaritonic, but the same unpatterned flakes also perfectly absorb light below the light-line.

Similar to perfect absorption, this thesis includes other exciting results beyond the strong light-matter interaction regime. **Chapter 2** provides an overview of the basics required to understand these results, such as perfect light absorption, optical resonators, and Casimir forces. The chapter describes perfect absorption in a few nanometers thick MoS_2 unpatterned flakes, the formation of self-assembled microcavities via Casimir attraction, and water droplets as an optical resonator. This chapter highlights that spheres have a complicated Mie spectrum because multiple Mie resonances overlap. Yet, **Paper V** presents a resonance spectrum organized in combs obtained by measuring the scattering of the droplet from a side [42]. The resonances have a Fano profile explained through a quantum mechanical analogy.

Despite the complex Mie spectrum of a single droplet, **Paper III** pointed out that single Mie modes in water droplets can reach strong coupling with the O–H stretch vibrational mode, as shown in Figure 1.1d. However, the experimental setup in **Paper V** would require significant upgrades (including an infrared laser and detector) to visualize polaritons. Instead, inspired by atmospheric sciences, mist's infrared (IR) spectrum was measured using a commercial Fourier transform infrared (FTIR) spectrometer described in **Chapter 5**. As a result, **Paper VI** demonstrates that water droplets in fog and mist are polaritonic [43].

As an overview, **Chapter 2** describes the optical properties of materials and the optical resonators used in this thesis. Then, **Chapter 3** describes the various regimes of light-matter interactions and conventional polaritons. This chapter includes a study of polaritonic decay rates and a way to simplify fabrication with self-assembled microcavities. The fabrication is further simplified in **Chapter 4** by removing external cavities. Thus, the chapter introduces cavity-free self-hybridized polaritons. All the experimental and theoretical methods details are found in **Chapter 5**.

Finally, **Chapter 6** summarizes the main findings of the research papers included in the thesis. The final chapter discusses the impact of results in the field, their significance to my research education, and present ideas for future research.

Chapter 2

Light-matter interactions

This chapter introduces important concepts for the rest of the thesis. It begins with the Lorentz model for permittivities of materials and covers the optical resonators used here for strong light-matter interactions. Even though the heart of the thesis is about polaritons, many exciting effects do not require strong coupling.

The appended papers have contributions outside of the strong coupling realm. This chapter also explores those results. First, I discuss reaching perfect absorption in an unpatterned few nanometer-thick 2D crystal. Later, following the topic of Mie resonances in water droplets, I go through the measurement of around a hundred Fano resonances in levitated water droplets. Lastly, I focus on a method to generate Fabry-Pérot resonators through self-assembly enabled by Casimir forces.

2.1 Optical properties of matter

To understand light propagating in materials, we can start by discussing light traveling in vacuum. From a classical perspective, light is an electromagnetic wave with oscillating electric and magnetic fields. In the case of a plane wave, the electric field evolves as $\mathbf{E}(\mathbf{r}, t) = \mathbf{E}_0 e^{i(\mathbf{k}\cdot\mathbf{r}-\omega t)}$. Here, $\mathbf{r}$ is the wave direction of propagation, $\mathbf{k}$ is the wave vector, and ω is the angular frequency. In a vacuum, the relationship between the wavenumber and the angular frequency is known as its dispersion relation, which is $k = |\mathbf{k}| = \frac{\omega}{c}$. I refer to this later on as the *light-line* in vacuum. Light can be described by frequency, wave number, or energy. In this case, I chose energy most of the time, where it is related to the angular frequency as $E = \hbar\omega$[1] and I describe it in electron volts (eV).

Now, imagine that the plane wave propagates through a material instead. The field **E** displaces its electrons, this generates a field that also impacts the electrons' movement. This effect of the generated field on the electrons is called polarization density, **P**. As a result, the plane wave is described by the electric displacement[2]:

$$\mathbf{D} = \varepsilon_0 \mathbf{E} + \mathbf{P} = \varepsilon_0 \mathbf{E} + \varepsilon_0 \chi \mathbf{E} \,. \tag{2.1}$$

In this equation, ε_0 represents the vacuum's permittivity while χ represents the material's susceptibility. We can simplify the equation by expressing the displacement in terms of the material's relative permittivity, denoted as $\mathbf{D} = \varepsilon_0 \varepsilon \mathbf{E}$. Therefore, the response to the plane wave is determined by the complex relative permittivity of the material, which is expressed as $\varepsilon = \varepsilon' + \mathrm{i}\varepsilon''$.

If the material is nonmagnetic, the permittivity is related to its refractive index as $\tilde{n}^2 = \varepsilon$ [44]. The real part of this macroscopic quantity, n, is related to the velocity of light in the material, $v = c/n$. Therefore, the dispersion in the material changes to $\omega = ck/n$. The imaginary part, κ, represents the extinction coefficient, which describes the absorption of light by the material.

The response of the material to incoming light usually varies with the frequency of light, ω, meaning that it is *dispersive*. The dispersion is considered in the dielectric *function*, $\varepsilon(\omega)$. Moreover, the permittivity may depend on the direction of propagation in the material for anisotropic materials [45]. Only some of the 2D materials in this thesis have out-of-plane anisotropy, hexagonal boron nitride (hBN), and molybdenum disulfide (MoS_2).

2.1.1 Drude-Lorentz model

The dispersion of the permittivity is usually related to resonances in the material. I will later address the nature of the resonances for each material used in the thesis. Let us now discuss the Lorentz model to describe classically ε [44, 45]. The model considers the electrons in the material as simple harmonic oscillators around the fixed ions. If the material is isotropic with a density of electrons (ρ), light induces oscillations around the ions with a frequency ω_0. Then, a polarization density, $\mathbf{P} = -\rho e x$, is induced that evolves in time as

---

[1] In many instances here for simplicity $\hbar\omega$ is shortened to ω.

[2] This is valid in linear optics. However, when the intensity of the field E_0 increases, nonlinearities play an important role. These effects are beyond the scope of this thesis, but they are covered in detail in [44].

$$\ddot{\mathbf{P}}(t) + \gamma\dot{\mathbf{P}}(t) + \omega_0^2\mathbf{P} = f\frac{\rho e}{m_e}\mathbf{E}(t) \ , \tag{2.2}$$

where, m_e is the electron mass, e its charge, γ is the damping frequency, and f is the oscillator strength of the resonance, which is related to the efficiency of the interaction between the electric field and the electronic or vibrational transition. Equation (2.2) is solved by performing a Fourier transform, obtaining

$$\mathbf{P}(\omega) = f\frac{\rho e^2/m_e\varepsilon_0}{\omega_0^2 - \omega^2 - \mathrm{i}\gamma\omega}\varepsilon_0\mathbf{E}(\omega) \ . \tag{2.3}$$

Assuming a homogeneous and isotropic material, we have $\mathbf{P}(\omega) = \varepsilon_0\chi\mathbf{E} = \varepsilon_0(\varepsilon - 1)\mathbf{E}$. Then, the permittivity can be written as,

$$\varepsilon(\omega) = 1 + f\frac{\omega_P^2}{\omega_0^2 - \omega^2 - \mathrm{i}\gamma\omega} \ , \tag{2.4}$$

where $\omega_P = \sqrt{\rho e^2/m_e\varepsilon_0}$ is the plasma frequency.

Equation (2.4) considers a single resonance locally. In reality, several resonances contribute to the total optical response in a material. It is possible to add more oscillators to account for resonances in the same energy range as in equation (2.5). If resonances occur at higher energies, the background permittivity can account for them [44]:

$$\varepsilon(\omega) = \varepsilon_\infty + \sum_j f_j\frac{\omega_P^2}{\omega_{0_j}^2 - \omega^2 - \mathrm{i}\gamma_j\omega} \ . \tag{2.5}$$

Until now, this permittivity has been described from a classical view. However, it is also possible to interpret it quantum mechanically. In that case, $\hbar\omega_0 = \hbar\omega_{g\to e}$ represents the energy between the ground and excited states of a transition, while $f = f_{g\to e}$ is the probability of the transition occurring [46]. It is then possible to prove that $\sum_j f_j = 1$ [44]. The following sections provide examples of the permittivity in equation (2.5) approximating the real permittivity of the materials in this thesis.

2.1.2 Permittivities of real materials

The nature of the resonances described by $\varepsilon(\omega)$ depends on the material and spectral range. These resonances can come from electronic transitions, vibrational transitions, or even excitons [44, 45]. Let us discuss the nature of the resonances of some materials considered in this thesis.

Organic molecules: J-aggregates

J-aggregates are a type of dye molecule that can self-assemble head-to-tail. This process results in a significant change in their optical properties [47]. J-aggregates can sustain delocalized excitons[3], which give rise to a sharp absorption spectrum. One of the most extensively studied cyanine dyes that form j-aggregates is TDBC[4] because of its simple spectrum [47].

The Lorentz permittivity of TDBC J-aggregates fitted to the experimental data [48] is shown in Figure 2.1. The fitting used equation (2.5) with one resonance with $\omega_0 = 2.11$ eV, $\gamma = 0.1$ eV and $\varepsilon_\infty = 2.15$. Plotting the same permittivity in the complex frequency plane shows the pole of equation (2.5), $\varepsilon(\tilde{\omega}) \to \infty$, when $\tilde{\omega} = \omega_0 - \mathrm{i}\gamma/2$. It is worth noting that γ increases the broadening of the Lorentzian in $\mathrm{Im}\varepsilon$, while $f\omega_P^2$ determines the peak height.

J-aggregates have been broadly used in strongly coupled systems [25, 49]. In particular, TDBC has been used to strongly couple to plasmonic resonances because its high oscillator strength generates a Rabi splitting larger than the high metallic decay rates [26, 28, 50]. Interestingly, since J-aggregates are formed in solution, the concentration of monomers before aggregation regulates the final absorption intensity. The concentration allows it to tune its oscillator strength. In **Paper III**, this property was used to theoretically visualize the eigenmodes of a J-aggregate in weak, strong, and ultrastrong coupling.

Water

Water's optical properties are well-documented in textbooks [46]. In this thesis, I am interested mainly in water's light absorption in the infrared (IR) spectral region [51, 52]. The absorption in this spectral region is given by its vibrational modes. The two main vibrational modes of water, H–O–H

---

[3] Excitons are quasiparticles that are formed due to the Coulombic interaction between an electron excited to the conduction band and the hole left in the valence band.

[4] TDBC stands for 5,5′,6,6′-tetrachloro - 1,1′- diethyl- 3,3′- di(4-sulfobutyl)benzimidazolocarbocyanine.

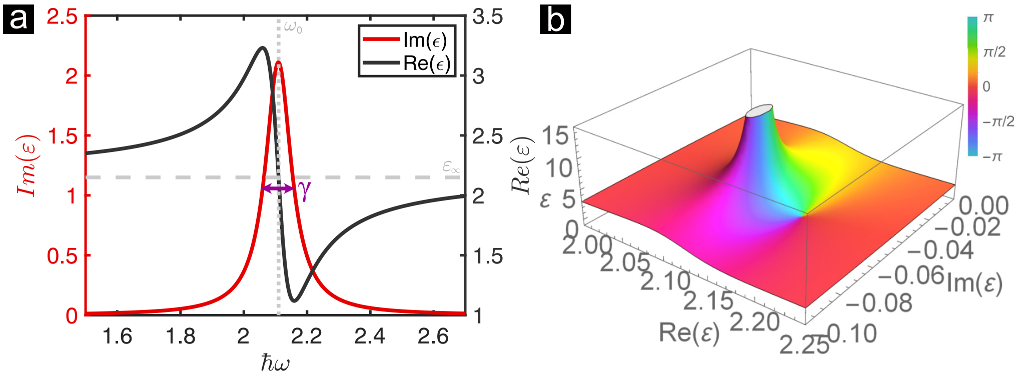

FIGURE 2.1: Permittivity of a Lorentzian fit of TDBC J-aggregates. (a) The real and imaginary parts of $\epsilon(\omega)$. The imaginary part reaches a maximum at the resonance frequency. The broadening of the imaginary part (purple arrow) is given by the system's damping, γ. (b) The same Lorentzian permittivity plotted in the complex-ω plane shows the pole at $\omega_0 - \mathrm{i}\gamma/2$.

bending and O–H stretching, are shown from left to right in Figure 2.2a. In the imaginary part of the permittivity, the bending mode appears as a peak around 0.2 eV. On the other hand, water has a symmetric and an anti-symmetric stretch so close to each other with such high oscillator strength that they merge into one peak around 0.418 eV, as shown in Figure 2.2a.

Figure 2.2 shows the Lorentzian fit of the experimental permittivity [51] using the fitting values proposed by Fiedler *et al.* [53]. The fit considers one damped oscillator for each vibrational mode in equation (2.5). **Paper VI** contains further details on the fitting values. For a more comprehensive fit to the water permittivity, an additional Debye term, described in **Paper II**, should be included [53]. This term is related to the polarization caused by the rotation of permanent dipoles at low frequencies [46]. Although not relevant for polaritons calculations, it is important for Casimir's potential calculations, as explained in section 2.5.

Atomically thin MoS$_2$

Bulk molybdenum disulfide, MoS$_2$, is an indirect band-gap semiconductor that belongs to the *Transition Metal Dichalcogenides*[5] (TMDs) family. TMDs are van der Waals (vdWs) layered materials. This means mechanical exfoliation can easily separate its layers due to the weak vdWs interaction between them. As a result, it is possible to obtain 2D-atomically thin layers similar to graphene [55–57]. As shown in Figure 2.2b, a single layer of

---

[5] TMDs are semiconductors of the type MX_2, where M is a transition metal atom (e.g., Mo, W or Ta) and X is a chalcogen atom (e.g., S, Se or Te) [55].

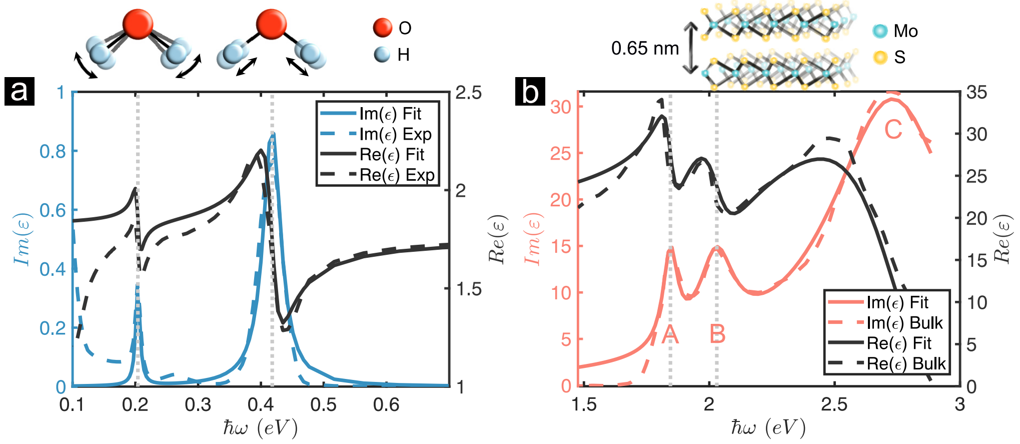

FIGURE 2.2: (a) Lorentzian fit to the experimental permittivity of water [51, 52] with resonances given by the vibrational bending (left) and stretching (right) modes. (b) Lorentzian fit of the experimental MoS_2 permittivity [54].

MoS_2 consists of three atoms, where Mo is sandwiched between two S atoms. These layers can stack to form slabs or a bulk material[6]. The dashed lines in Figure 2.2b show the experimental permittivity of bulk MoS_2 [54]. The Lorentzian is fitted using three oscillators, one for each exciton (A, B, and C)[7].

A commonly overlooked optical property of bulk TMDs is their high background refractive index in the visible range [60]. The real part of the permittivity in Figure 2.2b shows these high values. **Paper IV** uses this property to obtain optical resonances in the slabs, as described in subsection 4.1.1.

In contrast, the most popular property of TMD monolayers is the appearance of photoluminescence due to exciton recombination [61]. This occurs because the band structure changes, so the indirect band gap becomes direct. This feature makes it easy to identify monolayers, as done in **Paper IV**.

2D-atomically thin hBN

Hexagonal boron nitride (hBN) is a material composed of layers that are one atom thick and held together by vdWs forces [63]. It is commonly used

---

[6] The stacking is important for determining the thickness and properties such as second-harmonic generation and transport. In this case, for a 2H phase, the only stable stacking is AB. However, this is beyond the scope of this thesis. For a better description, see [55, 58, 59].

[7] Excitons are often present in semiconductors but are typically screened by other charges. However, in layered materials, the screening is reduced, resulting in particularly high binding energies of excitons in TMDs, which remain stable even at room temperature.

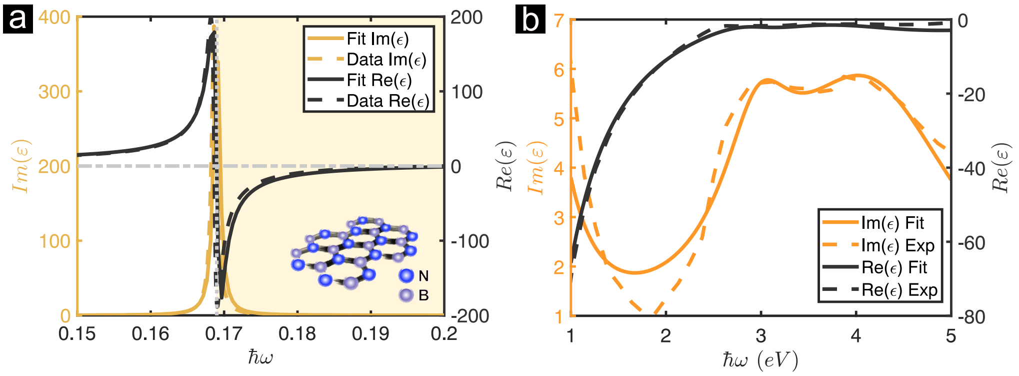

FIGURE 2.3: Materials with negative permittivities. (a) Lorentzian fit to the experimental bulk *in-plane* permittivity of hBN [54]. The shaded area represents the Reststrahlen band, where $\mathrm{Re}(\varepsilon)$ is negative. (b) Drude-Lorentz fit to the experimental gold permittivity [62].

as a substrate and insulator for other atomic crystals, enhancing and protecting their properties. However, its unique optical properties in the infrared (IR) have recently become an area of interest in their own right. Due to the large anisotropy, two phononic branches arise from the in-plane and out-of-plane lattice vibrations [63]. The in-plane branch is around 169 meV, while the out-of-plane branch is around 95 meV [64]. Figure 2.3 shows the in-plane experimental permittivity and its Lorentzian fit. Additional information about the fit is in **Paper III**.

Like MoS_2, hBN also has a high refractive index but in the IR range. **Paper III** uses this property to show that hBN slabs sustain cavity-free polaritons in the IR. In contrast, the real part of the permittivity turns negative for hBN, creating what is known as the Reststrahlen band (shaded area in Figure 2.3a). The appearance of Reststrahlen bands is common in polar crystals with strong phonon vibrations [46]. This is a reflective portion of the spectra where surface phonon-polaritons (SPhP) are supported. Moreover, these polaritons do not require any external cavities, and in subsection 4.1.2, I will discuss the distinctions between SPhPs and cavity-free polaritons.

Gold

Metals have a permittivity with a negative real part, as illustrated in Figure 2.3b. Unlike dielectrics, this negative permittivity is not caused by intense phonon vibration. Instead, it is due to free electrons in metals that can move around to reflect the incoming field. As a result, the resonance frequency in the Lorentzian (as shown in equation 2.4) is set to zero, i.e.,

$\omega_0 = 0$. This model is known as the Drude model [46],

$$\varepsilon(\omega) = \varepsilon_\infty - \frac{\omega_P^2}{\omega^2 + \mathrm{i}\gamma\omega} \, . \tag{2.6}$$

The electron collision frequency, γ, determines the damping in metals. However, this equation is limited because it only considers the free electrons in metals, not the bound electrons. For instance, noble metals such as gold contain additional bound electrons that can impact light absorption at higher frequencies [65]. The increase in light absorption from the onset of the interband transitions of gold is exemplified in Figure 2.3b. This increased absorption is what gives gold its characteristic color. To consider these bound electrons we use a Drude-Lorentz model,

$$\varepsilon(\omega) = \varepsilon_\infty - \frac{\omega_P^2}{\omega^2 + \mathrm{i}\gamma\omega} + \sum_j f_j \frac{\omega_P^2}{\omega_{0_j}^2 - \omega^2 - \mathrm{i}\gamma_j\omega} \, . \tag{2.7}$$

The parameters used to fit the permittivity values of gold are in **Paper I**. There, the gold permittivity Lorentzian fit was used to calculate the eigenfrequencies of a Fabry-Pérot microcavity, as addressed in subsection 2.3.1.

2.2 Perfect absorption in thin MoS_2 layers

The imaginary part of a material's permittivity indicates the frequencies and extent to which it absorbs light. As we have seen, some materials naturally have a large $\mathrm{Im}(\varepsilon)$ around the resonances, meaning they have enhanced absorption. Researchers have been actively designing and structuring materials to increase the amount of absorbed light, sometimes even resulting in total absorption of incoming radiation. This phenomenon is known as perfect absorption and has significant applications in fields like photodetection, sensing, and photovoltaics. Therefore, various techniques and materials have been used to achieve perfect absorption in different frequency ranges [66].

2D crystals have great potential in this field due to their ability to form ultra-thin slabs while having high absorption despite being only a few atoms thick [54]. Perfect absorption has been achieved in graphene [67] and hBN [68] from the microwave to IR regime. In the visible range, TMDs have been targeted to achieve perfect absorption in visible frequencies. Several

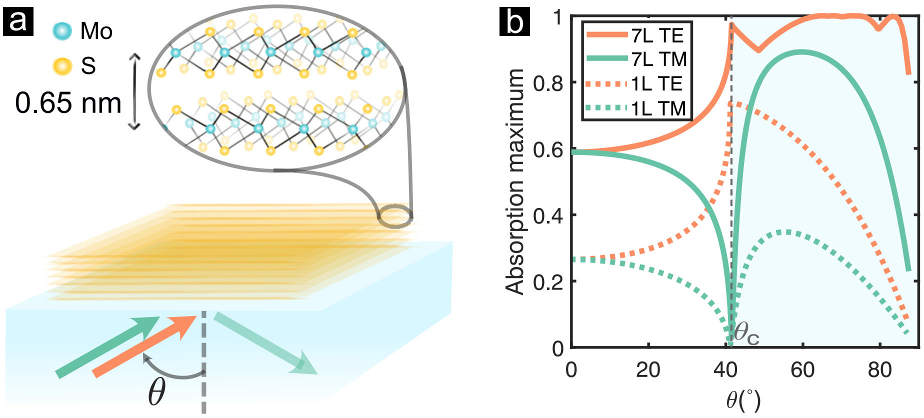

FIGURE 2.4: Perfect absorption in MoS_2 ultra-thin slabs. (a) Light shines from the bottom of the substrate with a few layers thick MoS_2 slab, which consists of a few stacked 3-atom layers. The number of stacked layers gives the thickness of the slab. (b) Maximum absorption in the visible at every angle for TE (orange) and TM (green) polarized light. Two thicknesses are considered, a monolayer (dotted lines) and a 7-layer (7L) slab shown in solid lines.

structures have been designed to maximize TMDs absorption [69–71]. However, achieving this requires careful design and fabrication.

In contrast, Häggalund *et al.* [72] noticed absorption enhancement in a dispersionless unpatterned dielectric when the refractive index of the material from which the light comes is higher than the outgoing one. The absorption is maximized for light coming at angles above the critical angle (below the light line). **Paper IV** extends this idea to a dispersive MoS_2 slab (also called *flake*), as shown in Figure 2.4a. Here, light comes from glass ($n = 1.51$), passes through MoS_2, and is scattered into air ($n = 1$).

This process is polarization-dependent. Figure 2.4b shows that the maximum absorption in the visible range reaches 100% for a 7-layer (7L$\sim$ 4.6 nm) MoS_2 slab for TE-polarized light, but it only reaches $\sim 85\%$ for TM polarization. Interestingly, a monolayer being only three atoms thick ($\sim$ 0.65 nm) reaches $\sim 70\%$ absorption by simply illuminating at the critical angle. **Paper IV** presents the experiments that show that the maximum absorption occurs around the C-exciton.

One of **Paper IV**'s most significant findings is the unique reflection spectra for each slab with thickness between 1-10L. The reflection[8] spectrum in the visible was measured at various angles as described in subsection 5.3.1, and it was calculated via the transfer matrix method (TMM). Here,

---

[8] Note that beyond the critical angle, there is no transmitted light due to total internal reflection in glass. Therefore, it is possible to calculate the absorption directly from reflection measurements by $A = 1 - R$.

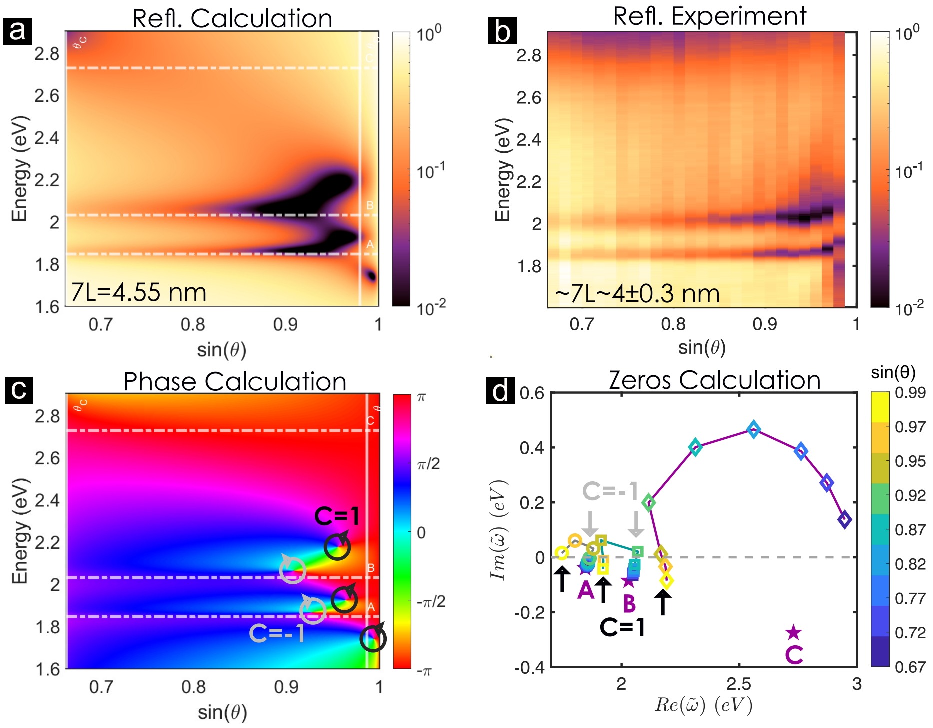

FIGURE 2.5: Perfect absorption of TE polarized light in a 7-layer MoS_2 slab. (a) Calculated reflectivity beyond the light-line by TMM. The horizontal dashed lines marked the energies of the excitons. The vertical line marks the limit of the experimental angular resolution. (b) Measured reflectivity via Fourier spectroscopy, note that the experimental angular resolution is limited. (c) Phase of the reflected wave calculated by TMM. The singularities appear in the points of perfect absorption. gray and black circles mark the topological charge of the singularities (1 and -1, respectively). (d) Zeros of the $\hat{S}$-matrix in the complex frequency plane at different angles. The frequencies at which the zeros cross the real axis are marked with gray and black arrows depending on the topological charge of its associated singularity. Figure modified from [41].

Figure 2.5a(b) shows only the example of the reflection calculation (experiment) for 7L of MoS_2 under TE-polarized light illumination. However, flakes with different thicknesses have a distinct angular reflection spectrum that could enable a direct optical, non-invasive characterization technique for the thickness of 2D crystals. This method does not require a monolayer nearby to calibrate with and is particularly interesting for flakes thicker than 4L. After this thickness, other methods like Raman spectroscopy become unreliable.

Note that the experimental resolution in reflection is 1%, meaning we cannot claim 100% absorption. To demonstrate perfect absorption, we examine the phase of the reflected wave. The phase of the reflected wave is not defined when its magnitude is zero, giving rise to a phase singularity as illustrated in Figure 2.5c. The points with singularities perfectly absorb light. For example, in the measured visible range, the 7L slab has five points of perfect absorption at different angles and energies. **Paper IV** also provides analytical formulas to find the angles and energies at which any material with permittivity $\varepsilon(\omega)$ will show perfect absorption. The formulas indicate that only 4L-8L MoS_2 flakes can absorb light perfectly and agree with the five perfect absorption points of 7L.

If a 7L MoS_2 has five singularities, what is the maximum number of singularities that can arise? We can find the answer using the $\hat{S}$-matrix (explained in subsection 5.1.2). The poles of $\hat{S}$-matrix determine the eigenfrequencies of the system. Similarly, perfect absorption occurs when the zeros of $\hat{S}$ become purely real[9] [74]. In a lossless system, all poles are in the lower plane, and the zeros are in the upper plane [73]. In MoS_2, the zeros get pulled to the lower plane because of the high loss of the excitons (see subsection 5.1.2 for more details). Therefore, the zeros can only cross the real axis (dashed lines) at most twice per exciton, resulting in a maximum of two singularities per exciton. The appearance of two singularities of opposite topological charges per resonance has been observed before in a metasurface [75].

2.3 Optical resonators

Optical resonators confine light [76, 77]. Intuitively, one can think of a resonant cavity as a set of boundary conditions reflecting light back and forth, enhancing electromagnetic fields in certain positions. The boundary conditions can vary. They can be given by a perfect mirror or simply by a sudden refractive index change. This section discusses the kinds of resonators used in this thesis, such as plasmonic nanoresonators, metallic and dielectric Fabry-Pérot cavities, and dielectric spheres.

Before diving into each resonator's details, let us start with some general definitions. An optical resonance is the response of an electromagnetic normal mode to incoming light. A normal mode is a stationary solution of the source-less Maxwell's equations in a closed system. A closed system has perfect boundary conditions, so no radiation leaks to the environment.

---

[9] They correspond to perfect absorption only below the LL, as in this case, because transmission is zero. In general, a zero in the real axis corresponds to Coherent Perfect Absorption (CPA) [73, 74].

If there are no losses to the environment, the system is Hermitian, and its eigenfrequencies are real.

However, all the systems in this thesis leak radiation into the environment. Thus, they are *open* systems. The solutions of the source-free Maxwell's equations in an open system are instead called *quasinormal modes* (QNMs) [78, 79]. The QNMs eigenfrequencies[10] are complex, $\tilde{\omega} = \omega - \mathrm{i}\gamma/2$, where γ is the decay rate of the mode. Intuitively, with a smaller decay rate, the photons stay longer in the resonator. The resonance quality is described by the *quality factor*, $Q = \omega/\gamma$ [78, 80]. The Q-factor tells the number of oscillations the resonant state has before it is damped by a factor of 2.7 [74].

The QNMs manifest in reflection, transmission, or extinction measurements or calculations depending on the system's geometry. They appear as peaks (dips) in extinction cross-sections (reflectivity) measurements. This chapter will discuss the manifestation of the QNMs and also the behavior of their eigenfrequencies in the complex frequency plane for different optical resonators.

2.3.1 Fabry-Pérot resonators

The most popular and intuitive resonator is the Fabry-Pérot resonator [81]. A Fabry-Pérot (FP) resonator is given by two reflecting surfaces, which bounce light and generate interference that leads to resonances. Usually, the reflecting surfaces are either metallic or Bragg mirrors. The higher the reflectivity of the mirrors, the higher the quality factor of the resonance.

Metallic Fabry-Pérot resonator

The FP resonant wavelength at normal incidence depends on the thickness of the cavity, denoted by L, and the refractive index of the material between the mirrors, $n = \sqrt{\varepsilon}$. If the mirrors were perfect conductors, the resonant wavelength would be $\lambda_m = 2Ln/m$, where m denotes higher order modes, such as $m = 1, 2, 3, \ldots$ [80].

Realistic metallic mirrors reflect most of the light but also transmit or absorb part of it. The more reflective the mirrors are, the better the quality factor of the resonance is [82, 83]. The mirrors used in this thesis are made of gold as sketched in Figure 2.6a. The thickness of the mirrors determines the amount of light they can reflect, which is directly proportional to the quality factor of the resonance. As previously discussed in subsection 2.1.2, gold reflects IR and visible light very well, thanks to its negative permittivity. However, the interband transitions (IBTs) of gold for energies above 2.2 eV result in absorption by the mirrors, as seen in the reflection calculation of a gold FP cavity shown Figure 2.6b.

---

[10] There is a detailed discussion about calculating the eigenfrequencies in subsection 5.1.1. Here, I focus only on the results and their physical interpretation.

The reflection was calculated using the transfer matrix method (TMM) [82, 84]. For that, the cavity was modeled for the calculation as a layered system with gold mirrors separated by a glass medium of thickness L, as shown in Figure 2.6a. The reflection from the cavity exhibits a dip in reflection at the cavity's resonance in Figure 2.6b. The minimum perfectly coincides with the eigenfrequencies of the system plotted on top for all angles of incidence, θ. The $\hat{S}$-matrix was used to calculate these eigenfrequencies, with reflection and transmission coefficients obtained from TMM, as described in subsection 5.1.2.

The resonance blue shifts at higher angles of incidence as shown in Figure 2.6b. In the complex frequency plane in Figure 2.6c, the blue shift is visualized as a shift to the right at higher angles, but the eigenfrequencies also move down. The increase in the imaginary part physically corresponds to a larger decay rate ($|\mathrm{Im}(\tilde{\omega})| = \gamma/2$). The cavity quality factor worsens at higher energies because the mirror absorption increases due to the IBTs in gold. **Paper I** focuses on the decay rates of strongly coupled structures using these metallic FP microcavities. There, the impact of the IBTs is studied by analytically removing the oscillators corresponding to the IBTs, leaving only the Drude part of the permittivity as in equation (2.6).

Dielectric Fabry-Pérot resonator

FP resonators do not require mirrors. The interfaces of a dielectric slab can reflect enough light to form FP cavities. The amount of reflection depends on the degree of impedance mismatch, which increases when the difference between the refractive indices of the incoming and outgoing media is greater. However, the reflection from an interface cannot be compared to that of a mirror, resulting in a lower FP quality factor.

The diagram in Figure 2.7a illustrates a 200 nm thick slab suspended in vacuum with $\varepsilon = \varepsilon_\infty = 2.15$ eV, typical for TDBC J-aggregates. The low-quality factor of the FP resonances results in a broad minimum in

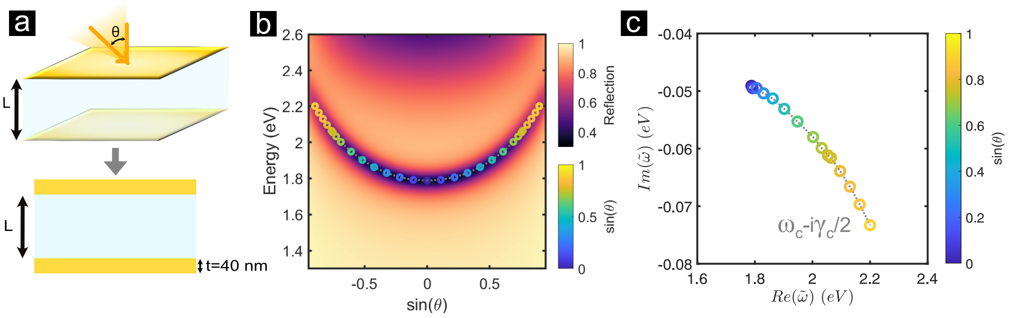

FIGURE 2.6: (a) Schematic of a metallic Fabry-Pérot (FP) resonator and its layered representation for TMM calculations. The energy of the resonance is mainly determined by the distance between the mirrors, L. The quality factor is mainly determined by the thickness of the mirrors, t. (b) Reflection of TE polarized light from a gold FP microcavity with $L = 180$ nm and $t = 40$ nm. The real part of the eigenfrequencies are plotted on top. (c) Eigenfrequencies of the same FP microcavity plotted in the complex frequency plane.

reflection as shown in Figure 2.7b. The eigenfrequencies marked on top show the two first FP modes (circles) above the LL (dashed line) and two waveguide modes below the LL (squares).

The complex frequency plane helps to visualize the radiative nature of the eigenfrequencies above the LL (circular markers). Note that the imaginary part of this FP cavity is one order of magnitude larger than the FP modes in the metallic cavity in Figure 2.6. This difference in decay rates matters for strongly coupling optical resonances and matter, as is discussed in the following Chapters.

Nevertheless, the waveguide modes (squares in Figure 2.7c) have an imaginary part approaching zero ($\mathrm{Im}(\tilde{\omega}) \to 0$). This shows the waveguide modes' lossless nature. The importance of the waveguide modes for polaritons is discussed in section 4.4.

2.3.2 Plasmonic nanoresonators

Intuitively, the previously described FP resonators need to be large enough to "fit" the photons they hold. Therefore, the distance between the "mirrors" must be larger than half a wavelength (in the medium) of the desired resonance frequency. This sets a minimum size for the resonators. However, plasmonics enabled smaller resonators, even of a few nanometers [65].

Plasmons are the quanta of free electrons' collective oscillations coupled to light. A bulk metal sustains volume plasmons, which are *longitudinal*

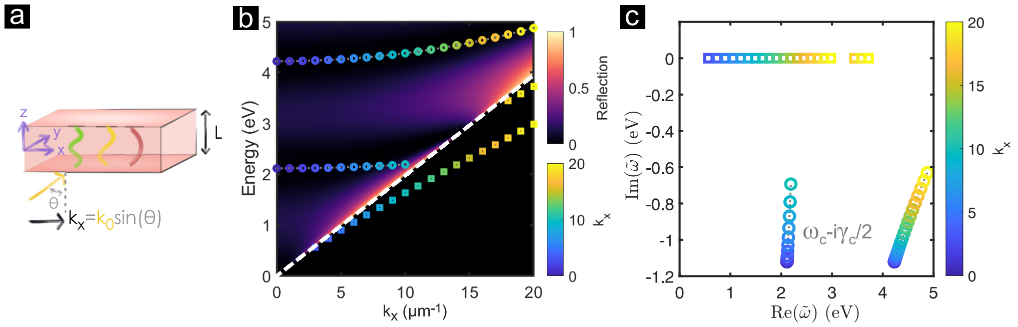

FIGURE 2.7: (a) Schematic of a dielectric slab of thickness $L = 200$ nm and $\varepsilon = 2.15$. (b) Reflection of light from the slab for various k-vectors, $k_x = k_0 \sin\theta$. The markers show the eigenfrequencies. A white dashed line marks the light line (LL). Above it, the modes are radiative (circular markers), and below it they are guided (square markers). The colorbars mark the reflection and the wave vector. (c) Eigenfrequencies plotted in the complex frequency plane. The colorbar marks the corresponding wave vector.

collective electron oscillations when $\varepsilon(k,\omega) = 0$, and they are excited when $\omega = \omega_P$ [65]. Due to the longitudinal nature of volume plasmons, they cannot be excited with transverse electromagnetic waves. Although not trivially, surface plasmons can be excited by light [85]. Surface plasmon polaritons (SPPs)[11] are electromagnetic excitations that propagate at a metal/dielectric interface.

However, SPPs cannot be excited with direct light in free space. In contrast, localized surface plasmon resonances (LSPRs) are bounded in three dimensions and can be excited with direct illumination. The LSPR occurs when free electrons in a metallic nanostructure oscillate in response to an external electromagnetic field. The LSPR frequency depends on the metal's permittivity, the surrounding medium's permittivity, and the shape and size of the structure [65].

Paper I uses the LSPR tunability in gold nanodisk arrays by changes in their diameter. The reflection spectra in Figure 2.8a show that smaller nanodisks blue shift the resonance and decrease its intensity. Prof. Tomasz Antosiewicz numerically simulated the reflection spectra using the Finite-difference time-domain method (FDTD) in the software Ansys Lumerical [87].

One can also vary the array's pitch, Λ (distance center to center). **Paper I** keeps the pitch large enough to avoid altering the spectra due to near-field interactions between the nanodisks [65] and smaller than the incident wavelength to avoid surface lattice resonances [88]. In this pitch range, the reflection closely follows a Lorentzian response. Due to the oscillatory

---

[11] As the name explains, these are polaritons [86], and I will return to them in chapter 4 to discuss their relation to surface phonon polaritons.

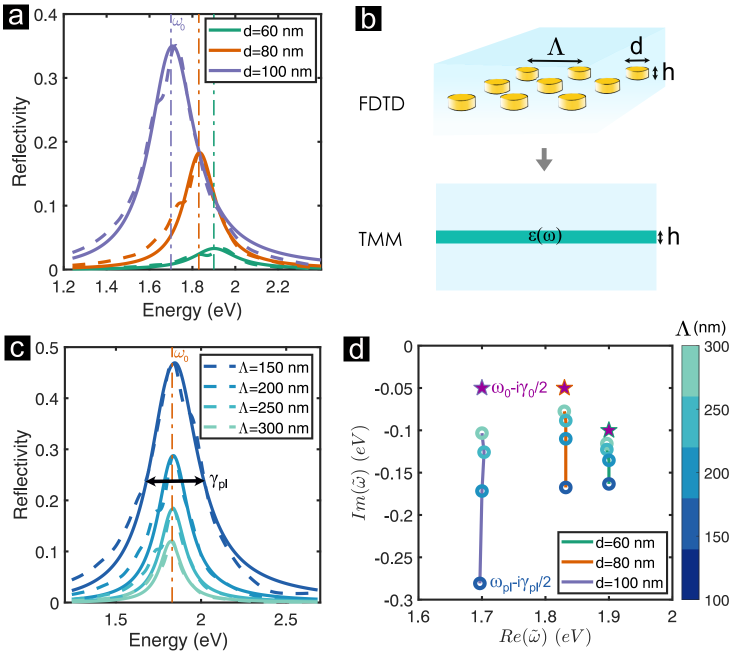

FIGURE 2.8: (a) Reflectivity of gold nanodisks simulated by FDTD (dashed lines) for 3 diameters, $d = 60, 80$ and 100 nm with the pitch fixed to $\Lambda = 300$ nm. The nanodisk's reflectivity is fitted with the reflectivity from a dispersive thin-film as shown in (b). (b) Schematic of the gold nanodisks being approximated as a dispersive thin-film with the same height as the nanodisks. The arrays are characterized by their pitch, Λ and the diameter of the disk, d. (c) Numerical simulation (dashed lines) and Lorenzian fit (solid line) of the reflectivity of gold nanodisks with $d = 80$ nm and varying the pitch. (d) Eigenfrequencies (in circles) in the complex frequency plane of the approximated dispersive Lorentzian slab embedded in glass. The pole of the permittivity for each diameter is marked in a purple star. The colorbar shows different pitches. Figure modified from [38].

nature of the electrons that cause the resonance, it is reasonable to consider the nanodisks response as a Lorentzian material [89]. Therefore, in **Paper I**, the nanodisk arrays are approximated as a dispersive layer of the same height as the nanodisks to use TMM to calculate its eigenfrequencies, as shown in Figure 2.8b.

To determine the effective Lorentz permittivity of the nanodisks, we first calculate the reflection of a single slab in glass using TMM. The permittivity of the slab is given by equation (2.5). We then compare this calculated reflection with the reflection of the nanodisks in glass, simulated by FDTD. The effective Lorentz permittivity is determined when the two reflections match[12]. Figure 2.8a,c compare the simulated (dashed) and the calculated (solid) reflections. The effective permittivity reproduces the optical response of the nanodisks very well in both cases.

---

[12] All the fitted values of the effective permittivity can be found in **Paper I**.

The LSPR tunability is visualized in the complex frequency plane when obtaining the eigenfrequencies of the equivalent slab in glass. A change in pitch affects the amplitude and FWHM of the resonance, as shown in Figure 2.8c. In the complex frequency plane, the decrease in pitch results in a growth of the imaginary part of the eigenfrequencies, which in turn pushes the circles in Figure 2.8d downwards. Thus, decreasing the pitch increases the coupling of the arrays to free space, increasing radiative losses.

The star marks the pole of the effective permittivity $\varepsilon(\omega)$, which represents the eigenfrequencies of the slabs without interactions with any electromagnetic modes. Physically, it would represent a "bare" plasmon fully shielded from the environment. These decay rates are non-radiative. Interestingly, smaller disks gain non-radiative losses, as shown by the most right star in Figure 2.8d. This increase is due to the onset of the IBTs, which damps the LSPR. None of the eigenfrequencies (in circles), $\tilde{\omega_{pl}}$ occur at the star because the interactions with free space always induce some radiative decay rate.

Despite their significant decay rates due to Ohmic losses and IBTs, plasmonic nanoresonators allow for subwavelength confinement of light. Therefore, the strong coupling community has utilized them as cavities with tight confinement, allowing single-molecule studies [27]. However, plasmons are already light-matter hybrids and can also play the "matter" part role. **Paper I** assumes so and hybridizes them with metallic microcavities. The arrays' tunability is leveraged to investigate different interaction regimes, ranging from weak to ultrastrong. **Paper I** will be further discussed in chapter 3.

2.3.3 Mie resonances in spheres

Finally, let us consider the last type of resonator: a water ($\varepsilon = 1.75$) sphere of radius R in vacuum. Spheres sustain optical Mie modes, named after Gustav Mie, who found the solutions in 1908. Mie theory describes a plane wave in spherical coordinates (an infinite series of spherical vector harmonics) scattered by a sphere. The complete derivation is in ref. [46].

Mie resonances can be found as the poles of the scattering coefficients in Mie theory for TM (TE) modes, a_l (b_l). A TM (TE) mode is defined as having no radial magnetic (electric) field [46]. Physically, the multipole mode

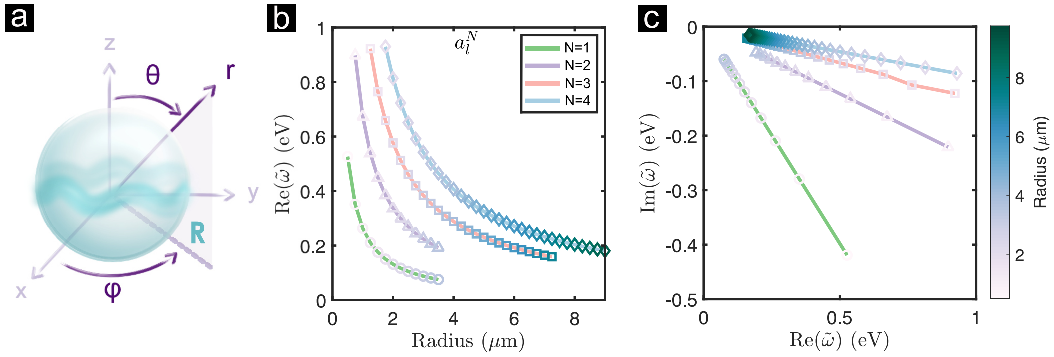

FIGURE 2.9: (a) Schematic of a dielectric sphere that sustains optical resonances. (b) Real part of the eigenfrequencies of the first four Transverse Magnetic dipolar Mie modes, a_1^N in the IR range of the spectrum. Different radii sustain different resonances. (c) Eigenfrequencies in the complex frequency plane show the frequency and the decay rate of the modes of spheres of different radii (colorbar).

number l can be visualized as the number of electromagnetic field maxima around the circumference of the droplet. For a fixed angular number l and radius R, multiple order modes occur at different energies with varying radial numbers, N. This mode order specifies the number of maxima in the radial direction inside the droplet [90].

The first four radial modes $N = 1, 2, 3, 4$ (computed from equation (5.9) as explained in subsection 5.1.2) for the electric dipole (TM$_{1,N}$ or a_1^N) are shown in Figure 2.9b. Higher-order modes are sustained for larger radii. Their decay rates decrease with the radial number N, as shown in Figure 2.9c. Larger l multipolar modes also require a larger droplet to resonate. Thus, the larger the radii, the more modes the sphere sustains.

All modes coexist in the droplet and contribute to the extinction spectrum, a commonly measured observable. The extinction cross-section depends on the droplet's radius and the wavelength of the light. To obtain the extinction cross-section, you can either fix the radius and explore different wavelengths or vice-versa using the formula [46],

$$\sigma_{ext} = \frac{2\pi}{k^2}\sum_{l=1}^{\infty}(2l+1)\mathrm{Re}(a_l + b_l) \ . \tag{2.8}$$

Regardless, the size parameter $x = kR$ is the important factor for calculations (see subsection 5.1.2 for details), where $k = 2\pi/\lambda$.

In **Paper VI**, we focus on spanning the energy, keeping the radius fixed as shown in Figure 2.10b. The covered energy range is extensive for spectroscopy and is achieved by Fourier transform IR (FTIR) spectroscopy

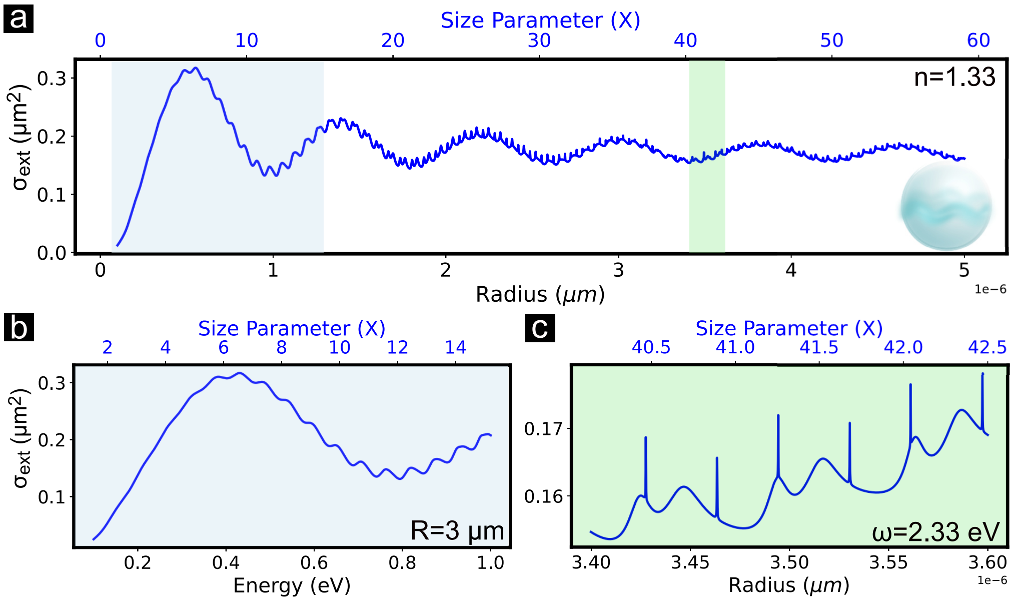

FIGURE 2.10: (a) Extinction cross-section of water spheres (n=1.33) of different sizes for fixed light energy of 2.33 eV (532 nm). (b) Extinction cross-section of the first size parameters in (a) but calculated for a fixed radius of R=3 μm in an IR spectrum between 0.1-1 eV. (c) Close up to the complexity of several resonances overlapping for diameters around 3.5 μm calculated at a fixed energy of 2.33 eV.

as described in subsection 5.3.3. Note that for this calculation, I considered only the background permittivity. Therefore, there is no strong coupling. The extinction of a coupled sphere is discussed in subsection 4.3.2.

Measuring large spectral ranges is usually a challenging task. Measuring the full range of size parameters calculated in Figure 2.10a in an experiment with a fixed diameter would require sources and detectors in energies between 0.1-4 eV. This is a daunting task. However, it is possible to measure the full range if the radius varies instead. **Paper V** shows this measurement via optical levitation, as described next.

2.4 Fano resonances in a single water droplet

The resonances of a levitated droplet were observed by Ashkin back in 1977 [91]. Despite being an oil droplet instead of water, the resonances overlapped as in Figure 2.10c. Soon after, each resonance was carefully associated with a Mie mode, a_l^N, b_l^N by direct calculation using Mie theory [92]. It is still common practice to compute the resonances to figure out the overlapping and order of the resonances.

In **Paper V**, a cleaner spectrum of a_l^N resonances was obtained from the scattering of a levitated water droplet evaporating over time, as described in section 5.4. The resonances appeared equally spaced and ordered in combs as shown in Figure 2.11a.

Moreover, the observed resonances evolve from Lorentzians to asymmetric profiles, as visible in Figure 2.11b. Fano resonances are characterized by displaying such asymmetric lineshapes. They were first described by Ugo Fano [93] in the context of electron scattering. However, they also appear in photonic systems and have recently attracted a lot of attention [94]. Fano resonances occur because of the interference between a discrete state and a continuum. In photonics, they also result from the interaction of a sharp resonance and a very broad one [94].

Mie resonances have been theorized to be a cascade of Fano resonances [95], but only a few have been measured at the same time [96]. **Paper V** shows around a hundred Fano resonances arranged in three combs. To explain the entire spectrum, **Paper V** used a previously proposed quantum analogy based on the radial, time-independent Schrödinger equation [97].

The analogy results in a potential well for each radius and fixed l, as shown in the inset of Figure 2.11b.i. The energy levels in the well are Mie modes and are "excited" when they have the same energy as the laser's energy level,[13] k^2, shown in a gray dashed line. Photons reach the well from the right and have a barrier to tunnel into it. As illustrated in Figure 2.11b.i, the smallest radius has a minimal barrier for the a_{11}^2 Mie mode to be excited. Therefore, light easily tunnels in but is trapped briefly before leaving the well with a negligible phase difference. This results in a broad Lorentzian when interfering with the continuum outside of the well.

For a larger radius, the barrier (in pink) grows because the well is moving up with respect to the laser line (Figure 2.11b.ii). Then, the mode is trapped longer, and the phase difference increases, resulting in a more intense asymmetric Fano shape. The asymmetry grows with the size of the barrier until it reaches the most asymmetric Fano shape at the end of the comb (Figure 2.11b.v). At this point, the potential well has moved too up in energy, and no more $N = 1$ modes resonate.

---

[13] Note that the laser's energy level is different from the laser's energy, 2.33 eV. The latter is the color of the laser.

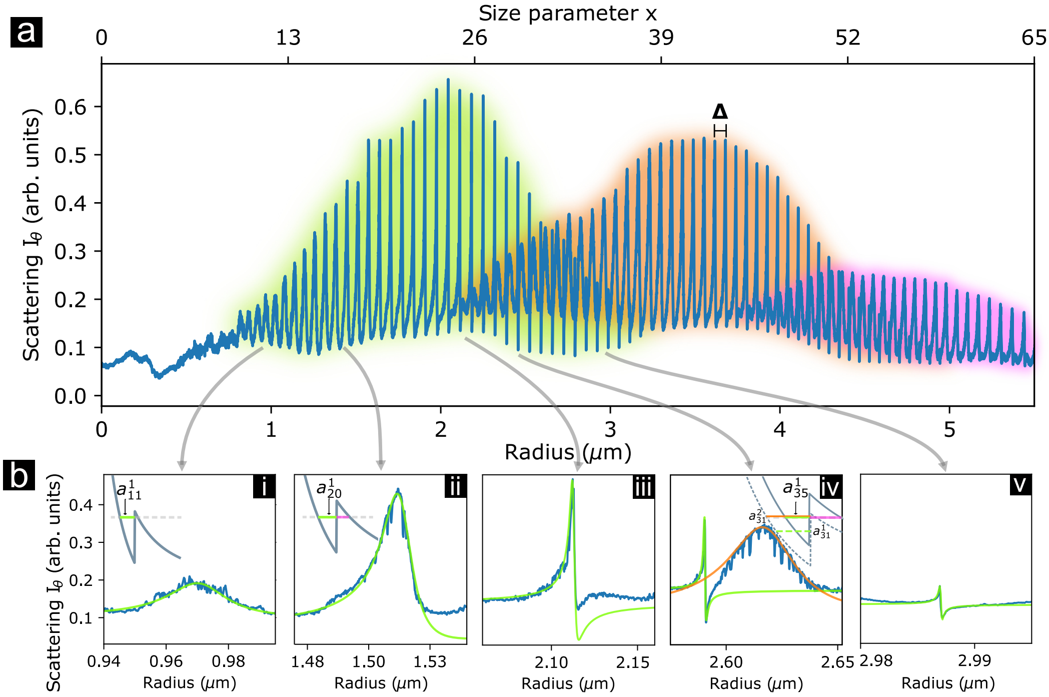

FIGURE 2.11: (a) Fano resonances for an evaporating water droplet. Each resonance corresponds to a multipolar number, l, ascending with the radius. Each comb corresponds to a radial number, N. The green comb corresponds to $N = 1$, the orange to $N = 2$, and the purple to $N = 3$. (b) Individual Fano resonances of the 1st comb evolving from a Lorentzian (i) to a completely asymmetric Fano profile (v). The inset shows the well obtained from the quantum mechanical analogy. Figure modified from [42].

However, at the end of the first comb, the droplet radius is large enough for the next radial mode, $N = 2$, to resonate with the laser (the potential is in dashed lines). However, the barrier is small again, so the resonance is close to a Lorentzian shape as marked in orange in Figure 2.11b.iv. This begins the next comb that repeats the cycle. This quantum analogy explains all three combs in the measured size parameters.

2.5 Self-assembled microcavities by Casimir forces

Usually, FP microcavities are fabricated with a given thickness (L) between them to sustain resonances on a specific energy. Instead of forcing two mirrors to a fixed position, **Paper II** presents a way of obtaining metallic self-assembled cavities using synthesized gold flakes that float in solution.

The gold flakes are synthesized as colloids by reducing gold ions with ascorbic acid in a cetyltrimethylammonium bromide (CTAB) aqueous

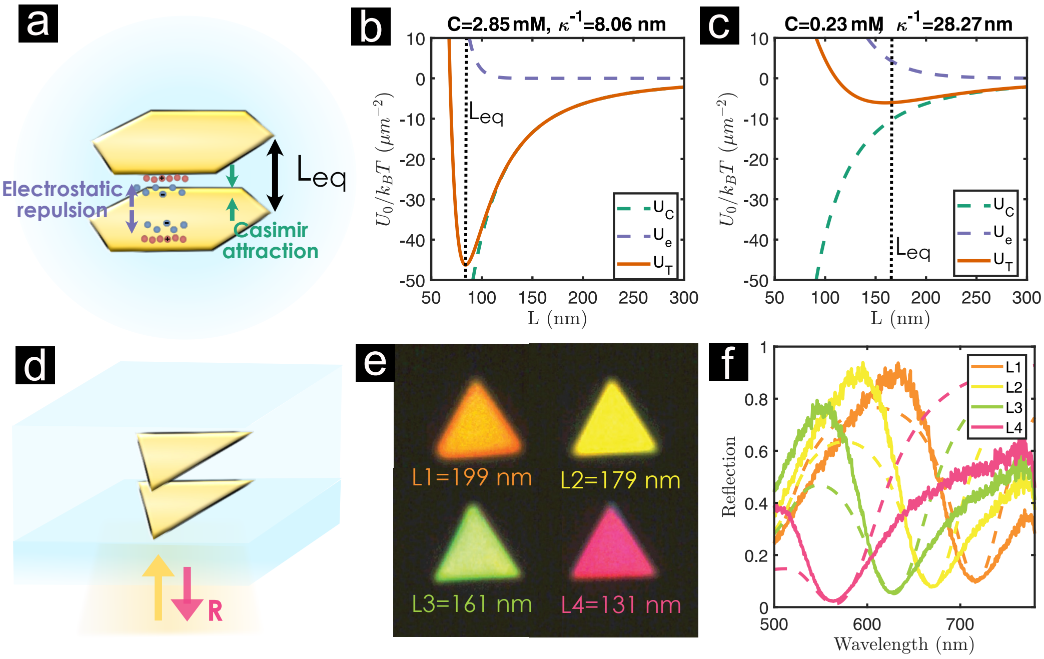

FIGURE 2.12: (a) Self-assembly of a Fabry-Pérot (FP) cavity in solution by the equilibrium of electrostatic repulsion and attractive Casimir forces. The equilibrium distance L_{eq} determines the FP resonance frequency. (b) Sum (orange) of the Casimir (green) and electrostatic (purple) potential calculation for an experimental cavity with a total ion concentration $C = 2.85$ mM (c) $C = 0.23$ mM. (d) FP formed by a floating gold flake aligned to a gold triangle patterned by EBL on the glass substrate. (e) True-color image in reflection of the self-assembled FP using a patterned substrate. (f) Normal incidence reflection spectra shows the resonance wavelength for different L_{eq}. The dashed lines represent the fit by TMM to determine L_{eq}.

solution [98]. CTAB works as a capping agent to stabilize the gold nanoflakes' growth and prevent them from aggregating. Once in solution, CTAB dissociates in cation CTA$^+$ (red circles) and anion Br$^-$ (blue circles) as shown in Figure 2.12a. Therefore, the flakes feel electrostatic repulsion between them. The screened electrostatic potential between two charged gold mirrors in an ionic solution is [99],

$$U_e = \frac{2\sigma^2}{\varepsilon_0 \varepsilon(0)\kappa} e^{-\kappa L} \; . \tag{2.9}$$

Where σ is the surface charge density, $\varepsilon(0)$ is the static permittivity of water, q_0 is the elementary charge, C is the total concentration of ions with valence z (which in case of CTAB is one) and $\kappa^{-1} = \sqrt{\frac{\varepsilon(0)\varepsilon_0 k_B T}{C q_0^2 z^2}}$ is the Debye-Huckel length. The potential is positive, meaning the repulsion increases with higher surface charges. This potential is in purple dashed curves in Figure 2.12b,c.

Adding this electrostatic potential with a van der Waals (vdWs) potential explains colloids' usual aggregation and short-range self-assembly in the DLVO (Derjaguin-Landau-Verwey-Overbeek) theory. This theory suggests that if the distance between two gold planes is less than κ^{-1}, the vdWs attraction will dominate and cause the plates to aggregate [99].

In contrast, **Paper II** shows self-assembly of gold dimers with colorful resonances as shown in the true-color reflection pictures in Figure 2.12e. The distances between the mirrors were determined by measuring the reflection spectra (shown as solid curves) and fitting them with TMM (shown as dashed curves) as demonstrated in Figure 2.12f. These distances are around or above a hundred nm, $L_{eq} \gtrsim 100$ nm, which are very long distances for vdWs forces to be relevant. This long-range stability suggests that Casimir forces play a role instead.

Casimir and Polder expanded the known vdWs interactions to consider retardation and thus be valid at long distances [100]. The same year, Casimir calculated the interaction between two infinite metallic plates and found an attractive force between both plates $F_C = \frac{\hbar c \pi^2}{240 R^4}$ [101]. Casimir considered perfect electrical conductors as plates in vacuum, but Lifshitz and his collaborators expanded the theory for it to be used with real materials in isotropic and non-magnetic media [102, 103]. Using this Casimir-Lifshitz approach, the potential between the two gold plates in water is,

$$U_C = \frac{\hbar}{2\pi} \int_0^\infty d\xi \int_0^\infty \frac{d\mathbf{k}_\parallel}{(2\pi)^2} \mathbf{k}_\parallel \ln\det\left(1 - \mathbf{R}_1 \mathbf{R}_2 e^{-2K_0 L}\right) . \tag{2.10}$$

This potential is obtained integrating over the imaginary frequency $\omega = i\xi$, where ξ is real and over all the in-plane wave vectors, $\mathbf{k}_\parallel$ in the gap region. The material properties are included on the reflection operator, $\mathbf{R}_i$ for each side of the system, $i = 1, 2$:

$$\mathbf{R}_i = \begin{pmatrix} r_i^{ss} & 0 \\ 0 & r_i^{pp} , \end{pmatrix} \tag{2.11}$$

with the Fresnel reflection coefficients r_i^q for each polarization $q = s, p$. Finally, $K_0 = \sqrt{\mathbf{k}_\parallel^2 + \xi^2/c^2}$ is the z-component of the wave vector in the gap between the two mirrors evaluated at the imaginary frequency. The integral depends on the materials of the system and was calculated by Dr. Denis G. Baranov. Once the materials are fixed (gold mirrors and water in between), the potential depends only on the distance between the mirrors as depicted in green curves in Figure 2.12b,c.

The total potential is the sum of electrostatic and Casimir potentials, $U_T = U_e + U_C$. The minimum in the total potential indicates that two mirrors in water can create a stable cavity for distances in the expected range of $L_{eq} \gtrsim 100$ nm. Higher concentrations of solution result in a smaller L_{eq} (as shown in Figure 2.12b), while lower concentrations increase L_{eq} (as shown in Figure 2.12c). Therefore, the cavity resonance frequency can be adjusted with the ion concentration of the solution. **Paper II** explores this static tuning and studies the dependence of the resonance frequency with the total ion concentration.

We explored having a bottom mirror fabricated on the sample and one floating flake to have more control over the cavities. Having one mirror fixed facilitates control over the formed cavity because we manipulate a single floating gold flake. **Paper II** had mirrors on extended surfaces, while **Paper S.III** explores patterned substrates in triangular lattices as bottom mirrors. Figure 2.12d shows the example of patterned triangles of a similar size to the floating gold flakes.

To manipulate the floating flake, **Paper II** employs laser irradiation, similar to optical tweezers. This technique also enables the vertical position of the flake to be adjusted, thus changing the distance between the two mirrors. As a result, the resonance frequency can be dynamically modulated using laser irradiation pressure. This effect is further examined in section 3.5, where a polariton is achieved using these self-assembled cavities and excitons in a 2D crystal. This dynamic control enables us to adjust the polaritonic composition of the hybrid material. However, to fully comprehend this concept, we should first understand what a polariton is, as discussed in the following chapter.

Chapter 3

Conventional polaritons

This chapter focuses on the strong coupling regime, where light and matter hybridize and require a description as a new quasiparticle: a *polariton*. In this thesis, *conventional* polariton refers to a polariton obtained with an external cavity. However, in this chapter, I also discuss *bulk* polaritons that do not need an external cavity. These were the first polaritons, so to start the chapter, I give a brief historical perspective on why an external cavity was included.

Then, I dive into the definitions of weak, strong, and ultrastrong coupling regimes. Once we have the basics, I discuss the results of **Paper I**, which uses an unconventional way to visualize polaritons in the complex frequency plane to obtain simultaneous information about polaritonic eigenfrequencies and decay rates.

Finally, I discuss self-assembled polaritons as obtained in **Paper II**. They offer static and dynamic tunability of the coupling strength and polaritonic composition.

3.1 A short historical perspective on polaritons

The term *polariton* dates back to the 1960s. The term's origin is usually related to Hopfield's work on excitons in solids [15]. He noticed that it was necessary to consider exciton interactions with light propagating in the solid to describe their properties accurately. We now refer to this as *bulk polaritons*. Hopfield used the quantum mechanical framework developed by Fano to describe phonons in a solid, replacing their classical macroscopic permittivity description [104]. However, the quantum mechanical framework is not crucial to describe them. A few years before, in 1951, Huang noticed that the classical description of phonons in a solid needed to consider retardation when light had similar energies to the phonons in the crystals [105], as in our previous Casimir discussion. The result of considering retardation was a dispersion curve that we now associate with phonon polaritons (PhP). However, measuring bulk polaritons required them to propagate to a boundary and scatter there. They quickly noticed that if a material sustained bulk polaritons close to the surface, it also sustained surface polaritons that propagate along interfaces, which could be easier to measure [16]. From there, the term surface phonon polariton (SPhP) was coined. In the past, these polaritons were heavily studied experimentally in crystals, and there has recently been a new wave of interest in polaritons in 2D-atomic crystals [64]. Until here, there is no external cavity required. Polaritons are intrinsic modes to the materials.

Why is a cavity needed if polaritonic modes are ubiquitous to some materials? Cavities enhance light-matter interactions in cases with minimal interaction. They are necessary when only one molecule or atom interacts with the electric field because atoms have minuscule dipole moments. Studying the interaction of a single atom with a photon was experimentally unthinkable until the development of the maser in 1955 [106]. The maser enabled the interaction of a couple of molecules with the electric field, hence paving the way for studies on single-molecule interactions with the electric field. Subsequently, Jaynes and Cummings proposed their well-known Hamiltonian in 1963 [107]. This field has evolved into what is now known as *cavity quantum electrodynamics* (cQED) [14], which developed terms like *strong coupling* and *Rabi oscillation*. A Rabi oscillation represents a complete cycle of excitation that passes from the atom to the cavity and back to the atom. In 1983, Haroche's group measured Rabi Oscillations between a cavity and N Rydberg atoms [13]. Haroche continued his work on controlling single photons with atoms and was awarded a Nobel prize in 2012 [14]. Enhancing single-atom interactions in these experiments requires extremely high-quality cavities.[1]

In 1992, when researchers were studying the interaction between single atoms and photons, Weishbuch et al. published a groundbreaking work that merged the concepts of polaritons and strong coupling [17]. Their research involved coupling dielectric microcavity photons with excitons in Quantum Wells. This platform was more controllable, as the polaritons could be tuned with the microcavity. Bulk polaritons, on the other hand, were difficult to control and relied solely on the material. Weisbuch's research led to the development of the field of *microcavity polaritons* [18], which linked atomic physics and solid-state physics, drawing ideas from both fields.

---

[1] Recently, the interaction between a single atom and cavity photon has been advanced using *giant atoms* in superconducting qubits. These atoms have a high and adjustable dipole moment, reducing the need requirements on the cavities, which has led to the emergence of a field known as *circuit QED*. This field has pushed the coupling strength to the ultrastrong coupling (USC) regime, which will be explained in the following section. Therefore, cQED has extensively developed USC's theory.

Excitons in various materials have been coupled to dielectric microcavities for strong coupling since then. Such as in organic semiconductors [20] and 2D-atomic crystals dichalcogenides [108]. After that, various cavities were explored to obtain strong coupling in quantum dots [109]. Further, organic molecules with large dipole moments achieved strong coupling even with cavities that have poor quality factors such as metallic microcavities [25] and plasmonic resonators [26]. In fact, due to their simple fabrication, metallic microcavities are currently preferred for coupling to vibrational (phonon) excitations in molecules [8] or electronic excitations in perovskites [110]. Nowadays, a wide range of materials have been coupled to various cavities [111].

Next, I will discuss metallic microcavities coupled to plasmons in metallic nanodisks and excitons in WSe_2 to metallic microcavities. However, before diving into the specific platforms, let us review the different light-matter interaction regimes.

3.2 Weak, strong and ultrastrong coupling

There are classical, semiclassical, and quantum mechanical descriptions of light-matter interactions [9]. I will start with the popular quantum mechanical Jaynes–Cummings Hamiltonian [107] because it is pedagogical. I will not dive into derivations (which can be found in text books [112]), but only use the model to build intuition.

Consider one photon in a single-mode cavity with an electric field $E = \mathcal{E}(\hat{a}^\dagger + \hat{a})$. A photon in the cavity field interacts with a two-level emitter that can only be in the ground, $|g\rangle$, or excited state, $|e\rangle$, as depicted in Figure 3.1. Then, the system is described by the Hamiltonian:

$$\hat{H} = \frac{\hbar\omega_0}{2}\hat{\sigma}_z + \hbar\omega_c\hat{a}^\dagger\hat{a} + \hbar g(\hat{a}^\dagger\hat{\sigma} + \hat{\sigma}^\dagger\hat{a}) \ . \tag{3.1}$$

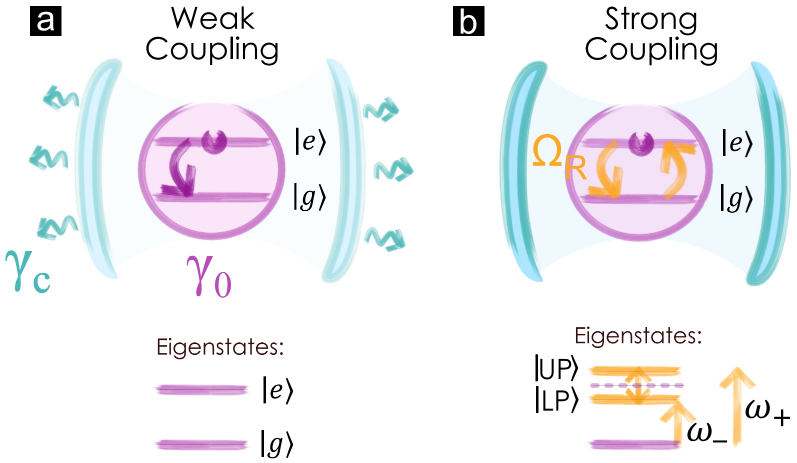

FIGURE 3.1: Weak and strong coupling in the *conventional* configuration with a generic FP cavity, in blue, and a two-level system (TLS), in purple. (a) In the weak coupling regime, the decay rates γ_c and γ_0 are larger than the rate at which the uncoupled elements share energy, Ω_R. In this case, the eigenstates of the system are approximately the same as the uncoupled ones. (b) In the strong coupling regime, the coupling strength results in a split of the eigenstates into lower and upper polaritons.

The first term corresponds to the free two-level system (TLS) and $\hbar\omega_0 = E_e - E_g$ is the transition energy between both energy levels.[2] The second term corresponds to the electric field mode resonating at $\hbar\omega_c$. The third term describes the light-matter interaction, where the annihilation of a photon excites the TLS, and vice-versa.

In the absence of a driving field, the emitter couples to the vacuum field. The coupling strength is given by $\hbar g = \vec{\mu} \cdot \vec{\mathcal{E}}_{vac}$, where $\hat{\mu} = \vec{\mu}(\hat{\sigma}^\dagger + \hat{\sigma})^2$ is the transition dipole moment. The amplitude of the vacuum field is $\mathcal{E}_{vac} = \sqrt{\hbar\omega_c/2\varepsilon\varepsilon_0 V}$, for a mode volume, V. Thus, high coupling strengths occur for large dipole moments and small cavity mode volumes.

This simple model has several extensions to include fast-rotating terms $(\hat{\sigma}^\dagger\hat{a}^\dagger, \hat{\sigma}\hat{a})$, several emitters[3], several photonic modes, diamagnetic term, etc. A good summary of which model is more accurate for each situation can be found in references [35, 113].

For this thesis, decay rates[4] are an essential missing feature in this model. In real systems, both lose energy to their environments at rates γ_0 and γ_c, as marked in Figure 3.1. To include dissipation, one can phenomenologically introduce the decay rates in the Hamiltonian by considering the cavity and TLS to have complex eigenenergies $\tilde{\omega}_{c,0} = \omega_{c,0} - \mathrm{i}\gamma_{c,0}/2$ [111]. Then, the above Hamiltonian becomes,

---

[2] $\hat{\sigma} = |e\rangle\langle g|$ and $\hat{\sigma}^\dagger = |g\rangle\langle e|$ are the atomic transition operators and $\hat{\sigma}_z = [\hat{\sigma}, \hat{\sigma}^\dagger]$.

[3] In a case with several emitters N the coupling strength increases with the number of emitters as $\sqrt{N}$ [32].

[4] The thesis treats decay rate as a synonym of linewidth because I consider $\hbar\gamma$ as γ, even though strictly speaking, these two have different units and the linewidth is the correct quantity in eV, while the decay rate should be in Hz.

$$\hat{H} = \hbar \begin{pmatrix} \omega_0 - \mathrm{i}\gamma_0/2 & g \\ g & \omega_c - \mathrm{i}\gamma_c/2 \end{pmatrix} , \tag{3.2}$$

where the new eigenfrequencies are,

$$\omega_\pm = \frac{\omega_c + \omega_0}{2} - i\frac{\gamma_c + \gamma_0}{4} \pm \sqrt{g^2 + \left(\frac{\omega_0 - \omega_c}{2} - i\frac{\gamma_0 - \gamma_c}{4}\right)^2} . \tag{3.3}$$

Here, the detuning is $\delta\omega = \omega_c - \omega_0$. The difference in decay rates is $\delta\gamma = \gamma_c - \gamma_0$ and the average uncoupled decay rate is $\gamma_{avg} \equiv \frac{\gamma_c + \gamma_0}{2}$. At zero detuning, $\omega_c = \omega_0$, the difference between the two new eigenfrequencies is the *Rabi* splitting. The Rabi frequency is the rate at which light and matter exchange energy. It is given by,

$$\Omega_R = \omega_+|_{\delta\omega=0} - \omega_-|_{\delta\omega=0} = 2\sqrt{g^2 - \left(\frac{\delta\gamma}{2}\right)^2} . \tag{3.4}$$

The Rabi splitting is real when the coupling is larger than $g = |\delta\gamma|/4$. This point is known as an exceptional point (EP) [114]. At zero detuning, both eigenfrequencies are degenerated before the EP, and higher coupling strengths result in a degeneracy lift as shown in Figure 3.2a.

Before the EP, the interaction is in the weak coupling (WC) regime, as highlighted in yellow in Figure 3.2a,b. In this regime, the interaction is not strong enough to affect the real part of the eigenfrequencies, but it alters the imaginary part, corresponding to the decay rates. At large detuning, the decay rates remain the same as for the uncoupled system. However, the decay rates become more similar at detunings closer to zero, as highlighted in yellow in Figure 3.2d. The stronger the coupling strength, the more similar the decay rates become until they eventually merge at the EP.

This modification is known as the Purcell effect[5], where a resonant (non-resonant) cavity can be used to enhance (decrease) the radiative decay rates of the emitter [115] due to an increased (decreased) density of available states

---

[5] Purcell discovered this effect in 1946 while working on measuring nuclear magnetic moments in resonant cavities in the radiofrequency (RF) range. [115]. He won the Nobel Prize in 1952 because his methods allowed him to measure magnetic moments in liquids.

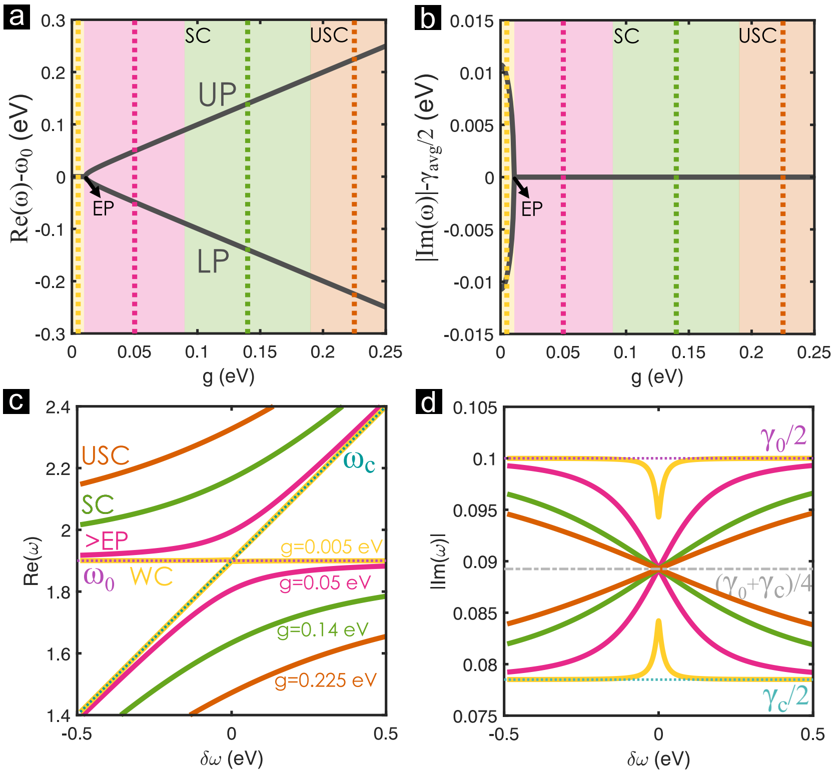

FIGURE 3.2: Eigenfrequencies of a coupled system calculated with the simplest Jaynes–Cummings (JC) non-Hermitian Hamiltonian. Here, $\omega_c = \omega_0 = 1.9$ eV $\gamma_c = 0.157$ eV, $\gamma_0 = 0.2$ eV. (a) Real part of the eigenfrequencies for various coupling strengths for $\delta\omega = 0$. The degeneracy is lifted after the exceptional point (EP). The different light matter regimes are marked in various colors: weak coupling (WC) – yellow, after EP – pink, strong coupling (SC) – green, and ultrastrong coupling (USC) – orange. (b) Imaginary part of the eigenfrequencies for the same interaction regimes. The decay rates become degenerate at $\delta\omega = 0$ after the EP. (c) Real part of the eigenfrequencies for varying detuning with a coupling strength in each interaction regime corresponding to the dashed lines in (a). (d) Imaginary part of the eigenfrequencies for varying detuning for the same coupling strengths as in (c).

for photons to decay in. The plasmonics community commonly uses this effect to enhance emission rates for sensing [65].

When the coupling strength reaches the exceptional point (EP), the real eigenfrequency degeneracy is lifted, and two new eigenmodes appear. This phenomenon is observed as an anticrossing when the detuning is varied, as shown in Figure 3.2c. However, the opposite situation occurs for the imaginary part of the eigenfrequencies ($\propto \gamma$). After the EP, they degenerate at zero detuning, and their decay rate equals the average of the uncoupled ones, $\gamma_\pm = \gamma_{avg}$. As the detuning increases, the decay rates get closer to the uncoupled values, as shown in Figure 3.2d.

The next regime after the EP in Figure 3.2 is shaded in pink and corresponds to a high enough coupling strength to present Rabi splitting

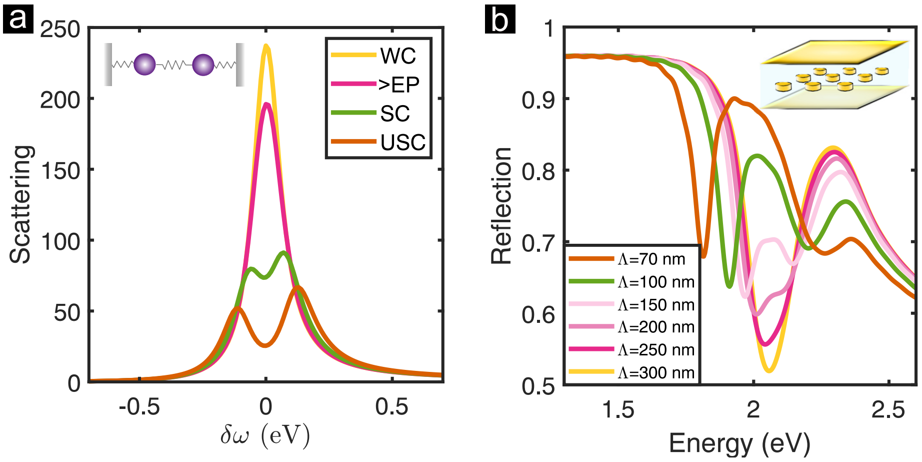

FIGURE 3.3: (a) Scattering calculated from a coupled mechanical oscillator model for parameters in weak coupling (yellow), after the exceptional point (pink), strong coupling (green) and ultrastrong coupling (orange). (b) Reflection from a coupled plasmon–microcavity system for various coupling regimes marked in the same colors as in (a). The coupling strength is controlled by the nanodisk array pitch, Λ.

but not enough to reach the strong coupling threshold. The exact coupling strength required for strong coupling is a debated topic [116, 117]. Even though some people consider the onset already after the EP [118], the more accepted threshold has been vaguely defined as the coupling required to resolve the two polaritons spectrally [9, 94]. For some, this occurs only when $g \gg \gamma_c, \gamma_0$ [94, 119]. Others consider that if the linewidth of the polaritons at zero detuning is $\gamma_\pm = \gamma_{avg}$,[6] then $\Omega_R > \gamma_{avg}$ is enough to resolve both polaritons[7] [9, 109]. Given its broad acceptance, this will be the strong coupling onset in this thesis.

To better understand the definitions, consider the following hypothetical example. In Figure 3.3a, the scattering spectra are calculated for a system with the coupling strengths considered in Figure 3.2c,d. The model used in the calculation is a coupled oscillator model from a classical mechanics perspective [83, 123]. The scattering spectrum exhibits a single peak at zero detuning in the weak coupling regime. Even after the EP, there are no two distinguishable peaks until the strong coupling regime is reached, as shown in Figure 3.3a.

---

[6] In the following sections, we will see that considering the polaritonic linewidth as average of the linewidth of the uncoupled components is just an approximation, and it can be inaccurate even at low coupling strengths.

[7] From a classical approach, this onset corresponds to Rabi oscillations taking place [120]. Rider and Barnes give a nice discussion of all the different SC onsets [117]. However, all the definitions stem from using cQED concepts in other areas, such as nanophotonics. Therefore, there are also debates about the direct applicability of those concepts [121, 122]. This discussion is beyond the scope of this thesis. However, interested readers are encouraged to refer to the given references.

In the previous hypothetical system, two polaritons are resolvable only after $\Omega_R > \gamma_{avg}$. However, two polaritons are resolvable even before in the system described in **Paper I**, where gold nanodisk arrays couple to a metallic microcavity. Their coupling strength depends on the pitch between nanodisks in the array, resulting in different interaction regimes. These regimes are shown in Figure 3.3b with the same color code as in Figure 3.3a. As expected, two distinct peaks are observed in the strong coupling regime (green). However, several pitches are above the EP (pink), and the lightest pink one has two clear peaks. Therefore, it is not always necessary to reach $\Omega_R > \gamma_{avg}$ to observe splitting in the peaks.

Hopfield Hamiltonian and coefficients

In the plasmon–microcavity platform, both plasmons and photons are bosonic fields. Therefore, the Jaynes–Cummings (JC) Hamiltonian, as shown in equation (3.1), cannot be applied. Instead, this thesis often approximates the matter component as a Lorentzian permittivity, which assumes matter as a series of harmonic oscillators. Hopfield made the same approximation in his seminal paper [15] to understand exciton behavior in crystals and proposed the following Hamiltonian,

$$\hat{H} = \hbar\omega_0\hat{b}^\dagger\hat{b} + \hbar\omega_c\hat{a}^\dagger\hat{a} + \hbar g(\hat{a}^\dagger + \hat{a})(\hat{b}^\dagger + \hat{b}) + \frac{\hbar g^2}{\omega_0}(\hat{a}^\dagger + \hat{a})^2 \,. \tag{3.5}$$

Where the first two terms represent the uncoupled oscillators. The third term is the interaction term of both fields with coupling strength $g = \mu\sqrt{\rho V}\mathcal{E}_{vac}\omega_0/\omega_c$, in the Coulomb gauge[8]. The diamagnetic term, also known as the A^2 term, is the fourth term in the equation. For small values of g, this term can be neglected. However, it becomes important when the system enters the ultrastrong coupling (USC) regime [19]. The USC regime is shaded in orange in Figure 3.4a, and it requires $\eta = g/\omega_0 \geq 0.1$, where the eigenfrequencies deviate from a linear behavior [19, 35]. The eigenfrequencies of this lossless Hamiltonian are the following,

$$\omega_\pm = \frac{\sqrt{\omega_c^2 + 4g^2\omega_c/\omega_0 + \omega_0^2 \pm \sqrt{(\omega_c^2 + 4g^2\omega_c/\omega_0 + \omega_0^2)^2 - 4\omega_c^2\omega_0^2}}}{\sqrt{2}}, \tag{3.6}$$

---

[8] The gauge choice does not change the values of the observables. Thus, one could use the dipole gauge and obtain the same eigefrequencies [33, 124].

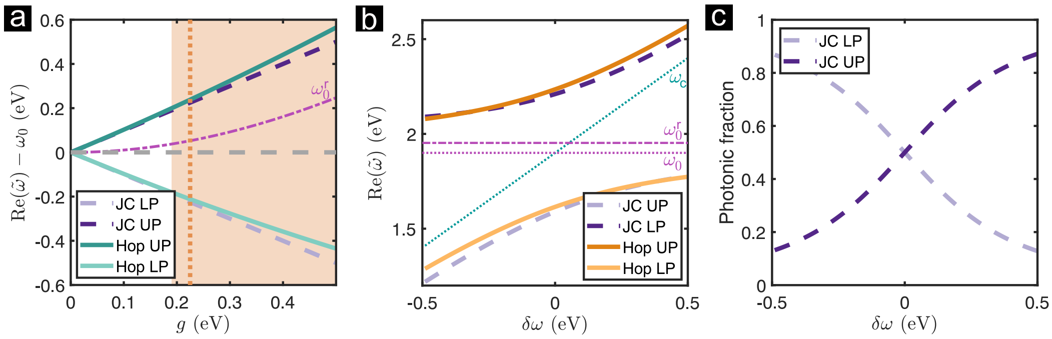

FIGURE 3.4: (a) Polaritonic eigenfrequencies for increasing coupling strength, g, with $\omega_0 = \omega_c = 1.9$ eV. Comparison between Jaynes–Cummings (JC) and Hopfield Hamiltonians. The dot-dashed line marks the renormalized frequency of the plasmon, $\omega_0^r = \sqrt{\omega_0^2 + 4g^2}$. (b) Eigenfrequencies corresponding to $g = 0.225$ eV calculated with a JC and a Hopfield Hamiltonian. (c) Photonic fraction (Hopfield coefficient) of the system in (b) for a JC Hamiltonian.

For small g in the SC regime, it is possible to obtain a Hamiltonian similar to JC in equation (3.1) by using the rotating wave approximation (RWA) and neglecting the diamagnetic term [35]. The comparison between the eigenfrequencies obtained with both Hamiltonians is shown in Figure 3.4a for increasing coupling strengths and in Figure 3.4b for various detunings with a fixed coupling strength.

In this JC approximation, the coefficients of the eigenvectors (called Hopfield coefficients) give the photonic or matter fractions. The photonic fractions depend on the detuning as shown in Figure 3.4c. In this case, perfectly mixed polaritons are achieved at zero detuning. However, in the USC, the polaritons at zero detuning are no longer evenly split between light and matter. Higher coupling strengths increase the matter (light) fraction in the LP (UP) at zero detuning [19].

Moreover, in the USC regime, the diamagnetic term renormalizes the resonance frequency of matter[9] to $\omega_0^r = \sqrt{\omega_0^2 + 4g^2}$ [125, 126]. The renormalized frequency is shown in dot-dashed magenta lines in Figure 3.4. The importance of ω_0^r will be further explored in section 3.4.

How can a system reach USC? The most common way is to increase the number of oscillators coupled, $g \propto \sqrt{N}$. However, few experimental platforms can span from weak to ultrastrong coupling regimes. Among them, there are intersubband polaritons [127], hBN in metallic microcavities

---

[9] In **Paper III**, we utilized the notation $\tilde{\omega}_0$ to represent the renormalized frequency, which is widely used in literature. However, throughout this thesis, we constantly use the complex frequency plane, where $\tilde{\omega}_0$ is equivalent to $\omega_0 - i\gamma_0/2$. In order to avoid any confusion, I use the notation ω_0^r instead.

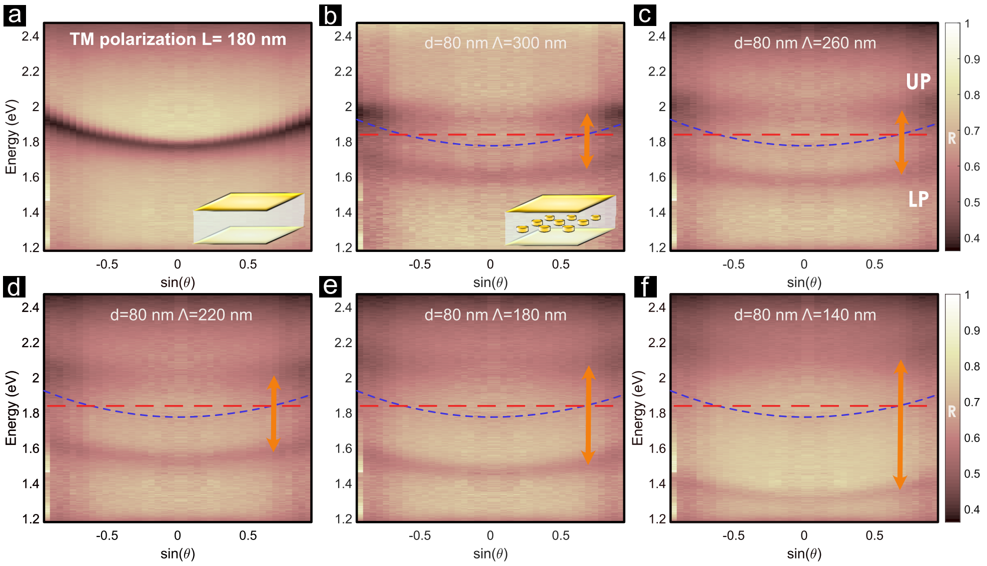

FIGURE 3.5: Dispersion in reflection of plasmon–microcavity polaritons for TM polarized light. The system has $L = 180$ nm and $d = 80$ nm. The red dashed line shows the uncoupled plasmon and the blue dashed line shows the empty cavity dispersion in (a). The arrays have different pitches that tune the coupling strength from SC to USC regime: (b) $\Lambda = 300$ nm, $\Omega_R \approx 0.28$ eV, (c) $\Lambda = 260$ nm, $\Omega_R \approx 0.36$ eV, (d) $\Lambda = 220$ nm, $\Omega_R \approx 0.44$ eV, (e) $\Lambda = 180$ nm, $\Omega_R \approx 0.56$ eV, (f) $\Lambda = 140$ nm, $\Omega_R \approx 0.76$ eV.

[128], and carbon nanotubes [129], among others. In **Paper I**, the plasmon–microcavity hybrid is used due to its versatility to span all regimes, as described next.

3.3 Plasmon – microcavity polaritons

Ameling *et al.* [30] began the study of the strong interaction between LSPR of metallic nanostructures (also called *meta–atoms*) and microcavity photons. Meta–atoms offer great versatility because one can tune their resonance frequency, dipole moment, and, to a certain extent, even their resonance width.

In this thesis, all meta–atoms are gold nanodisks arranged in lattices separated center-to-center by a pitch, Λ, as described in subsection 2.3.2. Their coupling strength to the microcavity field increases directly with d and inversely with Λ [31, 33]. This behavior is experimentally visualized in dispersion measurements in reflection shown in Figure 3.5b-f for TM polarization[10]. As expected, the Rabi splitting (Ω_R in orange arrows) between both polaritons grows for smaller pitches. The measurements are obtained in the Fourier plane as described in subsection 5.3.1.

---

[10] **Paper I** presents measurements and analysis for TE polarization for simplicity because the electric field is parallel to the dipole moment of the nanodisks for all angles. Thus, g remains constant even at all angles.

Figure 3.5f presents a significant reduction in the linewidth of the LP compared to panel b. At the same time, the UP broadens to the point where it becomes difficult to differentiate it from the absorption caused by the IBTs in gold. This observation was even more apparent in **Paper S.II** because the density of the meta-atoms increased, even reaching the USC regime with a reduced coupling strength of $\eta \approx 0.55$.[11] This polaritonic linewidth asymmetry observation sparked the analysis in **Paper I**.

Although **Paper S.II** used the Hopfield Hamiltonian framework to analyze ground-state modification of the system [33], the plasmon–microcavity platform is purely classical. Therefore, **Paper I** opted to use a classical approach to determine the eigenenergies of the system. The approach involved finding the eigenenergies via a pole-search method using the scattering matrix ($\hat{S}$-matrix), as explained in detail in subsection 5.1.2. This method automatically includes all the higher-order modes, dissipation, and all the Hamiltonian terms that must be included in a quantum model. Additionally, this technique provides both the real eigenfrequencies and decay rates simultaneously.

The only approximation of this pole-search method is that the LSPR response of the nanodisks is considered analogous to the optical response of an equivalent thin film with an effective Lorentzian permittivity. This approximation was suggested previously by Ameling *et al.* [89]. Previously, subsection 2.3.2 described the Lorentzian fit of the reflection response of the bare nanodisks outside the cavity. However, as in any approximation, it results in losing some information about the system.

In this case, our model does not consider the interactions between nanodisks mediated by the cavity. To consider these interactions, Berkhout *et al.* [130] proposed a transfer matrix to describe the plasmonic arrays. However, their method is only accurate at normal incidence, while **Paper I** also studies angular incidence. Nonetheless, **Paper I** showed that the effective Lorentzian permittivity approximation remains valid even at higher angles.

---

[11] **Paper S.II** reached this coupling without filling the full microcavity with meta-atoms, indicating that adding more nanodisk arrays could lead to reaching the regime where $\eta \approx 1$. Such regime is known as deep strong coupling, and it has been achieved by tightly packing gold nanoparticles in a crystal [34].

Using this approximation makes the study more general because many other experimental platforms in strong coupling use matter components whose permittivity is also approximated to a Lorentzian, as Zhu *et al*. did for atoms [131], Fano for phonons in crystals [104] and Hopfield for excitons in crystals [15]. As described in subsection 2.1.2, it is also a common approximation for excitons in organic molecules [48], excitons and phonons in 2D-crystals [132] and phonons in solution [8]. Therefore, the results obtained with this approximation can be generalized to many other systems.

3.3.1 Polaritonic eigenfrequencies in the complex frequency plane

Typically, strong coupling is visualized through dispersion plots, as shown in Figure 3.6a,d. However, in an open system, the eigenfrequencies are naturally complex. This thesis uses the complex frequency plane to visualize the eigenfrequencies, which is unusual in the strong coupling community. By using the complex frequency plane, it is possible to convey information about the resonance frequencies and their decay rates simultaneously. Figure 3.6b,e shows the same eigenfrequencies plotted in the complex frequency plane.

Paper I visualized the eigenfrequencies of conventional polaritons behavior in the complex frequency plane across different coupling regimes, ranging from weak to ultrastrong. The complex frequency plane in the weak coupling regime visualizes the Purcell effect (which results in a shift in the imaginary part of the eigenfrequency), and the Lamb shift (shift in the real part) [94]. As the coupling strength increases, a topological change occurs after the EP point [38]. This is the only transition in the eigenfrequencies behavior. Here, the polaritons split into two separate branches as seen in Figure 3.6b,e.

The eigenfrequencies' behavior in the complex frequency plane remains consistent regardless of the type of polaritons. These can include conventional polaritons in a cavity (**Paper I**), cavity-free polaritons coupled to their own optical modes in several geometries (**Paper III**, **Paper IV**, and **Paper VI**), and even bulk polaritons (**Paper III**). The behavior for different interaction regimes is detailed in **Paper I** and **Paper III**.

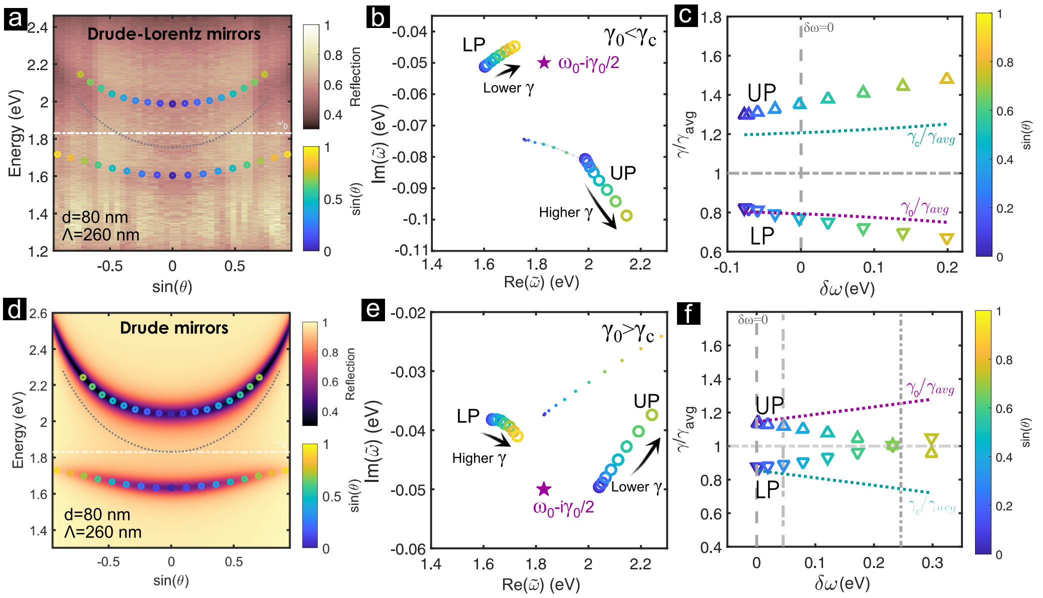

FIGURE 3.6: *Left column:* dispersion in reflection of plasmon–microcavity polaritons with the eigenfrequencies on top obtained with the pole-search method for (a) Experimental reflection with eigenfrequencies obtained for Drude-Lorentz (DL) mirrors with IBTs. (d) Calculated reflection and eigenfrequencies obtained for Drude mirrors without IBTs. *Middle column:* eigenfrequencies in the complex frequency plane for (b) DL mirrors causing a lossy cavity with $\gamma_c > \gamma_0$ and (e) Drude mirrors with a cavity with $\gamma_c < \gamma_0$. *Right column:* Decay rates of the polaritons with (c) DL mirrors and (f) Drude mirrors. The uncoupled decay rates are marked in dotted lines. The vertical dashed line marks zero detuning $\delta\omega = 0$. Image modified from [38].

The pole of the effective Lorentz permittivity is marked with a purple star and is considered the "uncoupled" plasmon in Figure 3.6b. The polaritons (circles) usually approach the uncoupled components' trajectories (star and dotted line). More than that, the UP imaginary part goes beyond the uncoupled cavity for Figure 3.6b. This increase in decay rate is due to the contribution of the interband transitions (IBTs) of gold in the mirrors to the losses, which causes a high-loss cavity mode with $\gamma_c > \gamma_0$.

Our approach allows us to "turn off" the IBTs contributions, resulting in the trajectories shown in Figure 3.6e, where $\gamma_0 > \gamma_c$. It is worth noting that even without IBTs, the LP and UP trajectories in the complex frequency plane remain asymmetric, which is intriguing. In fact, the asymmetry of the decay rates at zero detuning is the key takeaway of **Paper I**.

3.3.2 Decay rates in plasmon – microcavity polaritons

The linewidth commonly associated with polaritons at zero detuning is the average of the uncoupled losses, $\gamma_\pm = \gamma_{avg}$ [9, 22, 111, 133]. This result is obtained in the simplest JC approximation as discussed in Figure 3.2d.

However, asymmetries in the linewidth have been previously observed in experiments. Thorough studies on the asymmetry of polaritonic decay rates at zero detuning were done in the 1990s when mainly excitons in quantum wells were hybridized with dielectric cavities. Several models discussed the symmetry through different microscopic mechanisms, but all were based on the disorder in the excitons [36, 37, 134–138]. The asymmetries continue to be observed in modern experiments with other materials but are automatically attributed to the disorder as proposed in the 1990s. Except for Wang *et al.* [139], who observed the asymmetry even though the disorder in their platform was small, and they attributed it to cross-damping.

The plasmon–microcavity polariton is homogeneous under the Lorentz approximation and free of disorder. Nevertheless, the linewidth asymmetry is still noticeable, as shown in Figure 3.6c. The asymmetry is enhanced by the contribution of the IBTs in the mirrors, causing the UP to be broader for higher angles and coupling strengths because it spectrally overlaps with the IBTs. But even when removing IBTs in the mirrors, the asymmetry persists at zero detuning as shown in Figure 3.6f. However, in this case, the polaritons share the same linewidth at a higher detuning, as observed for excitons previously [37, 139]. This effect is solely due to electromagnetism, with no influence from microscopic structure.

In the field of plasmonics, a similar electromagnetic effect can occur where the interaction of two plasmons can generate resonances of asymmetric linewidths. The mode with narrow linewidth is known as subradiant, and the broad one as superradiant. In this case, the effect is due to interference [140, 141]. However, **Paper I** demonstrated that this effect persists in bulk polaritons.

3.4 Bulk polaritons

As originally studied by Hopfield [15, 142, 143], bulk polaritons are formed when a plane wave traveling through a material interacts with the material resonances (given by e.g. excitons or phonons) in it. Bulk polariton modes are found as roots of the dispersion equation in the material,

$$kc - \omega\sqrt{\varepsilon(\omega)} = 0\ , \tag{3.7}$$

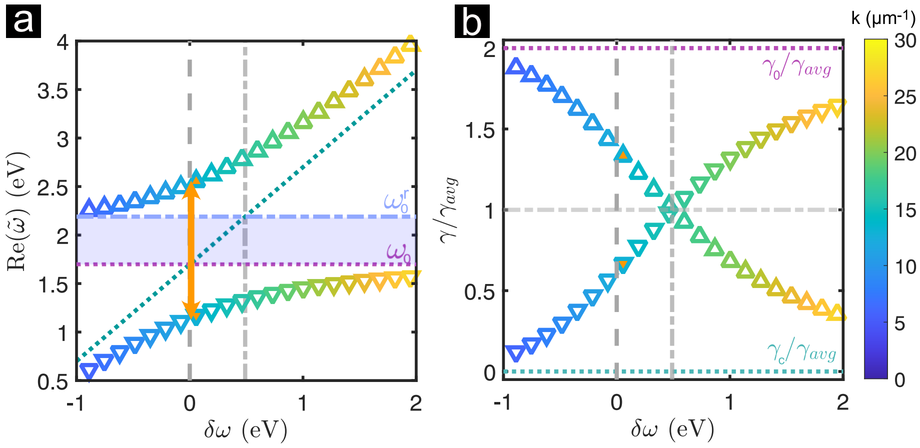

FIGURE 3.7: (a) Real eigenfrequencies of the bulk polaritons with an effective permittivity corresponding to a nanodisk array of $d = 100$ nm and $\Lambda = 260$ nm. The uncoupled eigenfrequencies are shown in dotted lines (ω_0 in magenta and ω_c in turquoise). The renormalized frequency, ω_0^r, is marked in the blue dot-dashed line. The polaritonic gap is shaded in blue. (b) Asymmetric decay rates of the bulk polaritons. Zero detuning is marked with a vertical gray dashed line. The vertical gray dot-dashed line marks the detuning for which $\omega_0^r - \omega_c = 0$. Figure modified from [38].

where $\varepsilon(\omega)$ is the permittivity of the material, which is approximated here by a simple Lorentz formula, as stated in equation (2.5). In **Paper III**, the coupling strength is expressed in terms of the oscillator strength (f) and plasma frequency (ω_P) of the Lorentz permittivity as $g = (\omega_P/2)\sqrt{f\omega_0/\varepsilon_\infty\omega_c}$[12]. Interestingly, the *bulk coupling strength* at zero detuning as $g_B = (\omega_P/2)\sqrt{f/\varepsilon_\infty}$, depends only on the optical properties of the material.

Paper III also shows that the material will sustain bulk polaritons if,

$$f\omega_P^2 > \varepsilon_\infty\gamma^2/4\,. \tag{3.8}$$

Alternatively, it can be expressed as $g_B > \gamma/4$ [144, 145], which is the usual strong coupling criterion ($\Omega_R > \gamma_{avg}$), but with a lossless cavity mode ($\gamma_c = 0$) due to it being a plane wave.

As mentioned before, **Paper III** shows that the eigenfrequencies in the complex frequency plane have the same behavior as the conventional polaritonic eigenfrequencies in different interaction regimes. As expected, the real eigenfrequencies in Figure 3.7a show anticrossing. The upper limit of the LP is given by the uncoupled resonance frequency ω_0, but the lower limit of the UP is the renormalized resonance frequency $\omega_0^r = \sqrt{\omega_0^2 + 4g_B^2}$, as defined before. This opens a polaritonic gap where no modes are sustained. This gap can be approximated to $\Delta = \omega_0^r - \omega_0 \approx 2g_B^2/\omega_0$ when $(2g_B/\omega_0)^2 \ll 1$ [40, 127]. This area also corresponds to the spectral range of the Reststrahlen band, where the permittivity is negative, and thus, no modes can propagate in the material.

---

[12] Note that ω_c in the case of bulk polaritons is not the frequency of the photons in the cavity, because there is no cavity. Instead, it is the frequency of the plane wave propagating through the medium.

3.4.1 Asymmetric decay rates in bulk polaritons

The decay rates of the bulk polariton in Figure 3.7b are not equal at zero detuning. However, they cross at a detuning corresponding to $\omega_0^r = \omega_c$. Therefore, the linewidth asymmetry at zero detuning and the detuning at which the polaritons have the same linewidth increase with the coupling strength.

Moreover, **Paper I** shows that at zero detuning, the quality factors of the polaritons are equal, $\frac{\omega_+}{\gamma_+} = \frac{\omega_-}{\gamma_-}$. This equality automatically means that an asymmetry in the linewidths compensates for the difference in polaritonic frequencies when the modes split. Intuitively, this conservation means that both polaritons oscillate the same number of times before they damp.

These results open a series of questions. The Hopfield coefficients of the full Hopfield Hamiltonian are not equal at zero detuning [19]. My preliminary calculations show they should be equal at the renormalized frequency. If that is the case, should the zero detuning be defined with respect to ω_0^r? As described before, the appearance of ω_0^r occurs when considering the diamagnetic term in the Hamiltonian.

Moreover, the detuning at which the linewidths become equal is $\delta\omega = \Delta \approx 2g^2/\omega_0$. This expression is similar to the approximate change in ground energy in the USC regime [33, 145]. Does this mean the linewidth asymmetry can estimate the ground state's occupancy? The link between ω_0^r and the linewidth asymmetry in bulk polaritons makes the asymmetries a more general result with a potential fundamental meaning that requires further research.

3.5 Self-assembled Casimir polaritons

The plasmon–microcavity polaritons samples were carefully fabricated as described in subsection 5.2.1. Their properties are fixed after fabrication, as

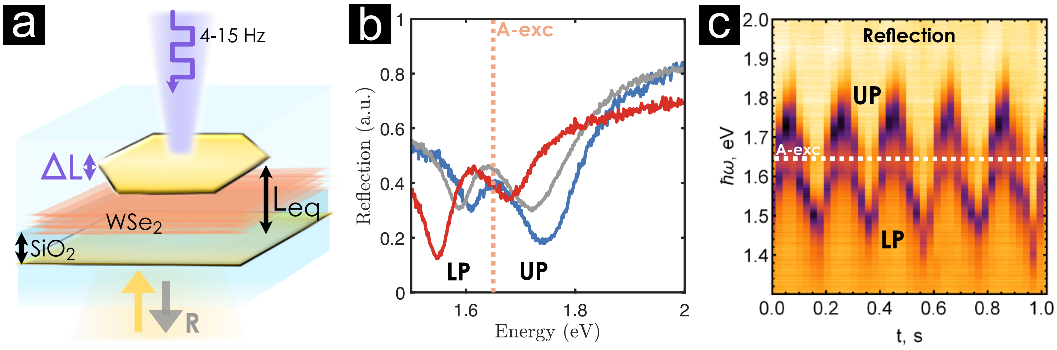

FIGURE 3.8: (a) Gold flake floating in water on top of few layers of WSe_2 deposited on SiO_2 on a gold mirror. Modulated laser irradiation at $\lambda = 455$ nm pushes the flake down, changing L_{eq}. (b) Normal incidence reflection spectra from the coupled system at different detuning of the cavity: red, zero, and blue detuning. The dashed line marks the energy of WSe_2 A-exciton. (c) Time-resolved normal incidence spectra of the modulated coupled system. Figure modified from [39].

with most polaritonic platforms. In fact, only a handful of platforms can actively adjust the properties of the cavity [146] or the material [147, 148] to tune polaritonic properties as coupling strength or polaritonic composition.

As discussed in section 2.5, FP cavities can be formed with floating gold flakes by Casimir forces. **Paper II** obtained polaritons by strongly coupling the A-exciton of WSe_2 to the self-assembled FP cavities. A few-layer WSe_2 flake was transferred on top of a SiO_2 spacer deposited on an evaporated gold mirror as shown in Figure 3.8a. Then, gold flakes floating in solution formed a microcavity around the WSe_2, resulting in self-assembled polaritons with a Rabi splitting above 100 meV.

In section 2.5, the resonance of the cavity depends on the total concentration of ions in the solution. However, the resonance also depends on the SiO_2 spacer thickness in this configuration. This configuration gives a broader frequency range tunability to couple to different materials [39]. The thickness and high-refractive index of the few-layer WSe_2 also add to the optical path. Figure 3.8b shows that coupling can occur with different detunings, where $\delta\omega = 0$ is in gray, the blue detuned cavity in blue, and the red detuning in red.

In addition to passive control of detuning, active control is also possible by using a laser to change the thickness of the cavity. The process involves using modulated laser radiation pressure to push the floating gold flakes vertically, as depicted in Figure 3.8a. The distance between the mirrors changes over time, causing a shift in the vacuum field, affecting the value of

g. Additionally, the change in L_{eq} changes the detuning between the two resonances, as shown in Figure 3.8c, enabling the tunability of the polaritonic composition. To quantify this effect, **Paper II** uses equation (3.2) to fit the data and obtain the Hopfield coefficients. Raising the intensity of the laser enhances the variation of ΔL, and all the effects discussed above.

Chapter 4

Cavity-free polaritons

This Chapter examines *cavity-free* or *self-hybridized* polaritons, where the photonic modes are sustained by the material's geometry, unlike conventional polaritons that require an external cavity. I provide an overview of cavity-free polaritons in various geometries, incorporating the findings in **Papers III**, **IV**, and **VI**.

Paper III theoretically demonstrated various geometries that sustain these polaritons for different materials. Then, **Paper IV** focused on measuring a planar geometry, where excitons in MoS_2 flakes hybridize to the photonic modes supported by the slab. Finally, **Paper VI** presents the results of measurements on water droplets in the IR spectral range.

The Chapter also includes unpublished experimental findings on hBN structures. Lastly, it discusses the limits and implications of self-hybridized polaritons.

4.1 Polaritons in 2D slabs

In a simple 2D slab, the edges of a material can reflect light well enough to form FP cavities, as shown in section 2.3. The photonic modes sustained by a thick 2D slab can be radiative (FP) or guided. According to equation (3.4), the Rabi splitting is maximum for a given coupling strength when $\gamma_c \rightarrow \gamma_0$. Therefore, depending on the decay rate of the material resonance, the Rabi splitting is larger with radiative or guided modes. Most materials have a small decay rate, $\gamma_0 \rightarrow 0$. Therefore, a larger Rabi splitting is easier to obtain with lossless waveguide modes ($\gamma_c \rightarrow 0$) than radiative modes. That is why the first cavity-free studies in planar cavities coupled excitons in J-aggregates to waveguide modes in the slab [149]. Additionally, 2D atomic crystals naturally stack, forming slabs that sustain photonic modes. Cavity-free polaritons have also been measured in WSe_2 with waveguide modes [150, 151]. Moreover, cavity-free vibrational polaritons were measured below the LL in a $\alpha-$lactose photonic crystal [152].

Cavity-free polaritons were later measured above the light line (LL) in J-aggregates [147, 153], and in TMDs [132, 154], including TMDs with in-plane anisotropy as ReS_2 [155].

However, most of these studies either do not mention the coupling strength or estimate it using a coupled oscillator model. In contrast, **Paper III** obtains the Rabi splitting directly from the difference between upper and lower polaritons' eigenfrequencies found via the pole-search method using the $\hat{S}$-matrix, as described in subsection 5.1.2. This approach obtains the radiative and waveguide eigenfrequencies of polaritons above and below the LL.

Paper III was purely theoretical, but **Paper IV** measures reflection spectra of MoS_2 slabs obtains and visualizes the polaritonic eigenfrequencies in the complex frequency plane, as we will see in the following section. **Paper III** presents the theoretical example of hBN slabs, and subsection 4.1.1 presents a simple experimental realization. However, these are preliminary results and require more theoretical work for a full interpretation.

4.1.1 Polaritons and perfect absorption in MoS_2 slabs

The goal of **Paper IV** was to measure polaritons above and below the light line (LL), as was theorized in **Paper III**. MoS_2 was used because its excitonic resonances are in the visible and because its high absorption around the C-exciton was promising for perfect absorption in ultrathin flakes as mentioned in section 2.2. Due to the high refractive index of MoS_2, thick flakes sustain FP modes above the LL and waveguide modes below the LL.

To measure reflection from the slab above and below the LL, we use an oil immersion objective that matches the refractive index of glass to illuminate the slab from the substrate, as shown in Figure 4.1a. All angles of incidence smaller than the critical angle of air/glass ($\theta_c = \arcsin 1/n_{glass} \sim 41.5°$) provide measurements above the LL, which is region **I** in Figure 4.1b. On the other hand, all angles larger than θ_c provide measurements below the LL.

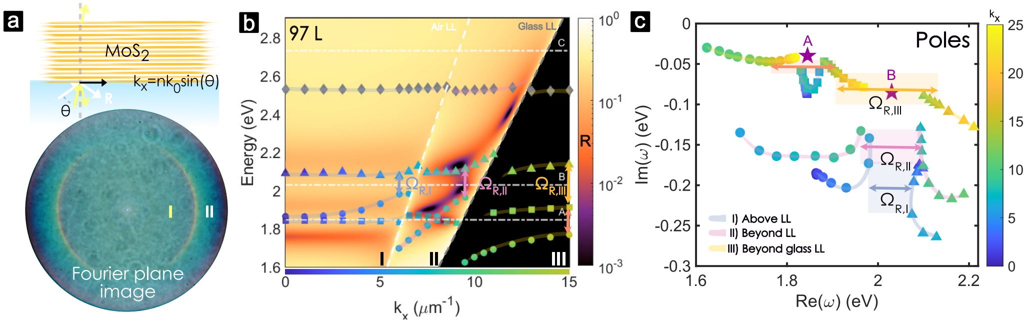

FIGURE 4.1: (a) *Top:* Schematic of the system. *Bottom:* True-color image of the reflected light from a 97L ($\sim$ 63 nm) MoS_2 flake in the Fourier Plane. (b) Calculated reflection of TM-polarized light from a 97L flake for various wavevectors, $k_x = k_0 n \sin\theta$. The real eigenfrequencies are plotted on top with markers of colors varying with the in-plane wavevector. The Rabi splitting is marked for each of the three regions: **I**) above the light line (LL) in blue, **II**) below the LL ($\theta > \theta_{c_{air}}$) in pink, and **III**) below the glass LL ($\theta > \theta_{c_{glass}}$) in yellow. (c) Eigenfrequencies in the complex frequency plane for all regions. The stars mark the uncoupled excitons. Image modified from [41].

Fourier imaging (described in subsection 5.3.1) allows us to measure the reflected spectra at different angles of incidence. The true-color image of the Fourier plane of a 97L slab in Figure 4.1a shows the colors generated by the photonic modes. Fabry-Pérot modes (region **I**) give the turquoise color around the center, and the dispersion of leaky modes results in the fast-changing colors of the region **II**.

Paper IV shows the spectra measured for various angles. The measurements correspond well with the calculated reflection via TMM shown in Figure 4.1b. The TMM calculations were used to build the $\hat{S}$-matrix and find the system's eigenfrequencies as described in subsection 5.1.2. The eigenfrequencies obtained with the pole-search method are shown with markers on top of the reflection colormap. The marker color varies with k_x.

The first remark is that the eigenfrequencies and the minima in reflection do not match, unlike in the metallic microcavity discussed in the previous chapter. This mismatch is because the two scattering channels for light above the LL are not symmetric. One of these channels is glass, and the other is air. This asymmetry leads to a mismatch between the observable (reflection) and the eigenfrequencies.

There have been discussions about the most accurate observable to obtain the Rabi splitting [156]. According to the literature, absorption is the closest observable to the eigenfrequencies [132, 157]. However, even absorption may not perfectly correspond [158]. In our case, the absorption spectra match better with the eigenfrequencies, as shown in **Paper IV**. This is an important remark because the apparent splitting in the reflection in region **I** could be mistakenly attributed to polaritons when, in fact, it is an interference effect resulting from two scattering channels. However, it could be easily mistaken for strong coupling, and one could even determine its coupling strength using the coupled oscillator model. To avoid this problem, we calculated the eigenfrequencies using the pole-search method to avoid this potential error. It is crucial to handle splitting in measurable observables with care [94]. I will return to a similar message when discussing polaritons in water droplets.

The second remark is that the anticrossing observed for the B-exciton in all three regions in Figure 4.1b varies depending on the region. Region **I** has the smallest value, and region **III** has the highest value because the decay rates decrease until in region **III**, the waveguide mode is lossless.

The advantage of using the complex frequency plane in Figure 4.1c is that it is easy to distinguish between weakly and strongly coupled modes. The A-exciton in region **I** is weakly coupled due to its trajectory in a circle around the uncoupled exciton (star). In contrast, the B-exciton shows a polaritonic gap in all regions. The A-exciton only shows the gap in region **III**.

Finally, **Paper IV** shows that the dips in reflection in Figure 4.1b correspond to points perfectly absorbing TM-polarized light. Therefore, this simple unpatterned MoS_2 flake on glass can sustain polaritons while also perfectly absorbing light.

4.1.2 Polaritons in hBN slabs

Paper III showed the anticrossing of the eigenfrequencies of hBN, another 2D atomic crystal. We chose a thick ($L = 1.75\ \mu m$) slab to tune the first FP mode at normal incidence with the TO phonon, $\omega_0 = 0.169$ eV. The eigenfrequencies show anticrossing above and below the LL in Figure 4.2a. The Rabi splitting with the first mode above the LL is indicated in blue, while the one below is in yellow. The uncoupled modes are marked in lines, and the hybridized ones are in markers. Unlike the previous analysis of MoS_2 on glass, here we only observe two regions, above and below the LL. There is no intermediate region because there is no substrate.

In Figure 4.2a, the polaritonic gap is marked. As explained earlier, the polaritonic gap refers to the region between two phonon resonances: the

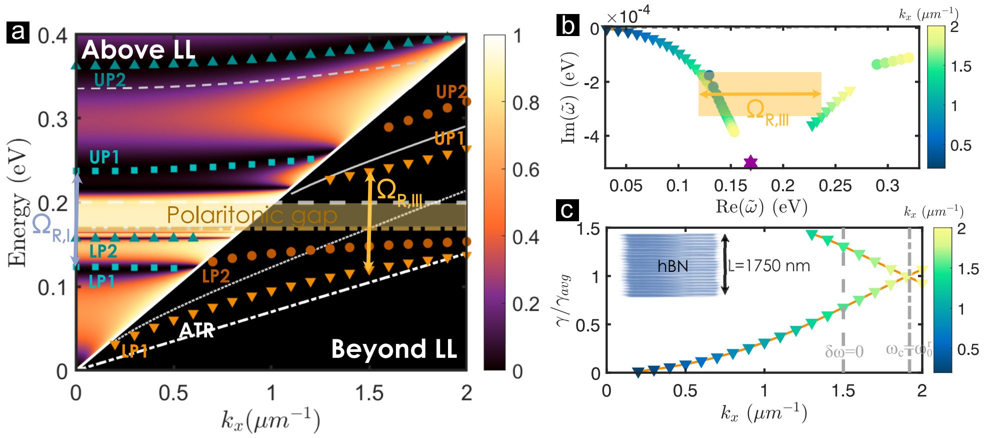

FIGURE 4.2: (a) Calculated reflection (TE polarization) and eigenfrequencies of a $L = 1750$ nm thick slab of hBN. The markers show the polaritonic eigenfrequencies with the first and second FP and waveguide modes. The polaritonic gap between transverse (TO) and longitudinal (LO) photons is shaded in yellow. The uncoupled modes are in dashed, dotted, and dot-dashed lines. The white dot-dashed line marks the line along which the ATR measures. (b) Eigenfrequencies of the modes below the LL in the complex frequency plane. The Rabi splitting is marked with an orange arrow. (c) Asymmetry of the normalized decay rate of polaritons resulting from hybridization with the first waveguide mode. The dashed vertical line marks the zero detuning $\delta\omega = 0$, and the dot-dashed line marks the waveguide mode in resonance with the renormalized frequency ω_0^r. Figure modified from [40].

uncoupled phonon resonance (ω_0) and the renormalized resonance (ω_0^r). For hBN, this gap corresponds to the Reststrahlen band between the transversal (TO, ω_0) and the longitudinal (LO) phonons.

Figure 4.2b illustrates the eigenfrequencies in the complex frequency plane. A shaded rectangle connects the eigenfrequencies at $\delta\omega = 0$. Similar shaded rectangles can be found in the complex frequency plane plots throughout the thesis and the appended papers. However, the papers do not address the full significance of these rectangles. If the polaritons had the same decay rate at zero detuning, these rectangles would be just a line (Rabi splitting). The height of the shaded area is determined by the polaritonic asymmetric linewidths described in subsection 3.4.1 and in **Paper I**. To better visualize this, Figure 4.2c displays the normalized polaritonic decay rates of the first waveguide mode for various k-vectors (varying detuning). The dashed line marks the wavevector corresponding to zero detuning for the first uncoupled waveguide mode (dotted line in Figure 4.2a). In contrast, a dot-dashed line marks the wavevector at which the renormalized frequency is at zero detuning. Hence, polaritonic decay rates of hBN polaritons below the LL exhibit the same asymmetric linewidth behavior observed for bulk polaritons in Figure 3.7.

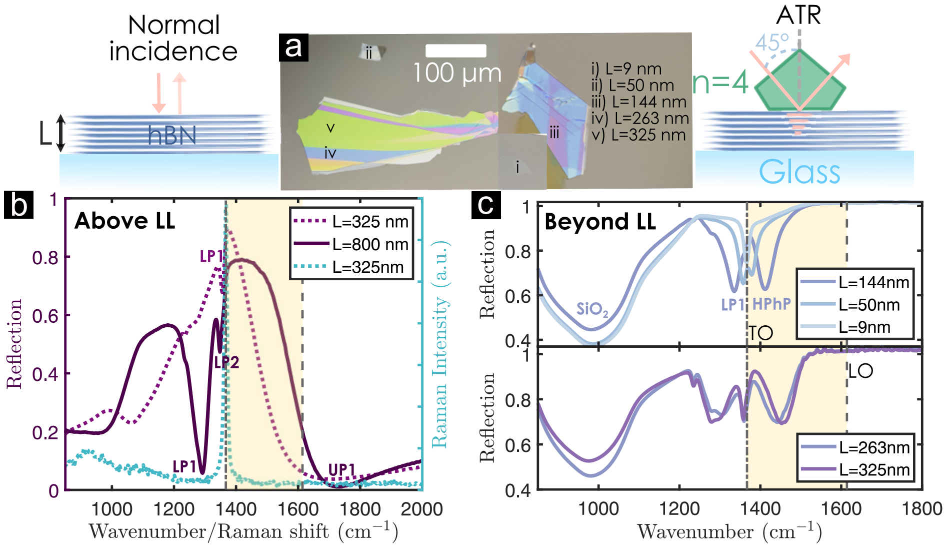

FIGURE 4.3: (a) Bright-field image of hBN flakes on glass. The colors are given by the FP modes sustained by the different thicknesses, L. (b) Normal incidence reflection from an hBN slab of $L \sim 325$ nm (dotted line) and $L \sim 800$ nm (solid line). The characteristic hBN Raman peak (~ 1367 cm^{-1}) is shown in blue. The Reststrahlen band between transverse (TO) and longitudinal (LO) photons is shaded in yellow. (c) Attenuated total reflectance (ATR) measurement of hBN slabs of different thicknesses. The Reststrahlen band is shaded in yellow.

We conducted preliminary experiments on hBN slabs, similar to MoS$_2$. Figure 4.3a shows hBN slabs of various thicknesses. The colors show that they sustain FP modes in the visible. However, the TO phonon is in the infrared, $\omega_0 = 0.169$ eV $= 1367$ cm^{-1}. Thus, Fourier-transform infrared spectroscopy (FTIR, described in subsection 5.3.3) was used to obtain the reflection spectra. The normal incidence reflection spectra of a "thin" slab with $L = 325$ nm (dotted line) shows only a lower polariton slightly red-detuned from the TO (subsection 4.1.2). Increasing the thickness to $L = 800$ nm decreases the detuning with the first FP mode. A first LP and UP are clearly visible for this thickness, and a slight second LP appears. Even thicker samples are required for the first FP mode to be zero detuned at normal incidence, but they are challenging to obtain by mechanical exfoliation and transfer (see subsection 5.2.2). Even though the measurement at normal incidence presented in Figure 4.3b is straightforward, I have not seen these hBN cavity-free polaritons above the LL reported in the literature.

However, bare hBN slabs are known to sustain other polaritons [64, 159]. It is important to understand the difference between those polaritons and the cavity-free polaritons discussed here. Usually, those polaritons refer to surface polaritons that propagate along an interface between a dielectric material and a material with negative permittivity, well-known since the 70s [86]. These are the same type of polaritons as surface plasmon polaritons (SPPs) [65], where a metal provides the negative permittivity. Here, the strong oscillator strength of the phonons results in negative permittivity. Thus, they are called surface phonon polaritons (SPhPs). As such, SPhPs appear only in the Reststrahlen band (shaded in yellow in Figure 4.3b), where the permittivity turns negative[1]. Similar to SPPs, they are excited below the LL for TM-polarized light. Therefore, they are not visible in the calculation for TE-polarization in Figure 4.2a. However, they are present in the measurements below the LL in Figure 4.3b.

Measurements below the LL in IR were done using attenuated total reflectance (ATR, as described in subsection 5.3.3) in FTIR with unpolarized light. ATR uses a germanium crystal ($n = 4$) to excite below the LL from a medium with a higher refractive index similar to the MoS_2 setup. The line along which the ATR measures is marked in Figure 4.2a with a dot-dashed white line[2]. Figure 4.3b shows the reflection for different hBN slab thicknesses. The thinnest one ($\sim$ 9 nm) shows a resonance at the TO phonon. Thicker slabs (50 and 144 nm) show a lower polariton dip for frequencies below the TO phonon and a hyperbolic phonon polariton (HPhP) dip for higher frequencies. For even thicker slabs (263, 325 nm), more dips are measured below the TO, corresponding to hybridization with higher-order waveguide modes of both polarizations. The dip in the Reststrahlen band gets broader and blue shifts because the dip integrates the contribution of several HPhPs. No UP is observed because they usually appear at smaller k-vectors as shown in Figure 4.2a.

Although these simple and fast measurements provide insight, to understand Figure 4.3c, calculations including both polarizations and resolving all HPhPs in the Reststrahlen band are required. Also, detailed pole-search calculations with the correct structure (glass/hBN/Ge) can be done to determine the contributions of the eigenfrequencies to the measured dips. Regardless, there are considerable limitations in the

---

[1] Many polar crystals have strong phonon resonances that sustain SPhPs [63]. However, hBN is a special material among them because it is anisotropic. The permittivity in-plane is very different from the out-of-plane one. It is so different that it sustains two Reststrahlen bands in different frequency regions, one in-plane (upper band in 1367-1614 cm^{-1}) and one out-of-plane (lower band in 760-825 cm^{-1}. This kind of material is called hyperbolic, which is why polaritons in hBN are better known as hyperbolic phonon polaritons (HPhP)

[2] This is just a guideline to understand the concept of the measurements, but those calculations are far from the actual measured system. A specific calculation is required for the hBN slab between glass and germanium.

k-vector resolution with these measurements. The better alternative (but not so easy to access) is using a scanning near-field optical microscope (SNOM) [64].

4.2 Polaritons in 1D infinite cylinders

Paper III shows that optical resonances in the cylinders hybridize with the electronic transition in the perovskite $CsPbCl_3$. Like slabs, cylinders sustain radiative (above the LL) and waveguided modes (below the LL), and all can be strongly coupled to the material. This thesis did not contribute to such experimental studies. However, polaritons have been demonstrated in several material platforms, including perovskite nanowires [110, 160], nanofibers of organic dyes [161], and inorganic semiconductors nanowires [162].

Recently, polaritons in self-hybridized nanowires of organic semiconductors (J-aggregates and H-aggregates) have been shown to have five times higher energy transport velocity than the expected for a non-polaritonic exciton [163]. Even though they only resolve Rabi splitting above the LL in about $\sim 30\%$ of the measured regions[3], they measured the energy transport effect for all the regions. This may be related to the fact that the nanowires are also strongly coupled with waveguide modes below the LL, even though no Rabi splitting is measurable above the LL. These observations highlight the impact of self-hybridized polaritons on material properties, particularly the importance of considering the coupling with waveguide modes. A more extended discussion about waveguide modes is found in subsection 4.4.3.

4.3 Polaritons in 0D geometries

Platts *et al*. [164] first theorized hybridizing excitons in a GaAs sphere to its whispering gallery modes. These were the first theorized self-hybridized polaritons, to my knowledge. Later WS_2 slabs were shaped into nanodisks and reached strong coupling with the A-excitons [165]. **Paper III** proposed that water droplets exhibit strong coupling in theory. **Paper VI** subsequently observed this phenomenon in laboratory mists. Moreover, hBN was recently

---

[3] The authors attribute this to potential variations in the oscillator strengths.

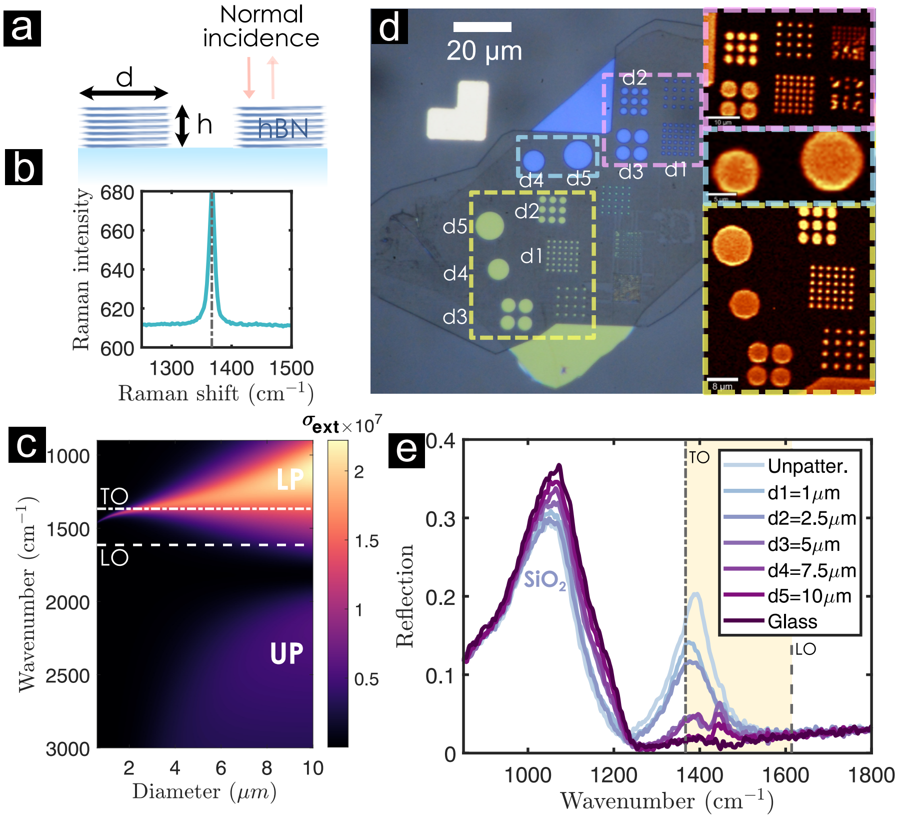

FIGURE 4.4: (a) Shematic of normal incidence reflection of hBN nanodisks on glass. (b) Raman signal for all nanodisks is the same as the unpatterned hBN with a main peak at 1367 cm^{-1}. (c) Extinction cross-section calculation of an isotropic ellipsoid with the in-plane permittivity of hBN. The height of the ellipsoid was 140 nm for various diameters. (d) *Left:* Bright-field image of an hBN flake patterned with nanodisks of various diameters, d1=1 μm, d2=2.5 μm, d3=5 μm, d4=7.5 μm, d5=10 μm. The blue flake has h = 140 nm, and the yellow h = 213 nm. *Right:* Raman intensity of the 1367 cm^{-1} peak on the patterned nanodisks. No additional peaks were observed. (d) Normal incidence reflection from the nanodisks patterned with h = 140 nm for various diameters.

shaped into nanodisks to target strong coupling to the TO phonon [166]. Here, I describe the last three cases.

4.3.1 Polaritons in hBN nanodisks

As often happens in science, similar ideas often occur to several people around the same time. In our case, we also created hBN nanodisks to combine the TO phonon with Mie resonances supported by the nanodisks. The schematic of the system measured at normal incidence is shown in Figure 4.4a. The nanodisks were patterned on hBN flakes with thicknesses of 140 nm and 213 nm, as shown in Figure 4.4d.

The quick calculations performed on the hBN ellipsoids extinction cross-section, shown in Figure 4.4c, were done as a guide for the sizes to fabricate. These calculations have two major approximations. Firstly, they assumed an ellipsoidal shape, and secondly, the material was approximated to an isotropic permittivity, with the in-plane permittivity of hBN. Although these calculations provided an initial idea, more accurate calculations are required to understand the experimental outcomes thoroughly.

Despite the heavy approximations, the calculations in Figure 4.4c provide insights. Here, the resonances appear as a maximum in extinction. They show that for a height of 140 nm, only diameters above 4 μm have visible UP and LP peaks in extinction. These are phonon modes hybridized with the Mie modes, resulting in UP and LP. The peak is inside the Reststrahlen band for smaller diameters. As a result, the resonance is similar to LSPR in metals, resulting in only one peak for smaller diameters.

Reflection from the fabricated arrays was measured as shown in Figure 4.4d using a normal incidence FTIR microscope, as described in subsection 5.3.3. The main changes for various radii occur inside the Reststrahlen band but only for larger nanodisks. The unpatterned flake shows a weak reflection peak given by the TO phonon. The peak is damped with the smaller diameters, but no other changes are observed. However, for larger diameters, the signal varies considerably. Unfortunately, this contradicts the simple calculation that expected changes inside the Reststrahlen band for smaller disks. Therefore, interpreting the data requires simulations in reflection with an anisotropic hBN permittivity.

The main goal of this project was not only to show hybridization with Mie modes but also to measure Raman scattering from the polaritons. We were looking for a nanodisk size-dependent Raman signal, which should only depend on the material's properties in the absence of polaritons. For that, Raman was measured at normal incidence, but we always obtained the same hBN 1367 cm^{-1} peak shown in Figure 4.4b. The large area scan on the right of Figure 4.4b shows the Raman intensity of the common hBN 1367 cm^{-1} peak. This central peak of hBN never varied, and no other peaks were detected.

We now understand that this project failed because the phonon measured by Raman is not the same as the phonon strongly coupled to IR light. They have practically the same energy but correspond to different vibrations [167]. As a result, the Raman signal always came from an uncoupled phonon.

For this project to work, we just need to change the material platform to a non-centrosymmetric crystal. The problem with hBN is that given its symmetry, the mutual exclusion principle states that an IR active mode is not Raman active [168]. However, breaking the symmetry allows for the same phonon to be Raman and IR active. Only in that case could the phonon coupled to IR Mie resonances show Raman signal from the polaritons.

4.3.2 Polaritons in water droplets

Finally, **Paper III** considers a water sphere and theoretically shows that Mie resonances (described in subsection 2.3.3) hybridize with the vibrational phonons in water. As shown in Figure 4.5c, the Rabi splitting (orange arrow) with the first $a_{l=1}^{N}$ Mie modes increases for larger N due to better confinement of the mode and a corresponding decrease in its decay rate. However, this increase is ultimately limited by the bulk Rabi splitting $2g_B$, as described in **Paper III**. The goal of **Paper VI** was to show that water droplets in mist sustain cavity-free polaritons experimentally.

An initial trial was to individually measure single droplets in an FTIR microscope, as was done for the hBN flakes and nanodisks. For that, I used spiderwebs to hold water droplets formed by a nebulizer as shown in Figure 4.5a. However, the droplets evaporate in about 10 seconds, and a single scan of the FTIR microscope takes several minutes. The droplets could stabilize if the ambient were humid. However, the main problem with this approach was that the droplets stabilized around sizes of 30 μm, which was far from the diameters calculated in **Paper III**.

For sizes below 5 μm, the effect of the self-hybridized polaritons is more notable in extinction. Figure 4.5d shows a clear "splitting" in the extinction spectra given by the coupling between the bare Mie modes (dashed gray line) and the O–H stretch resonating at $\omega_1 = 0.418$ eV (blue dotted line) in a droplet of $R = 2.5\ \mu m$. In contrast, a droplet with $R = 30\ \mu m$ shows a flattening behavior around the O–H stretch (marked in a circle in Figure 4.5e). This flattening pattern continues as the size increases.

Regardless of the size, the difference between the uncoupled spheres and the hybridized ones is clear. Even "splitting" is visible for the bending mode resonating at $\omega_2 = 0.2$ eV for $R = 30\ \mu m$. These "splittings" marked in red arrows in Figure 4.5d,e are not Rabi splittings, but they result from the superposition of several Mie modes splitting with the resonant mode.

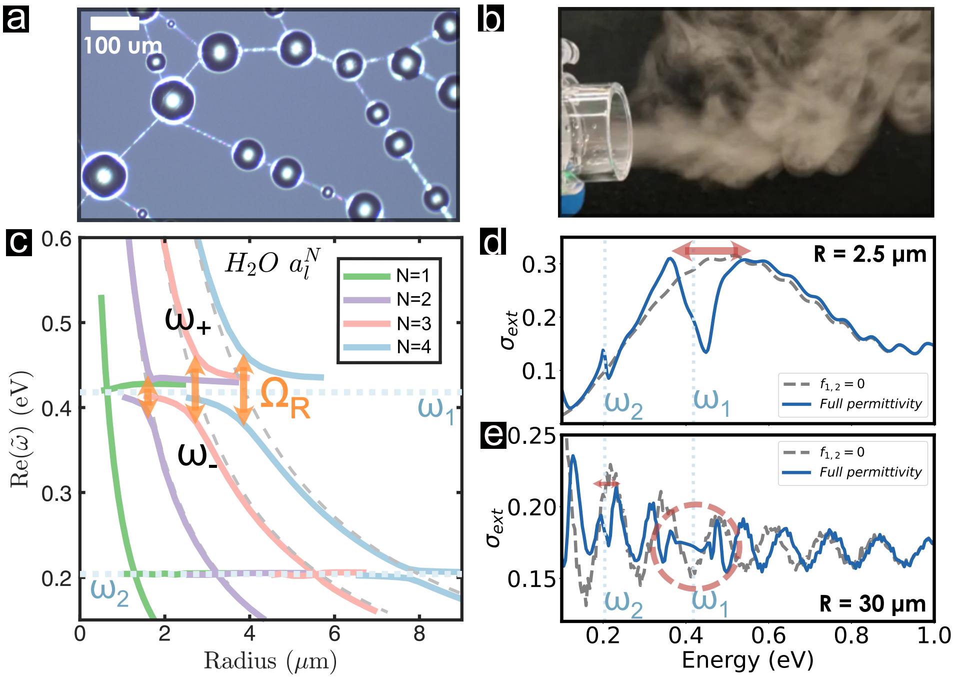

FIGURE 4.5: (a) Water droplets on a spiderweb. (b) Mesh nebulizer producing mist with water droplets with sizes below 5 μm. (c) Eigenfrequencies of water droplets of different sizes. The uncoupled eigenfrequencies are marked in blue dotted lines, and the extinction of the uncoupled spheres is in a gray-dashed curve. The Rabi splitting is marked with orange arrows. (d) Extinction cross-section of a water sphere of $R =$ 2.5 μm with (blue curve) and without the contribution of vibrational modes (uncoupled sphere shown in the gray dashed curve). (e) Extinction cross-section of a water sphere of $R = 30$ μm. Figure modified from [43].

To understand why they are not Rabi splittings, let us remember that extinction cross-sections (σ_{ext}) are the sum of all Mie modes in a sphere, as described in equation (2.8). Therefore, σ_{ext} includes all the modes in Figure 4.5c, all higher multipolar modes, $l > 1$, and all b_l^N modes. Note that most Mie modes are not at zero detuning with the resonance for a fixed radius. Therefore, most contributions to the extinction of a sphere of a given single radius will be of the splitting at high detuning.

Instead of measuring single droplets, **Paper VI** presents transmission measurements through the mist generated by a commercial vibrating mesh nebulizer (Evolu Air Pro), as demonstrated in Figure 4.5b. The mist produced by these nebulizers has a narrow droplet distribution due to their typical usage in drug delivery, with a median size requirement of below 5 μm [169, 170].

Paper VI fits the experimental optical density with a calculated one [171] that includes the extinction cross-section of water spheres with a size distribution between $0.5 - 4.5$ μm. It also shows that water droplets above

$\sim 2.7\ \mu m$ are strongly coupled. Therefore, a mix between polaritonic and non-polaritonic droplets gives the total optical density. **Paper VI** shows the difference between the measured optical density and the calculated one if the droplets would not interact with its vibrational modes.

We also studied heavy water (D_2O) in **Paper VI** to ensure the optical density signal is due to strong coupling. Its optical properties are similar to water, but the vibrational modes are shifted to lower energies due to its heavier mass. As a result, the measured "splitting" in optical density shifts to those frequencies. In this case, the radii cutoff to become polaritonic increases to $\sim 3.7\ \mu m$.

Therefore, the measured mist contains polaritonic droplets. The studied droplet sizes are similar to those found in some fogs [172, 173]. Also, most clouds are formed by droplets with sizes above the polaritonic threshold [174]. Consequently, polaritonic water droplets occur in clouds naturally.

Recent experimental [175–177] and theoretical [178] studies have increased interest in hybridized water. These studies on conventional polaritons have found that water properties undergo modifications in the strong coupling regime. Understanding the polaritonic nature of water droplets will hopefully lead to further research to better understand their impact.

4.4 Limits and applications for cavity-free polaritons

4.4.1 Critical size

The previous section pointed out that not all sizes in droplets that sustain Mie resonances can hybridize with the O–H stretch in water. In general, for any material, the critical radius depends on ω_0 and the material's background permittivity. The higher ε_∞, the smaller the spheres can be to sustain polaritons.

All the geometries studied in **Paper III** have a critical size below which no polaritons are sustained. In planar and cylindrical structures, the first waveguide mode gives the limit. **Paper III** provides a rough approximation of the minimum thickness required to sustain Rabi splitting below the LL for the 1st TE waveguide mode in slabs in terms of the optical properties of

TABLE 4.1: Calculated values of the bulk Rabi splitting, $2g_B$, η and the minimal slab thickness needed to sustain polaritons, L_{min}.

Material	$2g_B$ **(eV)**	η	L_{min} **(nm)**
Water	0.1	0.12	137.3
hBN	0.12	0.35	2.6
Perovskite ($CsPbCl_3$)	0.382	0.06	4.4
J-aggregates (TDBC)	0.455	0.11	9.7
MoS_2 A-exciton	0.328	0.09	2.4
MoS_2 B-exciton	0.524	0.13	2.1

the material. The thickness is then given by,

$$L_{min}^2 > \frac{\gamma^2}{2k_0^2(f\omega_P^2)\sqrt{\varepsilon_\infty - 1}} . \tag{4.1}$$

Here, k_0 is the wave vector in vacuum. This results in different thicknesses for different materials (see Table 4.1). We can only offer a rough guideline with this equation. It is important to find the eigenfrequencies for more accurate identification. Approximately, the thickness threshold for 2D crystals here is below 3 nm for slabs in vacuum. Interestingly, polaritons below the LL have recently been measured in a WSe_2 few-layer slabs as thin as 9 nm [151] on SiO_2.

Note that the structures are considered in vacuum, so the critical sizes may vary in a different medium, such as placing it on a substrate. Of course, by matching the surrounding media refractive index with the structure, the optical resonances disappear along with the polaritons.

4.4.2 Maximum Rabi splitting

Regardless of the photonic mode, all the materials and geometries studied exhibit a Rabi splitting below the bulk Rabi splitting, $2g_B = \omega_P\sqrt{f/\varepsilon_\infty}$. Other groups have also reported this observation [128, 164]. This limit applies to both cavity-free and conventional polaritons. A summary of the bulk coupling strength of all the materials studied in this thesis is found in Table 4.1. The table also shows that some of these materials can reach the USC regime, $\eta \geq 0.1$.

The bulk coupling strength can be used as a guideline to determine which materials can be hybridized with light. For a resonance of interest, one can fit its permittivity with a Lorentzian equation and verify that $f\omega_P^2 > \varepsilon_\infty\gamma^2/4$

to determine if a material sustains bulk polaritons. If so, the material can sustain bulk polaritons and may be strongly coupled to other photonic modes. Conversely, if a material cannot sustain bulk polaritons, no cavity will provide a photonic mode that can strongly couple to it.

4.4.3 Implications of cavity-free polaritons

Before closing the chapter, I would like to discuss the implications of the existence of cavity-free polaritons. One of the promises of polaritons is that they can tune materials' properties because of their hybrid nature [179]. Conventional polaritons have shown their impact in a few material characteristics like exciton transport [180–184], charge transport [185], photochemical reactions [1–3, 186], and ground-state chemical reactivity [187, 188]. Reaching even polariton condensation [12, 189].

For some of these applications, having an external cavity is necessary. For example, in long-range energy transfer [7, 190], the cavity mediates the transfer between two materials far from each other but that share the same photonic mode. However, other applications do not need an external cavity. For example, exciton transport enhancement has been recently obtained in cavity-free nanowires [163]. Also, it has been recently shown that self-hybridized polaritons affect magneto-optical properties of a van der Waals material [191].

The concept of cavity-free polaritons has only recently gained interest, so we will probably see more applications in the coming years. It would be particularly intriguing to find out whether ground-state chemical [8] reactivity can occur in cavity-free structures.

Interestingly, ground-state chemistry changes have been so far solely measured in conventional vibrational polaritons when the cavity and the vibrational mode are at zero detuning and normal incidence ($k = 0$, above the LL) [8]. As of yet, there are no conclusive theoretical explanations for these observations [122], which makes it difficult to understand if cavity-free polaritons would show the same changes. One hypothesis suggests that the density of states provided by bulk and cavity-free polaritons is not as large as that provided by a metallic cavity in conventional polaritons and, thus, cannot show the same results [192].

To determine the changes in polaritonic chemistry, the reaction speed is usually compared in a cavity at zero detuning versus a detuned cavity or with mirrors and without mirrors. Let us address both benchmarks considering the existence of cavity-free polaritons above and below the LL.

Polaritonic chemistry effects have been only observed for cavity thicknesses for which the Rabi splitting is visible at normal incidence. In order to determine the effects, the reaction speed is often compared to a benchmark. Two comparisons are often made: i) a cavity at zero detuning vs. a detuned cavity, or ii) a cavity with metallic mirrors vs. the same cavity without mirrors. Let us address both benchmarks considering the existence of cavity-free polaritons above and below the LL.

For the first one, the crucial need for zero detuning at k=0 is very intriguing. Similar to cavity-free slabs, conventional microcavities also sustain waveguide modes with which the phonon strongly couples [193]. Therefore, even if the detuning is high at normal incidence, several waveguide modes will be at zero detuning at higher k-vectors. The community is working on many of the puzzles regarding these observations, and I look forward to reading works on this in the future.

On the second one, cavity-free polaritons can still be present after removing the mirrors. Therefore, one needs to be careful with the thickness and refractive index contrast because, in some cases, there may even be cavity-free optical modes at zero detuning at normal incidence. To avoid polaritons and get a proper benchmark, one needs to match the solution's refractive index or decrease the thickness of the "uncoupled" material below the critical value. On the bright side, very recent studies are now considering this by comparing the effects of polaritons in cavities with mirrors, with one mirror, and without mirrors [194, 195].

In this chapter, we have discussed that Lorentz materials can form polaritons without requiring an external cavity. Such materials can be reshaped to support optical modes for the material to self-hybridize. Theoretical discussions have covered slabs, cylinders, and spheres. Experimental studies were conducted on MoS_2 and hBN slabs, hBN nanodisks, and water spheres. Polaritons can be easily fabricated and occur naturally, for instance, in water droplets in clouds.

The material's capability to form polaritons with any cavity (conventional or a self-hybridization configuration) depends solely on its optical properties since the bulk polaritons seem to be the maximum attainable Rabi splitting.

Thus, a quick way to test if a material could reach strong coupling is to fit a Lorentzian to the resonance of interest and calculate $2g_B = \omega_P\sqrt{f/\varepsilon_\infty}$ and compare it to its decay rate.

As described in this chapter, new experiments continue to show cavity-free self-hybridized polaritons and their potential to change materials properties [152, 153, 163, 191]. Self-hybridized polaritons offer a unique platform for studying polaritonic changes in materials, particularly in polaritonic chemistry, as they provide polaritons without any additional interactions with the external cavity. This allows for better isolation of the effects of polaritons when characterizing the material properties.

Chapter 5

Research methods

The previous chapters have focused on the results of the thesis. This chapter describes the calculation, fabrication, and optical characterization methods. The chapter is divided into three parts.

The first section covers the theoretical tools and concepts used in the thesis. It explores quasinormal modes of open systems and how to obtain them using a pole-search method in the complex frequency plane and the scattering matrix.

The second section focuses on nanofabrication. It describes the methods used to fabricate microcavity–plasmon polaritons, self-assembled polaritons, and how to exfoliate, transfer, and pattern 2D crystals.

The final section describes the experimental setups used for optical characterization, including Fourier plane spectroscopy, dynamic modulation of self-assembled polaritons, Fourier-transform infrared spectroscopy (FTIR), and optical levitation of water droplets.

5.1 Analytical calculations

5.1.1 Quasinormal modes in open systems

All the calculations in this thesis considered open systems (also called non-conservative or non-Hermitian) with radiative losses to the environment. The eigenmodes of these systems are called "quasinormal modes" (QNMs) to differentiate them from the eigenmodes in closed systems called "normal modes". In waveguide theory, these modes are also called "leaky" modes [196].

The QNMs are solutions to the source-less Maxwell's equations. Therefore, they do not depend on the excitation field. In the case of open systems, the equations should obey the Silver-Müller (SM) radiation conditions, which state that there should be no sources of radiation in the far-field, such that the energy flow is only outgoing [79]. Let us consider the source-less Maxwell's equations with no free charges in a matrix form, such that they look like an eigenvalue problem [78],

$$\begin{bmatrix} 0 & \mathrm{i}\varepsilon^{-1}(\mathbf{r},\tilde{\omega})\nabla\times \\ -\mathrm{i}\mu^{-1}(\mathbf{r},\tilde{\omega})\nabla\times & 0 \end{bmatrix} \begin{bmatrix} \tilde{\mathbf{E}}(\mathbf{r}) \\ \tilde{\mathbf{H}}(\mathbf{r}) \end{bmatrix} = \tilde{\omega} \begin{bmatrix} \tilde{\mathbf{E}}(\mathbf{r}) \\ \tilde{\mathbf{H}}(\mathbf{r}) \end{bmatrix}. \tag{5.1}$$

The eigenvectors are the QNMs' spatial field distributions $[\tilde{\mathbf{E}}(\mathbf{r}), \tilde{\mathbf{H}}(\mathbf{r})]^{\mathrm{T}}$ and the eigenvalues are its complex frequencies, $\tilde{\omega}_n = \omega_n - i\gamma_n/2$ [78, 79]. The real part is the measurable resonant frequency, ω_n, and the imaginary part is the decay rate, associated with its lifetime, $\tau_n = 1/\gamma_n$. This means that the field decays exponentially with time, $\mathbf{E}(\mathbf{r},t) = \tilde{\mathbf{E}}(\mathbf{r})e^{\mathrm{i}\omega_n t}e^{-\gamma_n t}$, and similarly for $\mathbf{H}$.

Resonances are a manifestation of QNMs. A figure of merit of the damping for resonances is the quality factor, $Q = \omega_n/\gamma_n$. The measurable quantity related to γ_n is the resonance's full width at half maximum (FWHM). The Q–factor physically corresponds to the resonance's number of oscillations before damping.

Among the various methods to find QNMs [78, 79], it is possible to compute them by searching poles in the complex frequency plane of the system's electromagnetic response [197]. This pole-search approach uses that if a driving field approaches a QNM eigenfrequency, its resonator response will diverge. We look for points where the scattered field diverges. Therefore, we calculate the systems' scattering matrix ($\hat{S}$) and find the poles of its eigenfrequencies [74]. In practice, one calculates $\det \hat{S}$ in the complex frequency plane and looks for points where it diverges.

5.1.2 Scattering matrix

When an incoming field interacts with a system, the scattering matrix relates the incoming and scattered fields after the incoming field interacts with the system, $\mathbf{E}_s = \hat{S}\mathbf{E}_i$. The $\hat{S}$matrix is built by linking the amplitudes of the incoming waves ($\mathbf{s}^+ = \{s_1^+, s_2^+, ..\}$) with those of the outgoing waves ($\mathbf{s}^- = \{s_1^-, s_2^-, ..\}$), $\mathbf{s}^- = \hat{S}\mathbf{s}^+$ [74], as shown in Figure 5.1a for M scattering channels.

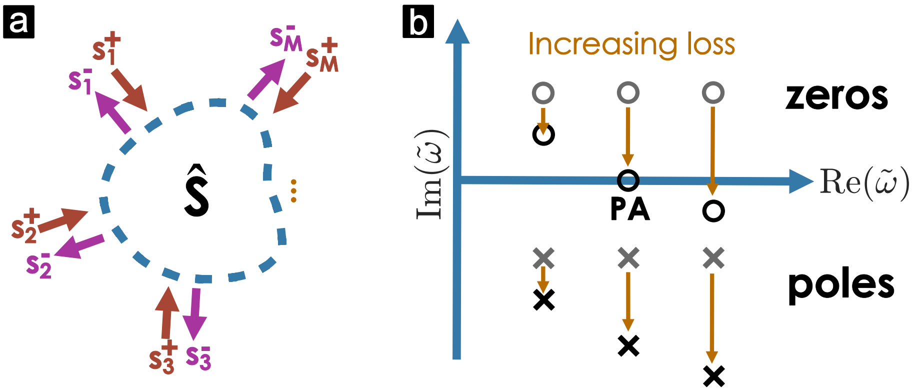

FIGURE 5.1: (a) Schematic of the scattering matrix with M scattering channels. (b) Poles (cross) and zeros (circle) of the $\hat{S}$-matrix without for a material without loss or gain in gray and increasing loss in black. The point when the zero is on the real axis is where perfect absorption (PA) occurs when there is only one scattering channel.

Before diving into the specific geometries calculated for this thesis, let us understand some generalities of the $\hat{S}$-matrix. The $\hat{S}$-matrix has both zeros ($\hat{S}\mathbf{s}^+ = 0$) and poles ($\hat{S}\mathbf{s}^+ = \infty$) [73]. In the absence of loss and gain in the material, the zeros and poles appear in pairs in the complex frequency plane and are related by complex conjugation. The zeros appear in the upper plane, and the poles are in the lower plane, as shown in the schema in Figure 5.1b. Their distance to the real axis depends on the total radiative losses. For example, waveguide modes have poles almost at the real axis since they are practically lossless.

Increasing the amount of material loss (γ in $\varepsilon(\omega)$) has the effect of pulling down the zeros and poles to the lower plane. The larger the loss, the lower both are. The point where the zeros cross the real axis is a point with no outgoing fields. This point corresponds to perfect absorption if the system has only one scattering channel, as in **Paper VI**. However, in systems with more scattering channels, this corresponds to coherent perfect absorption (CPA) [73].

Now, let us continue to calculate the $\hat{S}$-matrix and the QNMs eigenfrequencies for the relevant structures in the thesis. First, I discuss planar structures, followed by spheres.

Dielectric and layered planar structures

Planar structures are a two-port scattering problem as shown schematically in Figure 5.2a. Considering the incoming light, $\mathbf{E}_i$, with an angle, $k_x = k_0 \sin\theta$, where k_0 is the wave vector in vacuum. Then, the incoming and scattered fields can be described as,

$$\mathbf{E}_i\left(\mathbf{r}\right) = a_1 \mathbf{E} e^{\mathrm{i}k_z z + \mathrm{i}k_x x} + a_2 \mathbf{E} e^{-\mathrm{i}k_z z + \mathrm{i}k_x x} \tag{5.2}$$

$$\mathbf{E}_s\left(\mathbf{r}\right) = b_1 \mathbf{E} e^{-\mathrm{i}k_z z + \mathrm{i}k_x x} + b_2 \mathbf{E} e^{\mathrm{i}k_z z + \mathrm{i}k_x x} \tag{5.3}$$

From these equations, one can build the scattering matrix such that,

$$\begin{pmatrix} b_1 \\ b_2 \end{pmatrix} = \hat{S} \begin{pmatrix} a_1 \\ a_2 \end{pmatrix} , \tag{5.4}$$

Then, the scattering matrix is [74]:

$$\hat{S}(\omega) = \begin{pmatrix} R_{11}(\omega) & T_{12}(\omega) \\ R_{21}(\omega) & T_{22}(\omega) \end{pmatrix} , \tag{5.5}$$

Here, R_{ij}, T_{ij} represent the final reflection and transmission coefficients, respectively, from either side as shown in Figure 5.2. These coefficients can be calculated with the transfer matrix method (TMM) [84, 198]. The TMM breaks down a layered system, such as the one illustrated in Figure 5.2b, into matrices representing each layer. These matrices are multiplied together to calculate the optical response of the system. Textbooks such as [82, 84, 198] thoroughly explain this standard method.

In the case of a single slab in a symmetric environment as depicted in Figure 5.2a, reflection and transmission can be expressed as:

$$R_{\mathrm{TE,TM}} = \frac{r_{\mathrm{TE,TM}}(1 - e^{2\mathrm{i}k_{z,2}L})}{1 - r^2_{\mathrm{TE,TM}} e^{2\mathrm{i}k_{z,2}L}} , \quad T_{\mathrm{TE,TM}} = \frac{r_{\mathrm{TE,TM}}(1 - r^2) e^{2\mathrm{i}k_{z,2}L})}{1 - r^2_{\mathrm{TE,TM}} e^{2\mathrm{i}k_{z,2}L}} , \tag{5.6}$$

where the Fresnel coefficients are given by[80],

$$r_{\mathrm{TE}} = \frac{k_{z,1} - k_{z,2}}{k_{z,1} + k_{z,2}}, \quad r_{\mathrm{TM}} = \frac{k_{z,1} - k_{z,2}/\varepsilon(\omega)}{k_{z,1} + k_{z,2}/\varepsilon(\omega)} , \tag{5.7}$$

with $k_{z,1} = \sqrt{k_0^2 - k_x^2}$, $k_{z,2} = \sqrt{\varepsilon(\omega)k_0^2 - k_x^2}$ being the z-components of the wave vector in vacuum and dielectric, respectively.

In this simple case, it is unnecessary to calculate the full $\hat{S}$-matrix and find the poles of its eigenvalues. In this case, the eigenvalues are given by $\lambda_{1,2} = R \pm T$, and from equation (5.6), we see that the poles of the system are the

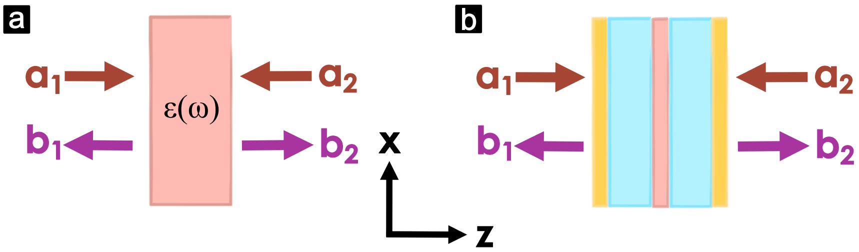

FIGURE 5.2: (a) Schematic of the two scattering channels in a single slab with permittivity $\varepsilon(\omega)$. (b) Schematic of the same scattering channels in a layered system where the total $\hat{S}$-matrix is calculated using the transfer matrix method (TMM).

roots of the characteristic equation:

$$1 - r_{\mathrm{TE,TM}}^{2} e^{2ik_{z,2}L} = 0\,. \tag{5.8}$$

This characteristic equation was used for all planar calculations in **Paper III**. However, in **Paper IV**, one channel was glass, and the other was air. Also, **Paper I** required several layers, as shown in Figure 5.2b. Therefore, the transmission and reflection coefficients were calculated using TMM to build the $\hat{S}$-matrix and calculate its eigenvalues numerically to find their poles and zeros.

Spheres

Paper III and **Paper VI** obtain the eigenfrequencies of a sphere as follows. When considering the scattering with a sphere of radius R, it is easier to consider plane waves in spherical coordinates (r, θ, ϕ). Mie theory writes the incident and scattered field in spherical coordinates. Here, we use the results and notation from Bohren [46]. The field scattered by a sphere of radius R and permittivity $\varepsilon = n^2$ can be written as an infinite series of spherical vector harmonics with scattering coefficients a_l and b_l [46].

$$a_l = \frac{n\psi_l(nx)\psi_l'(x) - \psi_l(x)\psi_l'(nx)}{n\psi_l(nx)\xi_l'(x) - \xi_l(x)\psi_l'(nx)}, \tag{5.9}$$

$$b_l = \frac{\psi_l(nx)\psi_l'(x) - n\psi_l(x)\psi_l'(nx)}{\psi_l(nx)\xi_l'(x) - n\xi_l(x)\psi_l'(nx)}, \tag{5.10}$$

where $x = k_0 R$. The Ricatti-Bessel functions: $\psi_l(\rho) = \rho j_l(\rho)$ and $\xi_l(\rho) = \rho h_l^{(1)}(\rho)$ are used to simplify the expressions with spherical Bessel, $j_l(\rho)$, and first kind Hankel functions, $h_l^{(1)}(\rho)$.

The coefficient a_l (b_l) weighs the contribution of the l-th TM (TE) mode, for which there is no radial magnetic (electric) field. Thus, the eigenfrequencies for TE and TM polarized modes with orbital number l are found as roots of the following characteristic equations:

$$\psi_l(nx)\xi_l'(x) - n\xi_l(x)\psi_l'(nx) = 0, \quad \text{(TE)} \tag{5.11}$$

$$n\psi_l(nx)\xi_l'(x) - \xi_l(x)\psi_l'(nx) = 0. \quad \text{(TM)} \tag{5.12}$$

These roots have several zeros at different energies. The radial number, N characterizes these higher-order modes.

Finally, as mentioned in section 2.3, the extinction cross-sections can be computed using the scattering coefficients as in equation (2.8).

5.2 Nanofabrication

This part is dedicated to the nanofabrication processes followed for conventional polaritons in metallic microcavities, plasmonic particles, self-assembled polaritons, self-hybridized MoS$_2$ and hBN slabs, and hBN disks.

All the samples were prepared on glass coverslips ($170\ \mu m$). Cleaned by 5 min ultrasonication in acetone and IPA, followed by oxygen plasma ashing.

5.2.1 Microcavities and plasmonic particles

The plasmon-microcavity polaritonic samples of **Paper I** were fabricated by evaporating a 30 nm Au bottom mirror on top of a 2 nm Cr adhesion layer using an e-beam evaporator (Kurt J. Lesker PVD225). Then 80 nm of SiO$_2$ was deposited by STS plasma-enhanced chemical vapor deposition (PECVD) at 300 °C.

Then, the nanodisks were fabricated by electron beam lithography (EBL) on spin-coated PMMA (baked for 5 min at 180 °C). Twelve arrays were patterned with disks of diameters $d = 60, 80$ and 100 nm and different pitches $\Lambda = 100, 140, 180, 220, 300$ and 340 nm. After the development and oxygen plasma ashing of the exposed areas, 20 nm of Au were evaporated. Then, lift-off in acetone finalizes the nanodisk arrays fabrication. The samples were annealed for 10 min at 200 °C on a hotplate to improve the crystallinity of the nanodisks. Separately, bare nanodisk arrays on glass were prepared similarly and imaged with SEM (Zeiss Supra 60 VP - EDX) by coating them with a thin layer of conductive polymer (E-spacer).

The second half of the spacer was spin-coated (PMMA, baked at 180 °C for 5 min). Finally, the cavity was closed by evaporating the last 30 nm Au layer deposited by e-beam evaporation.

In a similar way, the self-assembled cavities fabricated for **Paper II** that required a fixed bottom mirror were evaporated with various SiO_2 thicknesses deposited on top as described previously. Flakes of WSe_2 were deposited on top as explained below.

5.2.2 Transfer and characterization of 2D materials

MoS_2, WSe_2, and hBN flakes were mechanically exfoliated from bulk crystals (HQ Graphene) using dicing tape. The flakes were then transferred onto thin PDMS stamps and finally onto glass substrates, following the procedure outlined by Castellanos-Gomez et al. [199]. The monolayers were identified through their distinct photoluminescence [61] in an upright Nikon microscope with a fiber-coupled spectrometer (Andor Shamrock SR-303i) equipped with a CCD (Andor iDus 420).

Photographs of the transferred flakes were taken with a CCD camera (Nikon D300S) through an upright microscope. The number of layers was deduced by optical contrast using the software ImageJ. The thicknesses of hBN flakes were measured by a surface profiler (Tencor AS500). for **Paper IV**, the thicknesses of MoS_2 flakes were measured by AFM (NTEGRA Prima, NT-MDT) in non-contact mode by Dr. Battulga Munhkbat.

The hBN nanodisks were fabricated by Dr. Aleksandr Polyakov. The samples are spin-coated with a positive resist (polymethyl methacrylate, PMMA). Next, the electron beam in EBL was used to expose the area around the disks. After development, all PMMA was removed, except for the disks. These PMMA disks act as a protective layer for hBN during the reactive ion etching (RIE). This ensures that after RIE, only the protected areas have hBN remaining. Once the PMMA is dissolved, the hBN nanodisks are obtained. This method closely follows the one described in Munhkbat et al. [200]

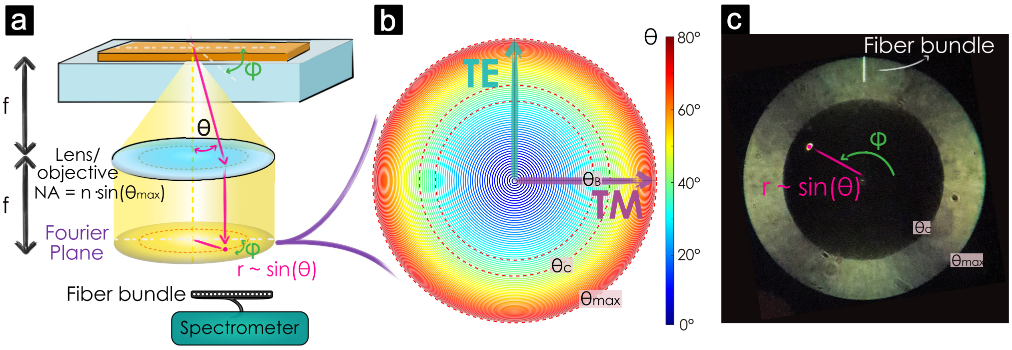

FIGURE 5.3: (a) Schematic of the experimental setup for angular resolved spectroscopy. Collimated light illuminates the full numerical aperture of the lens focused on the sample. The incoming light is focused with incident angles up to $\theta_{max} = \arcsin \mathrm{NA}/n$. The reflected signal is collected with the same lens. The Fourier plane of the lens is found at a distance equal to the focal length f. The spectra of the imaged Fourier plane are collected simultaneously at different radii via a fiber bundle with a spectrometer. (b) Incident angle distribution in the Fourier plane for an oil immersion objective with NA=1.49. The Brewster, θ_B, and critical, θ_C, angles are marked in red dashed lines. The arrows mark the directions along which TE and TM polarizations are measured. (c) Fourier plane of glass in reflection. All the light is transmitted before the critical angle and after it is all reflected. The fiber bundle is shown measuring TE-polarization. Figure modified from [41].

5.3 Optical characterization

My work heavily relies on reflectivity measurements to optically characterize micro and nanostructures at normal incidence and angular dispersion. This section describes the experimental setups used to measure reflection in the visible and infrared spectral range.

Reflection spectra at normal incidence were collected using a 20× objective (Nikon, NA = 0.45) in an upright microscope with a fiber-coupled spectrometer (Andor Shamrock SR-303i) equipped with a CCD (Andor iDus 420). The reflection signal was then normalized with a standard dielectric-coated silver mirror (Thorlabs). Higher angle reflection was measured in the Fourier plane as described below.

5.3.1 Fourier microscopy and spectroscopy

The field of Fourier optics is quite vast [198]. However, I mainly used it to obtain angular spectral information from the Fourier plane, also known as the Back Focal Plane (BFP). The BFP of a lens with focal length f is located at a distance f from it, as depicted in Figure 5.3a. The Fourier plane spreads the k-vector information, so light collected by the lens at various angles is distributed in the BFP at different radii, $r \sim sin(\theta)$ [201]. Increasing the angle increases the distance from the center. This means that light collected at normal incidence will land on the center of the Fourier plane, while the signal collected at the highest possible angle will end up on the edge of the Fourier plane.

In Figure 5.3b, we can see an example of angle dependence. The figure shows the angles corresponding to different radii in an oil immersion objective with a 1.49 numerical aperture (NA)[1]. The outermost dashed circle corresponds to the maximum angle collected by the objective. The most inner red dashed circle marks the Brewster angle, θ_B, for which all TM-polarized light is transmitted. This angle gives us the minimum reflection our setup can measure for TM polarization, which is about 1%.

The next marked dotted circle is the critical angle, θ_C, after which total internal reflection (TIR) occurs from the glass substrates. The critical angle is clearly visible in the Fourier plane of the glass substrate shown in Figure 5.3c. Before reaching this angle, most light is transmitted through the substrate, creating a black region. After the critical angle, the light is entirely reflected due to TIR, producing a bright band. This area is the region **II**, below the light line in **Paper IV**.

The Fourier plane is a powerful tool that also gives information about the polarization through the azimuthal angle, ϕ [202]. It is also possible to measure any polarization mixture, where the weight of each polarization depends on the azimuthal angle as $E_{\text{TM}} \sim cos(\phi)$ and $E_{\text{TE}} \sim sin(\phi)$ [202]. My experiments set the signal of TE (TM) polarization on the vertical (horizontal) axis, as shown in Figure 5.3b. The fiber bundle is placed to measure TE-polarization in the example in Figure 5.3c.

A simplified description of the optical setup in **Paper IV**, which used an inverted microscope (Nikon Eclipse TE2000-E), is depicted in Figure 5.4a. Here, a collimated laser-driven white light source (LDLS, EQ-99FC, high-brightness, flat-broadband spectrum) is polarized and fully covers the back aperture of an oil (n=1.51) immersion 60× objective (Nikon, NA=1.49). The sample is illuminated from the glass substrate, thus allowing it to reach TIR.

The same objective collects the reflected light (depicted in orange). Typically, the Fourier plane of an objective is located inside it, so a Bertrand lens is used to image it. The spectra are then collected for different radii

---

[1] Every lens or objective has a maximum angle from which it can collect light, and its numerical aperture describes it, NA= $n \sin \theta_{max}$, where n is the refractive index of the medium, which is usually air, water, or oil in commercial objectives.

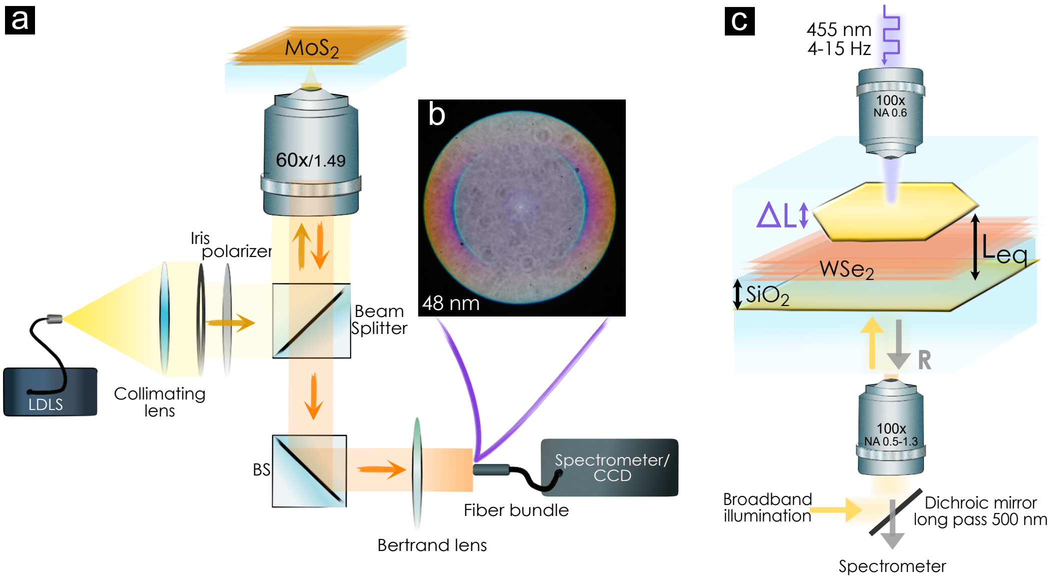
a
MoS$_2$
60x/1.49
Iris
polarizer
Beam
Splitter
LDLS
Collimating
lens
BS
Bertrand lens
Fiber bundle
Spectrometer/
CCD
b
48 nm
c
455 nm
4-15 Hz
100x
NA 0.6
ΔL
Leq
WSe$_2$
SiO$_2$
R
100x
NA 0.5-1.3
Broadband
illumination
Dichroic mirror
long pass 500 nm
Spectrometer

FIGURE 5.4: (a) Schematic of the experimental setup used to measure angular dispersion of conventional polaritons and self-hybridized MoS$_2$ polaritons. Collimated light is focused and reflected from the sample. It is collected with an objective whose Fourier plane is imaged with a Bertrand lens. Then, a fiber bundle coupled to a spectrometer measures spectra at various radii of the Fourier plane. Alternatively, the Fourier plane is imaged on a CCD camera. (b) True-color image of the Fourier plane of a 48 nm thick MoS$_2$ layer. (c) Experimental setup to measure normal incidence reflection from self-assembled polaritons while modulating the top mirror. The dimer is illuminated from the bottom with an LDLS source. The floating top mirror is modulated with incident laser irradiation from the top, causing a change in the distance between the mirrors, L_{eq}. The intensity of a continuous wave (cw) laser (455 nm) is modulated with a chopper, and the mirror returns to equilibrium when there is no laser irradiation. The dichroic mirror filters the laser. Figure modified from [41].

simultaneously using a fiber bundle consisting of 19 fibers with $100\ \mu m$ core (Andor SR-OPT-8002) coupled to a spectrometer (Andor 500i, equipped with Newton 920 CCD camera). Alternatively, the Fourier plane is imaged on a CCD camera (Nikon 300S), which produces true-color images of the Fourier plane, as illustrated in Figure 5.4b for a 48 nm MoS$_2$ slab.

The angular resolution can increase if the Fourier plane is expanded with a telescope (not shown). In this case, the fiber bundle no longer covers the full BFP as is the case in Figure 5.3c. The fiber bundle is mounted on an XYZ translational stage to ensure complete coverage.

For measurements above the light-line for the *conventional* polariton dispersion in **Paper I**, the setup is very similar to the one shown in Figure 5.4a. However, the objective and illumination source used are different. In this case, an air 40x objective with a numerical aperture of 0.95 was utilized, along with a fiber-coupled Halogen lamp (Thorlabs) to illuminate from the bottom.

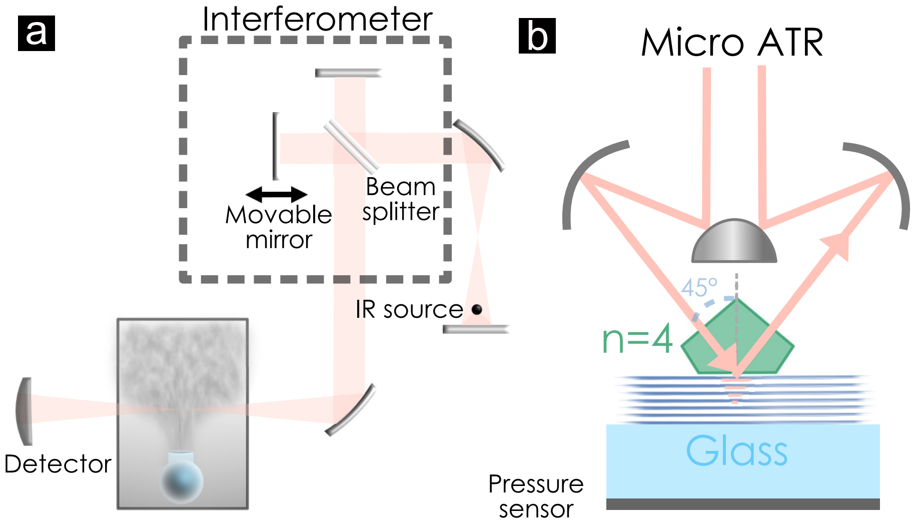

FIGURE 5.5: (a) Fourier transform infrared (FTIR) spectrometer schematic. The IR beam passes through the sample, and the transmitted light intensity is recorded. (b) Attenuated total reflection (ATR) objective working principle. Light is focused on the sample via a Germanium crystal, forming an evanescent wave that interacts with the sample. Figure modified from [43].

5.3.2 Active modulation of self-assembled cavities

All the measurements of reflection of **Paper II** took place in the inverted microscope (Nikon Eclipse TE2000-E), as depicted in Figure 5.4c. In this case, the objective was 100× oil immersion with a tunable NA 0.5-1.3 (Nikon). NA=0.5 was used for quasi-normal incidence reflection and to take colorful pictures of the formed cavities. The NA=1.3 was used for measuring the dispersion in reflection in the Fourier plane with the fiber bundle, as described in the previous section. The sample was illuminated using an LDLS. The reflected signal was then collected by a fiber-coupled spectrometer (Andor Shamrock SR-303i) equipped with an iDus 420 CCD detector.

Active modulation of the equilibrium distance between the fixed and floating mirror was obtained using a continuous wave (cw) laser (455 nm) modulated with a chopper. The radiation pressure pushes the top mirror towards the bottom mirror. The mirror returns to equilibrium when the laser intensity is minimal. A dichroic mirror filters the laser from the reflected signal measured by the spectrometer.

5.3.3 Fourier-Transform Infrared Spectroscopy

Fourier-transform infrared spectroscopy (FTIR) is a widely used technique to analyze the infrared absorption spectrum of materials. Conventional spectroscopic techniques separate light into colors and each color's intensity after interacting with the material. However, FTIR utilizes a Michelson interferometer to obtain dispersion in a broad energy range, as depicted in Figure 5.5a. In this method, the detector measures the intensity interferograms as a function of time, which uses a Fourier transformation to obtain the information in energy expressed in wave numbers.

The Bruker Vertex70v spectrometer was used in **Paper VI** to analyze the light absorbed by mist within the 600-8000 cm^{-1} range. Then, a vibrating mesh nebulizer generating the mist was placed in the optical path, as depicted in Figure 5.5a. Typically, a spectrometer measures bulk samples by shining a focused IR light beam through the sample.

To measure microscopic samples such as hBN flakes and hBN microdisks, we utilized the FTIR microscope Hyperion3000. With a 15× objective, the microscope can measure reflection and transmission at normal incidence. The samples were fabricated on glass due to its low refractive index in IR, which has a smaller impact on the optical resonances sustained by hBN. However, glass is not transparent in IR, so the samples were only measured in reflection.

The hBN slabs were measured beyond the light line using the Hyperion3000 in ATR mode. In this mode, a special objective is used to touch the sample with a crystal, as depicted in Figure 5.5b. The measurement starts when the pressure sensor detects 1N. The sample is illuminated at 45° using a germanium crystal with a refractive index of 4 in the IR range. Due to total internal reflection, only an evanescent wave interacts with the sample. The objective and detector then detect the reflected light. However, the smallest measurable spot size is approximately 32 μm, so it could not be used for hBN disks.

5.4 Optical levitation of water droplets

Paper V studied light scattering from a levitated water droplet in air. All experiments in **Paper V** were done by Javier Tello-Marmolejo. He built a

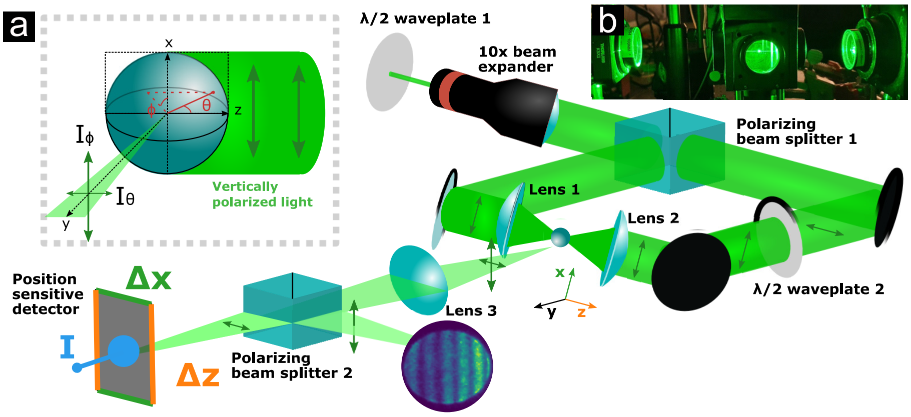
a
x
z
φ
θ
Iφ
Iθ
y
Vertically polarized light
λ/2 waveplate 1
10x beam expander
b
Polarizing beam splitter 1
Lens 1
Lens 2
λ/2 waveplate 2
x
y
z
Lens 3
Position sensitive detector
Δx
I
Δz
Polarizing beam splitter 2

FIGURE 5.6: (a) Counter-propagating trap used to measure Fano combs in levitated water droplets. The scattered light is measured at 90° from the axis of the trap. A beam splitter separates the vertical and horizontal polarizations. The vertical polarization is used to determine the size of the droplets, and the horizontal polarization is used to study the scattering intensity. The inset shows a picture of the light interacting with the sphere, resulting in the two scattered components. (b) Picture of the trap with a water droplet scattering light in the middle. Figure modified from [42].

counter-propagating optical trap to obtain stable trapping of water droplets produced by an ultrasonic nebulizer (MY-520A).

The 532 nm cw laser (Laser Quantum gem532) was divided into two arms. Both were focused into a beam waist of around the droplet size (~ 7.5 and $\sim 5\ \mu m$) from opposite sides. The relative power of each arm was balanced to minimize the drift of the particles during their evaporation.

The scattering was collected perpendicular to the trapping axis. A lens collected the signal, and a polarizing beam splitter separated it. The vertically polarized signal was used to visualize the diffraction pattern generated by the droplet from which its size can be calculated [203]. The horizontal one measures the intensity of the scattering while the droplet evaporates in time. The analysis of both signals results in the plot presented in Figure 2.11.

Chapter 6

Concluding remarks

Undertaking a PhD is a profoundly personal experience unique to every individual. While some journeys seem linear and focused on a specific subject, my experience has been different. I enjoy learning new things and connecting different subjects. Even though the heart of my research is on strong-light matter coupling, the systems I studied led to interesting results in other areas, such as Fano resonances, perfect absorption, and Casimir physics. In essence, this thesis reflects a journey full of fun and exciting detours.

The thesis divided the findings of some works for the sake of clarity. First, in **Chapter 2**, I introduced the optical properties of materials and optical resonators. This chapter included the results obtained outside of strong light-matter interaction, such as perfect absorption in MoS_2, Fano resonances in levitated water droplets, or the self-assembly of Fabry-Pérot resonators by equilibrium of electrostatic and Casimir forces. Then, **Chapter 3** delved into strong light-matter interactions in *conventional* structures, consisting of an external cavity and a separate resonant material. This chapter focused on polaritonic decay rates and tunable self-assembled polaritons that can be dynamically tuned. **Chapter 4** demonstrates that some materials can support optical modes and hybridize without an external cavity. This results in *self-hybridized cavity-free polaritons*, which can be more easily fabricated or naturally occur. This thesis explores cavity-free polaritons in various materials and geometries, including fabricated hBN nanodisks and naturally occurring planar 2D crystals and water droplets. Finally, **Chapter 5** gave an overview of all the methods (experimental and theoretical) used in this thesis.

In this final chapter, I summarize the works included in this thesis. Instead of dividing the results by topic, I present the scientific key takeaways of each work, along with my perspective on their scientific impact. As doctoral studies focus on our education toward becoming independent researchers, I also reflect on the learning outcomes of each work as a part of my growth as a researcher. With that in mind, let us dive into each work.

6.1 Summary of the appended papers

Paper I

Polaritonic linewidth asymmetry in the strong and ultrastrong coupling regime

In the first project, I worked on a conventional polariton given by a plasmon–microcavity system. We explored this platform in **Paper S.I** and noticed that the Rabi splitting increased with the nanoparticle density [31]. Therefore, we pushed the nanoparticle density limit in **Paper S.II** to reach ultrastrong coupling [33]. I was interested in the difference between both polaritons at higher coupling strengths for the follow-up. The lower polariton became narrower, while the upper polariton was broad. These observations were not unique in the polaritonic community. They were observed since the 90s [36] and were attributed to the disorder in the material [134]. However, for the theoretical analysis, we considered the nanodisks a dispersive media with a Lorentzian permittivity, removing all inhomogeneities from the system. Despite the absence of disorder, the linewidth asymmetry persisted.

Paper I analyzed the asymmetry behavior for various coupling strengths and noted that the lower polariton can even reach linewidths below the ones of the uncoupled elements for some coupling strengths. Interestingly, the decay rates equalize at higher detunings if no other losses affect the polaritons (as the interband transitions in the gold mirrors). I observed this also for cavity-free polaritons even before the coupling strength reached the ultrastrong coupling regime onset.

The most surprising result was that bulk polaritons also have a decay rate asymmetry, making the effect more general. Even more so, their quality factors are the same at zero detuning. Therefore, the linewidth asymmetry arises naturally from the Rabi splitting. The most intriguing result is that the polariton linewidths are equal for zero detuning with the renormalized frequency for bulk polaritons.

This project grew and developed alongside me. As my first project, I gained much experience in experimental and fabrication techniques through it. With time, I put a hold on the project as I delved into other exciting projects. Only when I learned the pole-search method could I apply it to this project and complete it. I finished the project only at the end of my studies, and the outcome was more profound than I ever expected.

Paper II

Tunable Self-Assembled Casimir Microcavities and Polaritons

Many discoveries are accidental, as was the case in **Paper II**. We were interested in continuing the work of **Paper S.II**. The question was if the ground state modification affected the formation of polaritons. In **Paper I**, the nanodisks sit on top of a spacer deposited on a bottom mirror, with a top mirror closing the cavity. Thus, as in most platforms, the structure is fixed. But what would happen if the top mirror could move? Would it sit on the nanodisks and form polaritons or try to avoid them? The hypothesis was that the floating mirror would leave the nanodisks because the polaritonic system has more energy than the uncoupled one. However, the denser the arrays, the more attracted the gold flakes (top mirror) were to the nanodisks. Later, we noticed that the attraction was because of Casimir forces. Even more so, we noticed that the floating gold flakes formed stable dimers with each other, creating Fabry-Pérot cavities resonating in the visible.

In **Paper II**, the two floating gold flakes formed a cavity by balancing the electrostatic repulsive and attractive Casimir forces. The concentration of ions in the solution affected the distance between the flakes in equilibrium. Therefore, the resonant wavelengths could be tuned by manipulating the ion concentration.

Paper II also showed that self-assembled cavities can strongly couple to the A-exciton in WSe_2 as a proof of concept. Coupling any material of interest resonating in the visible with these self-assembled cavities is possible. Moreover, the top mirror was movable in the liquid, allowing dynamic tunability. The floating mirror was pushed by laser radiation pressure to change the cavity thickness, which dynamically varied the coupling strength and polaritonic composition.

During this project, I gained insights into the importance of adaptability and creativity. I discovered that sometimes, the unexpected things we encounter can be just as interesting, or even more so, than what we were initially searching for. Additionally, I learned about the benefits of collaborative work. The allocation of tasks between the theoretical and experimental team members was precise, efficient, and fruitful.

Paper III

Abundance of Cavity-Free Polaritonic States in Resonant Materials and Nanostructures

Paper III brought back into focus bulk polaritons from a new perspective since we used the complex-frequency plane to visualize the complex eigenfrequencies of leaky systems. We described the coupling strength for these bulk polaritons in terms of the macroscopic permittivity. We showed that the bulk Rabi splitting is the limit for the Rabi splitting for any geometry, which significantly simplifies the search for materials that will achieve strong coupling. No other polaritons will be present if the material cannot sustain bulk polaritons.

Paper III theoretically demonstrated the possibility of achieving cavity-free polaritons in various geometries and materials. Our research involved organic semiconductor slabs, 2D crystals, perovskite nanowires, and water droplets. The key findings show that various geometries can support cavity-free polaritons, a minimum size exists for a cavity-free polaritonic structure, and the bulk Rabi splitting represents the maximum Rabi splitting achievable in any geometry. Cavity-free polaritons considerably reduce the fabrication complexity to obtain polaritonic systems.

This work also highlighted the importance of considering optical modes below and above the light line in 2D and 1D geometries. The modes below the light-line are often ignored, but they are crucial when determining the minimum size of a structure to be polaritonic. Note that cavity-free polaritons can complicate control experiments on polaritonic effects. Even after the external cavity is removed, polaritons may persist, making it difficult to compare the uncoupled and polaritonic effects. Sometimes, the material may still be strongly coupled "outside" of the cavity, and one should be cautious. To ensure that no remaining polaritons are present, the size of the structure must be below the critical size threshold.

Due to its implications, this theoretical work may be my most significant contribution to the polaritonic community. As it served as the backbone of my PhD, it was certainly the most relevant during my studies. It guided the rest of my research and established the theoretical basis I continued to rely on.

Paper IV

Perfect Absorption and Strong Coupling in Supported MoS_2 Multilayers

Continuing the theoretical work in **Paper III**, I conducted experiments to measure cavity-free polaritons in unpatterned MoS_2 slabs above and below the LL. The findings of **Paper IV** revealed the presence of polaritons and showed perfect absorption below the LL in unpatterned MoS_2 flakes.

Even a 2.6 nm thick unpatterned MoS_2 slab can perfectly absorb TE-polarized light. Moreover, the angle and frequency at which perfect absorption occurs largely depend on the number of layers present. As a result, each thickness below nine layers exhibits a unique reflection spectrum and provides an optical, non-invasive means of determining the number of layers without the need for comparison with a nearby monolayer.

Thicker slabs of MoS_2 have Fabry-Pérot modes that produce colored slabs when viewed at normal incidence. The most striking colors can be seen in the Fourier plane. These images, including this thesis's cover, are my favorite experimental results. Not only are they beautiful, but they also demonstrate two phenomena simultaneously: polaritons and perfect absorption. Both phenomena are present in the same unpatterned sample, making the results all the more remarkable.

This work was pivotal for my research education. It took me several months to achieve the quality of measurements I desired, but it boosted my confidence in the lab. Furthermore, with occasional guidance, I applied and expanded the theoretical skills I had developed in **Paper III**. I am very proud of this work and its scientific and aesthetic beauty. Its beauty lies in its simplicity.

Paper V

Fano Combs in the Directional Mie Scattering of a Water Droplet

Paper V studied Mie resonances of a single levitating water droplet. The spectrum of a levitated dielectric is now a classic since Ashkin observed it first in 1977 [91]. However, that spectrum is a mix of all resonances simultaneously occurring in the droplet. Mie calculations are needed to identify each resonance and untangle the messy spectrum.

Paper V presents an ordered spectrum with approximately a hundred resonances. These resonances progressively shift from Lorentzians to Fano profiles. The spectrum was obtained by measuring the scattering of a shrinking water droplet from a side. This method filtered the resonances and detected only TM modes. To explain the full spectrum, **Paper V** employed a quantum-mechanical analogy to an atom.

Collaborating with Javier Tello Marmolejo from Gothenburg University on **Paper V** was a very valuable experience. It all started with casual coffee breaks, where we would try to interpret Javier's experimental results. It was my first collaboration outside my research group, and it helped me grow and mature as a scientist.

Paper VI

Self-hybridized vibrational – Mie polaritons in water droplets

After the theoretical prediction in **Paper III**, I began working on measuring polaritonic water droplets. **Paper VI** shows a simple experiment using an FTIR and a commercial mesh nebulizer to produce mist. A fitting confirmed that the droplet sizes contributing to the measured optical density were indeed polaritonic. **Paper VI** presented how the optical density would look without interactions with the vibrational modes and the experimental results with heavy water. It demonstrated that the Mie modes strongly coupled with the vibrational modes.

The main message of this work was that water droplets in mist, fog, and clouds are naturally strongly coupled. As my most recent work, it is challenging to assess its impact. An interesting study will be to investigate whether the alterations observed in water (and its solutions) in conventional polaritons also manifest in water droplets.

During my time in the lab, I found this project to be the most enjoyable. It challenged me to think creatively and develop innovative ways to measure.

Additionally, it expanded my scientific knowledge and stimulated my curiosity.

6.2 Outlook

Some of my projects have raised more questions than answers, while others offer a new perspective by bridging two fields. In both cases, there are opportunities for further studies to deepen our knowledge. In this outlook, I will discuss a few topics that require more time for exploration and other ideas that could be pursued in the future.

Asymmetric polaritonic linewidths

Paper I showed, in an entirely classical approach, that the polariton linewidths are the same when zero detuning is considered with respect to the renormalized frequency. The renormalized frequency concept comes from studies of the USC regime in quantum optics, where the diamagnetic term of the Hamiltonian is crucial. Thus, the appearance of the renormalized frequency suggests the diamagnetic term's importance. However, the linewidth asymmetry occurred before the USC regime, implying that the diamagnetic term has a greater impact on linewidths than the actual eigenfrequencies. It would be interesting to investigate from a quantum optics perspective whether USC effects are present on linewidths even before the USC onset. In our joint project, Therese Karmstrand showed that the linewidth behavior is reproduced with a complete Hopfield Hamiltonian. This method provides us with the necessary means to investigate the effects of the diamagnetic term. The results need further work, but they are promising.

Furthermore, I intuitively expect the Hopfield coefficients to be equal at the same point as the linewidths become the same. Therese's calculations could establish a connection between the Hopfield coefficients and the linewidths obtained classically. This understanding could provide the composition of polaritons without the need for Hamiltonians.

However, the most interesting research direction would be the significance of the polaritons having equal linewidths at the renormalized frequency. An intriguing question is if it is possible to use the asymmetry in linewidths at zero detuning to detect changes in the ground-state energy.

On a more applied note, we demonstrated that coupling two high-loss elements, namely plasmonic nanodisks and metallic cavities, leads to a narrow resonance for the LP. This effect could benefit plasmonic sensors since the strong coupling generates a sharp lower polariton with nearly flat dispersion.

Casimir physics and polaritons

The work on Casimir has opened a lot of possibilities. We are currently exploring the control we can have on the self-assembled system. For example, we are patterning substrates to promote the formation of dimers in specific areas. We are also exploring possibilities to study the bending of thin gold flakes due to Casimir forces.

For the polaritonic community, the most interesting contribution of our work is to highlight the importance of Casimir physics. Casimir forces do not only form the self-assembled cavities. They contribute to the energy of the system, and this contribution is more important for metallic mirrors. The polaritonic community has largely ignored such contributions. The main difference between considering Casimir and strong coupling is that Casimir integrates over all frequencies, while strong coupling is a resonant effect focusing on frequencies around zero detuning. A study on the contribution of Casimir to the ground-state energy of the system would be interesting to see the impact of non-resonant effects on the system.

Cavity-free polaritons

We learned that cavity-free polaritons are more straightforward to obtain than we thought and are ubiquitous. From there, an option could be that polaritons are too common to be interesting. Thankfully, other works have recently shown that cavity-free polaritons also have interesting properties! For example, energy transport in organic semiconductors is faster in polaritonic nanowires [163], and the magneto-optical properties can be tuned by varying the photonic component in the polariton in a vdW magnet [191].

Even though I required more time to finish my research on polaritons in hBN nanodisks, we learned a lot during the project. More extensive arrays are needed to obtain better-quality results in FTIR, and simulations of the disks in reflection that consider the anisotropy of hBN are required to understand the experimental results better. However, our primary goal with that project was to observe Raman signal dependence on the polaritonic states. However, we did not see any changes. We now realize that to observe any variations, we need to switch to a non-centrosymmetric material. Therefore, I look forward to seeing the experiment results using a different material platform.

Water polaritons

A clear next step for my work on polaritonic water droplets is to try to measure the Rabi splitting between a single Mie mode and the stretching modes in water. I envision a setup like the one presented in **Paper V**. However, that setup has challenges to overcome to achieve it. Notably, it requires equipment in the IR, including detectors and tunable lasers. Once the appropriate source is found, the next problem is evaporation. In **Paper V**, every droplet evaporates in about 10 seconds, and water is transparent at the laser wavelength (532 nm). That process considerably speeds up if the droplet absorbs at the frequency of the illuminating IR source (around 3μm), requiring a fast photodetector sensible in the IR.

However challenging and interesting, these experiments would still only measure Rabi splitting. The most exciting research would be to go beyond simply observing Rabi splitting. It would be interesting to know if any properties are affected by the polaritons in the water droplets. Are thermal properties affected? Could chemical reaction rates be changed? In a long shot, polaritons could affect the process of acid rain formation, which occurs by interactions between water droplets and atmospheric gases. Research in this direction would have the highest impact.

As human beings, our memory capacity is limited. So, if you can only remember one thing from this thesis, remember that polaritons are more common than previously thought. They can exist in simpler structures and even occur naturally, such as in water droplets in clouds. There is still much work left to understand polaritons fully, and I am excited to see how the field evolves in the coming years.

Bibliography

1. Peters, V. N., Prayakarao, S., Koutsares, S. R., Bonner, C. E. & Noginov, M. A. Control of Physical and Chemical Processes with Nonlocal Metal–Dielectric Environments. *ACS Photonics* **6,** 3039–3056 (2019).
2. Munkhbat, B., Wersäll, M., Baranov, D. G., Antosiewicz, T. J. & Shegai, T. Suppression of photo-oxidation of organic chromophores by strong coupling to plasmonic nanoantennas. *Science Advances* **4,** eaas9552. ISSN: 2375-2548 (2018).
3. Hutchison, J. A., Schwartz, T., Genet, C., Devaux, E. & Ebbesen, T. W. Modifying chemical landscapes by coupling to vacuum fields. *Angewandte Chemie International Edition* **51,** 1592–1596 (2012).
4. Ebbesen, T. W. Hybrid light–matter states in a molecular and material science perspective. *Accounts of Chemical Research* **49,** 2403–2412 (2016).
5. Feist, J., Galego, J. & Garcia-Vidal, F. J. Polaritonic chemistry with organic molecules. *ACS Photonics* **5,** 205–216 (2018).
6. Bhatt, P., Kaur, K. & George, J. Enhanced Charge Transport in Two-Dimensional Materials through Light–Matter Strong Coupling. *ACS Nano* (2021).
7. Coles, D. M. *et al.* Polariton-mediated energy transfer between organic dyes in a strongly coupled optical microcavity. *Nature Materials* **13,** 712–719 (2014).
8. Garcia-Vidal, F. J., Ciuti, C. & Ebbesen, T. W. Manipulating matter by strong coupling to vacuum fields. *Science* **373** (2021).
9. Törmä, P. & Barnes, W. L. Strong coupling between surface plasmon polaritons and emitters: a review. *Reports on Progress in Physics* **78,** 013901 (2014).
10. Hakala, T. K. *et al.* Bose–Einstein condensation in a plasmonic lattice. *Nature Physics* **14,** 739–744 (2018).
11. Anton-Solanas, C. *et al.* Bosonic condensation of exciton–polaritons in an atomically thin crystal. *Nature Materials,* 1–7 (2021).

12. Deng, H., Weihs, G., Santori, C., Bloch, J. & Yamamoto, Y. Condensation of semiconductor microcavity exciton polaritons. *Science* **298,** 199–202 (2002).
13. Kaluzny, Y., Goy, P., Gross, M., Raimond, J. M. & Haroche, S. Observation of Self-Induced Rabi Oscillations in Two-Level Atoms Excited Inside a Resonant Cavity: The Ringing Regime of Superradiance. *Physical Review Letters* **51,** 1175–1178 (1983).
14. Haroche, S. Nobel Lecture: Controlling photons in a box and exploring the quantum to classical boundary. *Reviews of Modern Physics* **85,** 1083 (2013).
15. Hopfield, J. Theory of the contribution of excitons to the complex dielectric constant of crystals. *Physical Review* **112,** 1555 (1958).
16. Mills, D. & Burstein, E. Polaritons: the electromagnetic modes of media. *Reports on Progress in Physics* **37,** 817 (1974).
17. Weisbuch, C., Nishioka, M., Ishikawa, A & Arakawa, Y. Observation of the coupled exciton-photon mode splitting in a semiconductor quantum microcavity. *Physical Review Letters* **69,** 3314 (1992).
18. Skolnick, M., Fisher, T. & Whittaker, D. Strong coupling phenomena in quantum microcavity structures. *Semiconductor Science and Technology* **13,** 645 (1998).
19. Ciuti, C., Bastard, G. & Carusotto, I. Quantum vacuum properties of the intersubband cavity polariton field. *Physical Review B* **72,** 115303 (2005).
20. Lidzey, D. G. *et al.* Strong exciton–photon coupling in an organic semiconductor microcavity. *Nature* **395,** 53–55 (1998).
21. Yoshie, T. *et al.* Vacuum Rabi splitting with a single quantum dot in a photonic crystal nanocavity. *Nature* **432,** 200–203 (2004).
22. Reithmaier, J. P. *et al.* Strong coupling in a single quantum dot–semiconductor microcavity system. *Nature* **432,** 197–200 (2004).
23. Łempicka-Mirek, K. *et al.* Electrically tunable Berry curvature and strong light-matter coupling in liquid crystal microcavities with 2D perovskite. *Science Advances* **8,** eabq7533 (2022).
24. Liu, X. *et al.* Strong Light–matter Coupling in Two-Dimensional Atomic Crystals. *Nature Photonics* (2014).
25. Hobson, P. A. *et al.* Strong exciton–photon coupling in a low-Q all-metal mirror microcavity. *Applied Physics Letters* **81,** 3519–3521 (2002).

26. Bellessa, J, Bonnand, C, Plenet, J. & Mugnier, J. Strong coupling between surface plasmons and excitons in an organic semiconductor. *Physical Review Letters* **93,** 036404 (2004).
27. Chikkaraddy, R. *et al.* Single-molecule strong coupling at room temperature in plasmonic nanocavities. *Nature* **535,** 127–130 (2016).
28. Zengin, G. *et al.* Realizing Strong Light-Matter Interactions between Single-Nanoparticle Plasmons and Molecular Excitons at Ambient Conditions. *Physical Review Letters* **114,** 157401 (2015).
29. Liu, W. *et al.* Strong exciton–plasmon coupling in MoS_2 coupled with plasmonic lattice. *Nano Letters* **16,** 1262–1269 (2016).
30. Ameling, R. & Giessen, H. Cavity plasmonics: large normal mode splitting of electric and magnetic particle plasmons induced by a photonic microcavity. *Nano Letters* **10,** 4394–4398 (2010).
31. Bisht, A. *et al.* Collective strong light-matter coupling in hierarchical microcavity-plasmon-exciton systems. *Nano letters* **19,** 189–196 (2018).
32. Agarwal, G. Vacuum-field Rabi splittings in microwave absorption by Rydberg atoms in a cavity. *Physical Review Letters* **53,** 1732 (1984).
33. Baranov, D. G. *et al.* Ultrastrong coupling between nanoparticle plasmons and cavity photons at ambient conditions. *Nature Communications* **11,** 2715 (2020).
34. Mueller, N. S. *et al.* Deep strong light–matter coupling in plasmonic nanoparticle crystals. *Nature* **583,** 780–784 (2020).
35. Frisk Kockum, A., Miranowicz, A., De Liberato, S., Savasta, S. & Nori, F. Ultrastrong coupling between light and matter. *Nature Reviews Physics* **1,** 19–40 (2019).
36. Whittaker, D. M. *et al.* Motional Narrowing in Semiconductor Microcavities. *Physical Review Letters* **77,** 4792–4795 (1996).
37. Whittaker, D. M. What Determines Inhomogeneous Linewidths in Semiconductor Microcavities? *Physical Review Letters* **80,** 4791–4794 (1998).
38. Canales, A., Karmstrand, T., Baranov, D. G., Antosiewicz, T. J. & Shegai, T. O. Polaritonic linewidth asymmetry in the strong and ultrastrong coupling regime. *Nanophotonics* **12,** 4073–4086 (2023).
39. Munkhbat, B., Canales, A., Küçüköz, B., Baranov, D. G. & Shegai, T. O. Tunable Self-Assembled Casimir Microcavities and Polaritons. *Nature* **597,** 214–219 (2021).

40. Canales, A., Baranov, D. G., Antosiewicz, T. J. & Shegai, T. Abundance of cavity-free polaritonic states in resonant materials and nanostructures. *The Journal of Chemical Physics* **154,** 024701 (2021).
41. Canales, A., Kotov, O. & Shegai, T. O. Perfect Absorption and Strong Coupling in Supported $\mathrm{MoS_2}$ Multilayers. *ACS Nano* **17,** 3401–3411 (2023).
42. Marmolejo, J. T., Canales, A., Hanstorp, D. & Méndez-Fragoso, R. Fano Combs in the Directional Mie Scattering of a Water Droplet. *Physical Review Letters* **130,** 043804 (2023).
43. Canales, A., Kotov, O. V., Küçüköz, B. & Shegai, T. O. Self-hybridized vibrational-Mie polaritons in water droplets. *arXiv preprint arXiv:2309.06906* (2023).
44. Fox, M. *Optical properties of solids* (American Association of Physics Teachers, 2002).
45. Collins, R. W. & Ferlauto, A. S. Optical physics of materials. *ChemInform* **37** (2006).
46. *Absorption and scattering of light by small particles* 530. ISBN: 3527618163 (Wiley, 2004).
47. Würthner, F., Kaiser, T. E. & Saha-Möller, C. R. J-aggregates: from serendipitous discovery to supramolecular engineering of functional dye materials. *Angewandte Chemie International Edition* **50,** 3376–3410 (2011).
48. Balasubrahmaniyam, M., Genet, C. & Schwartz, T. Coupling and decoupling of polaritonic states in multimode cavities. *Physical Review B* **103,** L241407 (2021).
49. Lidzey, D. G. *et al.* Room Temperature Polariton Emission from Strongly Coupled Organic Semiconductor Microcavities. *Physical Review Letters* **82,** 3316–3319 (1999).
50. Guebrou, S. A. *et al.* Coherent emission from a disordered organic semiconductor induced by strong coupling with surface plasmons. *Physical review letters* **108,** 066401 (2012).
51. Hale, G. M. & Querry, M. R. Optical Constants of Water in the 200-nm to 200-μm Wavelength Region. *Appl. Opt.* **12,** 555–563 (1973).
52. Segelstein, D. J. *The complex refractive index of water* PhD thesis (University of Missouri–Kansas City, 1981).
53. Fiedler, J. *et al.* Full-Spectrum High-Resolution Modeling of the Dielectric Function of Water. *The Journal of Physical Chemistry B* (2020).

54. Li, Y. *et al.* Measurement of the optical dielectric function of monolayer transition-metal dichalcogenides: MoS_2, $MoSe_2$, WS_2, and WSe_2. *Physical Review B* **90,** 205422 (2014).
55. Manzeli, S., Ovchinnikov, D., Pasquier, D., Yazyev, O. V. & Kis, A. 2D transition metal dichalcogenides. *Nature Reviews Materials* **2,** 1–15 (2017).
56. Novoselov, K. S. *et al.* Two-dimensional atomic crystals. *Proceedings of the National Academy of Sciences* **102,** 10451–10453 (2005).
57. Geim, A. K. & Grigorieva, I. V. Van der Waals heterostructures. *Nature* **499,** 419–425 (2013).
58. Ermolaev, G. A. *et al.* Giant optical anisotropy in transition metal dichalcogenides for next-generation photonics. *Nature Communications* **12** (2021).
59. Van Baren, J. *et al.* Stacking-dependent interlayer phonons in 3R and 2H MoS_2. *2D Materials* **6,** 025022 (2019).
60. Munkhbat, B., Wróbel, P., Antosiewicz, T. J. & Shegai, T. O. Optical constants of several multilayer transition metal dichalcogenides measured by spectroscopic ellipsometry in the 300–1700 nm range: high index, anisotropy, and hyperbolicity. *ACS Photonics* **9,** 2398–2407 (2022).
61. Splendiani, A. *et al.* Emerging photoluminescence in monolayer MoS_2. *Nano Letters* **10,** 1271–1275 (2010).
62. Johnson, P. B. & Christy, R.-W. Optical constants of the noble metals. *Physical Review B* **6,** 4370 (1972).
63. Caldwell, J. D. *et al.* Photonics with hexagonal boron nitride. *Nature Reviews Materials* **4,** 552–567 (2019).
64. Caldwell, J. D. *et al.* Low-loss, infrared and terahertz nanophotonics using surface phonon polaritons. *Nanophotonics* **4,** 44–68. ISSN: 21928606 (2015).
65. Maier, S. A. *Plasmonics: fundamentals and applications* (Springer Science & Business Media, 2007).
66. Kats, M. A. & Capasso, F. Optical Absorbers Based on Strong Interference in Ultra-Thin Films. *Laser Photonics Rev.* **10,** 735–749. ISSN: 18638899 (2016).
67. Song, H. *et al.* Nanocavity absorption enhancement for two-dimensional material monolayer systems. *Optics express* **23,** 7120–7130 (2015).

68. Baranov, D., Edgar, J. H., Hoffman, T., Bassim, N. & Caldwell, J. D. Perfect interferenceless absorption at infrared frequencies by a van der Waals crystal. *Physical Review B* **92,** 201405 (2015).
69. Horng, J. *et al.* Perfect Absorption By An Atomically Thin Crystal. *Physical Review Applied* **14,** 1–9 (2020).
70. Cao, J. *et al.* Perfect Light Absorption of Monolayer MoS_2 with Cross-Shaped Groove Air Resonator. *Mater. Res. Express* **6,** 015050 (2018).
71. Liu, J.-T., Wang, T.-B., Li, X.-J. & Liu, N.-H. Enhanced Absorption of Monolayer MoS_2 with Resonant Back Reflector. *Journal of Applied Physics* **115,** 193511 (2014).
72. Hägglund, C., Apell, S. P. & Kasemo, B. Maximized Optical Absorption in Ultrathin Films and Its Application to Plasmon-Based Two-Dimensional Photovoltaics. *Nano Lett.* **10,** 3135–3141 (2010).
73. Baranov, D. G., Krasnok, A., Shegai, T., Alù, A. & Chong, Y. Coherent perfect absorbers: linear control of light with light. *Nature Reviews Materials* **2,** 1–14 (2017).
74. Krasnok, A. *et al.* Anomalies in Light Scattering. *Adv. Opt. Photonics* **11,** 892–951 (2019).
75. Berkhout, A. & Koenderink, A. F. Perfect Absorption and Phase Singularities in Plasmon Antenna Array Etalons. *ACS Photonics* **6,** 2917–2925 (2019).
76. Vahala, K. J. Optical microcavities. *Nature* **424,** 839–846 (2003).
77. Heylman, K. D. *et al.* Optical microresonators for sensing and transduction: a materials perspective. *Advanced Materials* **29,** 1700037 (2017).
78. Lalanne, P., Yan, W., Vynck, K., Sauvan, C. & Hugonin, J.-P. Light interaction with photonic and plasmonic resonances. *Laser & Photonics Reviews* **12,** 1700113 (2018).
79. Kristensen, P. T., Herrmann, K., Intravaia, F. & Busch, K. Modeling electromagnetic resonators using quasinormal modes. *Advances in Optics and Photonics* **12,** 612–708 (2020).
80. Jackson, J. D. *Classical Electrodynamics* 3rd (John Wiley and Sons, Inc., New York, 1999).
81. Perot, A. & Fabry, C. On the application of interference phenomena to the solution of various problems of spectroscopy and metrology. *Astrophysical Journal, vol. 9, p. 87* **9,** 87 (1899).
82. Saleh, B. E. & Teich, M. C. *Fundamentals of photonics* (John Wiley & sons, 2019).

83. Novotny, L. & Hecht, B. *Principles of nano-optics* (Cambridge University Press, 2012).
84. Born, M. & Wolf, E. *Principles of optics: electromagnetic theory of propagation, interference and diffraction of light* (Elsevier, 2013).
85. Barnes, W. L., Dereux, A. & Ebbesen, T. W. Surface plasmon subwavelength optics. *Nature* **424,** 824–830 (2003).
86. Mills, D. L. & Burstein, E. Polaritons: The electromagnetic modes of media. *Reports on Progress in Physics* **37,** 817–926 (1974).
87. `https://www.ansys.com/products/photonics`. Accessed: 2023-05-31.
88. Kravets, V. G., Kabashin, A. V., Barnes, W. L. & Grigorenko, A. N. Plasmonic surface lattice resonances: a review of properties and applications. *Chem. Rev.* **118,** 5912–5951 (2018).
89. Ameling, R. & Giessen, H. Microcavity plasmonics: strong coupling of photonic cavities and plasmons. *Laser Photonics Reviews* **7,** 141–169 (2013).
90. Ward, A. D., Zhang, M. & Hunt, O. Broadband Mie scattering from optically levitated aerosol droplets using a white LED. *Optics Express* **16,** 16390–16403 (2008).
91. Ashkin, A. & Dziedzic, J. M. Observation of Resonances in the Radiation Pressure on Dielectric Spheres. *Physical Review Letters* **38,** 1351–1354 (1977).
92. Chýlek, P., Kiehl, J. T. & Ko, M. K. W. Optical levitation and partial-wave resonances. *Phys. Rev. A* **18,** 2229–2233 (1978).
93. Fano, U. Effects of Configuration Interaction on Intensities and Phase Shifts. *Phys. Rev.* **124,** 1866–1878 (1961).
94. Limonov, M. F., Rybin, M. V., Poddubny, A. N. & Kivshar, Y. S. Fano resonances in photonics. *Nature Photonics* **11,** 543–554 (2017).
95. Rybin, M. V. *et al.* Mie scattering as a cascade of Fano resonances. *Optics Express* **21,** 30107–30113 (2013).
96. Tribelsky, M. I., Geffrin, J.-M., Litman, A., Eyraud, C. & Moreno, F. Directional Fano resonances in light scattering by a high refractive index dielectric sphere. *Physical Review B* **94,** 121110 (2016).
97. Johnson, B. R. Theory of morphology-dependent resonances: shape resonances and width formulas. *Journal of the Optical Society of America* **10** (1993).

98. Chen, S. *et al.* Rapid seedless synthesis of gold nanoplates with microscaled edge length in a high yield and their application in SERS. *Nano-micro Letters* **8,** 328–335 (2016).
99. Israelachvili, J. N. *Intermolecular and surface forces* (Academic press, 2011).
100. Casimir, H. B. G. & Polder, D. The Influence of Retardation on the London-van der Waals Forces. *Physical Review* **73,** 360–372 (1948).
101. Casimir, H. B. *On the attraction between two perfectly conducting plates* in *Proc. Kon. Ned. Akad. Wet.* **51** (1948), 793.
102. Lifshitz, E. & Hamermesh, M. in *Perspectives in Theoretical Physics* (ed Pitaevski, L.) 329–349 (Pergamon, Amsterdam, 1992). ISBN: 978-0-08-036364-6.
103. Dzyaloshinskii, I., Lifshitz, E. & Pitaevskii, L. The general theory of van der Waals forces. *Advances in Physics* **10,** 165–209 (1961).
104. Fano, U. Atomic Theory of Electromagnetic Interactions in Dense Materials. *Physical Review* **103,** 1202–1218 (1956).
105. Huang, K. On the interaction between the radiation field and ionic crystals. *Proceedings of the Royal Society of London. Series A. Mathematical and Physical Sciences* **208,** 352–365 (1951).
106. Gordon, J. P., Zeiger, H. J. & Townes, C. H. The maser—new type of microwave amplifier, frequency standard, and spectrometer. *Physical Review* **99,** 1264 (1955).
107. Jaynes, E. T. & Cummings, F. W. Comparison of quantum and semiclassical radiation theories with application to the beam maser. *Proceedings of the IEEE* **51,** 89–109 (1963).
108. Liu, X. *et al.* Strong light–matter coupling in two-dimensional atomic crystals. *Nature Photonics* **9,** 30–34 (2015).
109. Khitrova, G., Gibbs, H., Kira, M, Koch, S. W. & Scherer, A. Vacuum Rabi splitting in semiconductors. *Nature Physics* **2,** 81–90 (2006).
110. Zhang, S. *et al.* Strong Exciton–Photon Coupling in Hybrid Inorganic–Organic Perovskite Micro/Nanowires. *Advanced Optical Materials* **6,** 1701032 (2018).
111. Baranov, D. G., Wersäll, M., Cuadra, J., Antosiewicz, T. J. & Shegai, T. Novel Nanostructures and Materials for Strong Light–Matter Interactions. *ACS Photonics* **5,** 24–42 (2018).
112. Gerry, C., Knight, P. & Knight, P. L. *Introductory quantum optics* (Cambridge University Press, 2005).

113. Le Boité, A. Theoretical methods for ultrastrong light–matter interactions. *Advanced Quantum Technologies* **3,** 1900140 (2020).
114. Miri, M.-A. & Alu, A. Exceptional points in optics and photonics. *Science* **363,** eaar7709 (2019).
115. Purcell, E. M., Torrey, H. C. & Pound, R. V. Resonance absorption by nuclear magnetic moments in a solid. *Physical Review* **69,** 37 (1946).
116. Bhuyan, R. *et al.* The Rise and Current Status of Polaritonic Photochemistry and Photophysics. *Chemical Reviews* (2023).
117. Rider, M. & Barnes, W. Something from nothing: linking molecules with virtual light. *Contemporary Physics* **62,** 217–232 (2021).
118. Laussy, F. P., del Valle, E. & Tejedor, C. Luminescence spectra of quantum dots in microcavities. I. Bosons. *Physical Review B* **79,** 235325 (2009).
119. Thompson, R. J., Rempe, G. & Kimble, H. J. Observation of normal-mode splitting for an atom in an optical cavity. *Physical Review Letters* **68,** 1132–1135 (1992).
120. Rodriguez, S. R.-K. Classical and quantum distinctions between weak and strong coupling. *European Journal of Physics* **37,** 025802 (2016).
121. Tserkezis, C. *et al.* On the applicability of quantum-optical concepts in strong-coupling nanophotonics. *Reports on Progress in Physics* **83,** 082401 (2020).
122. Fregoni, J., Garcia-Vidal, F. J. & Feist, J. Theoretical challenges in polaritonic chemistry. *ACS Photonics* **9,** 1096–1107 (2022).
123. Canales Ramos, A. I. *Light-Interband transitions coupling in Aluminum* Available at `https://odr.chalmers.se/items/0d271177-579e-49ff-b489-64f1936f37d8`. Master's thesis (Chalmers University of Technology, 2018).
124. Di Stefano, O. *et al.* Resolution of gauge ambiguities in ultrastrong-coupling cavity quantum electrodynamics. *Nature Physics* **15,** 803–808 (2019).
125. Vasanelli, A., Todorov, Y. & Sirtori, C. Ultra-strong light–matter coupling and superradiance using dense electron gases. *Comptes Rendus Physique* **17,** 861–873 (2016).
126. Cortese, E. & De Liberato, S. Exact solution of polaritonic systems with arbitrary light and matter frequency-dependent losses. *The Journal of Chemical Physics* **156** (2022).

127. Jouy, P. *et al.* Transition from strong to ultrastrong coupling regime in mid-infrared metal-dielectric-metal cavities. *Applied Physics Letters* **98,** 231114 (2011).
128. Barra-Burillo, M. *et al.* Microcavity phonon polaritons from the weak to the ultrastrong phonon–photon coupling regime. *Nature Communications* **12,** 6206 (2021).
129. Gao, W., Li, X., Bamba, M. & Kono, J. Continuous transition between weak and ultrastrong coupling through exceptional points in carbon nanotube microcavity exciton–polaritons. *Nature Photonics* **12,** 362–367 (2018).
130. Berkhout, A. & Koenderink, A. F. A simple transfer-matrix model for metasurface multilayer systems. *Nanophotonics* **9,** 3985–4007 (2020).
131. Zhu, Y. *et al.* Vacuum Rabi splitting as a feature of linear-dispersion theory: Analysis and experimental observations. *Physical Review Letters* **64,** 2499–2502 (1990).
132. Munkhbat, B. *et al.* Self-Hybridized Exciton-Polaritons in Multilayers of Transition Metal Dichalcogenides for Efficient Light Absorption. *ACS Photonics* **6,** 139–147 (2019).
133. Raizen, M. G., Thompson, R. J., Brecha, R. J., Kimble, H. J. & Carmichael, H. J. Normal-mode splitting and linewidth averaging for two-state atoms in an optical cavity. *Physical Review Letters* **63,** 240 (1989).
134. Ell, C. *et al.* Influence of Structural Disorder and Light Coupling on the Excitonic Response of Semiconductor Microcavities. *Physical Review Letters* **80,** 4795–4798 (1998).
135. Savona, V., Piermarocchi, C., Quattropani, A., Tassone, F. & Schwendimann, P. Microscopic Theory of Motional Narrowing of Microcavity Polaritons in a Disordered Potential. *Physical Review Letters* **78,** 4470–4473 (1997).
136. Litinskaia, M., La Rocca, G. & Agranovich, V. Inhomogeneous broadening of polaritons in high-quality microcavities and weak localization. *Physical Review B* **64,** 165316 (2001).
137. Kavokin, A. V. & Baumberg, J. J. Exciton-light coupling in quantum wells: From motional narrowing to superradiance. *Physical Review B* **57,** R12697–R12700 (1998).
138. Kavokin, A. V. Motional narrowing of inhomogeneously broadened excitons in a semiconductor microcavity: Semiclassical treatment. *Phys. Rev. B* **57,** 3757–3760 (1998).

139. Wang, W. *et al.* Interplay between strong coupling and radiative damping of excitons and surface plasmon polaritons in hybrid nanostructures. *ACS Nano* **8,** 1056–1064 (2014).
140. Hao, F. *et al.* Symmetry breaking in plasmonic nanocavities: subradiant LSPR sensing and a tunable Fano resonance. *Nano Letters* **8,** 3983–3988 (2008).
141. Verellen, N. *et al.* Fano resonances in individual coherent plasmonic nanocavities. *Nano Letters* **9,** 1663–1667 (2009).
142. Hopfield, J. Resonant scattering of polaritons as composite particles. *Physical Review* **182,** 945 (1969).
143. Henry, C. & Hopfield, J. Raman scattering by polaritons. *Physical Review Letters* **15,** 964 (1965).
144. Huttner, B. & Barnett, S. M. Quantization of the electromagnetic field in dielectrics. *Physical Review A* **46,** 4306–4322. ISSN: 10502947 (1992).
145. De Liberato, S. Virtual photons in the ground state of a dissipative system. *Nature Communications* **8,** 1465 (2017).
146. Król, M *et al.* Universality of open microcavities for strong light-matter coupling. *Optical Materials Express* **13,** 2651–2661 (2023).
147. Thomas, P. A., Menghrajani, K. S. & Barnes, W. L. All-optical control of phase singularities using strong light-matter coupling. *Nature Communications* **13,** 1809 (2022).
148. Munkhbat, B. *et al.* Electrical control of hybrid monolayer tungsten disulfide–plasmonic nanoantenna light–matter states at cryogenic and room temperatures. *ACS Nano* **14,** 1196–1206 (2020).
149. Ellenbogen, T., Steinvurzel, P. & Crozier, K. B. Strong coupling between excitons in J-aggregates and waveguide modes in thin polymer films. *Applied Physics Letters* **98** (2011).
150. Fei, Z. *et al.* Nano-optical imaging of $\mathrm{WSe_2}$ waveguide modes revealing light-exciton interactions. *Physical Review B* **94,** 081402 (2016).
151. Hu, F *et al.* Imaging propagative exciton polaritons in atomically thin $\mathrm{WSe_2}$ waveguides. *Physical Review B* **100,** 121301 (2019).
152. Kaeek, M., Damari, R., Roth, M., Fleischer, S. & Schwartz, T. Strong Coupling in a Self-Coupled Terahertz Photonic Crystal. *ACS Photonics* (2021).
153. Thomas, P. A., Menghrajani, K. S. & Barnes, W. L. Cavity-Free Ultrastrong Light-Matter Coupling. *The Journal of Physical Chemistry Letters* **12,** 6914–6918 (2021).

154. Wang, Q. *et al.* Direct observation of strong light-exciton coupling in thin WS_2 flakes. *Optics Express* **24,** 7151–7157 (2016).
155. Gogna, R., Zhang, L. & Deng, H. Self-Hybridized, Polarized Polaritons in ReS_2 Crystals. *ACS Photonics* **7,** 3328–3332 (2020).
156. Savona, V., Andreani, L., Schwendimann, P. & Quattropani, A. Quantum well excitons in semiconductor microcavities: Unified treatment of weak and strong coupling regimes. *Solid State Communications* **93,** 733–739 (1995).
157. Antosiewicz, T. J., Apell, S. P. & Shegai, T. Plasmon–exciton interactions in a core–shell geometry: from enhanced absorption to strong coupling. *ACS Photonics* **1,** 454–463 (2014).
158. Zanotto, S. in *Fano Resonances in Optics and Microwaves: Physics and Applications* (eds Kamenetskii, E., Sadreev, A. & Miroshnichenko, A.) 551–570 (Springer International Publishing, Cham, Switzerland, 2018).
159. Low, T. *et al.* Polaritons in layered two-dimensional materials. *Nature Materials* **16,** 182–194 (2017).
160. Evans, T. J. *et al.* Continuous-wave lasing in cesium lead bromide perovskite nanowires. *Advanced Optical Materials* **6,** 1700982 (2018).
161. Takazawa, K., Inoue, J.-i., Mitsuishi, K. & Takamasu, T. Fraction of a Millimeter Propagation of Exciton Polaritons in Photoexcited Nanofibers of Organic Dye. *Physical Review Letters* **105,** 067401 (2010).
162. Van Vugt, L. K. *et al.* Exciton Polaritons Confined in a ZnO Nanowire Cavity. *Physical Review Letters* **97,** 147401 (2006).
163. Pandya, R. *et al.* Microcavity-Like Exciton-Polaritons Can Be the Primary Photoexcitation in Bare Organic Semiconductors. *Nature Communications* **12,** 1–11 (2021).
164. Platts, C. E. *et al.* Whispering-gallery exciton polaritons in submicron spheres. *Physical Review B* **79,** 245322. ISSN: 10980121 (2009).
165. Verre, R. *et al.* Transition metal dichalcogenide nanodisks as high-index dielectric Mie nanoresonators. *Nature Nanotechnology* **14,** 679–684 (2019).
166. Ling, H., Nourbakhsh, M., Whiteside, V. R., Tischler, J. G. & Davoyan, A. R. Near-unity light-matter interaction in mid-infrared van der Waals nanocavities. *arXiv preprint arXiv:2308.16492* (2023).
167. Gil, B., Cassabois, G., Cusco, R., Fugallo, G. & Artus, L. Boron nitride for excitonics, nano photonics, and quantum technologies. *Nanophotonics* **9,** 3483–3504 (2020).

168. Bernath, P. F. *Spectra of atoms and molecules* (Oxford university press, 2020).
169. Pritchard, J. N., Hatley, R. H., Denyer, J. & Hollen, D. v. Mesh nebulizers have become the first choice for new nebulized pharmaceutical drug developments. *Therapeutic Delivery* **9,** 121–136 (2018).
170. Sharma, P., Quazi, M., Vazquez, I. R. & Jackson, N. Investigation of droplet size distribution for vibrating mesh atomizers. *Journal of Aerosol Science* **166,** 106072 (2022).
171. Arnott, W. P., Schmitt, C., Liu, Y. W. & Hallett, J. Droplet Size Spectra and Water-Vapor Concentration of Laboratory Water Clouds: Inversion of Fourier Transform Infrared (500–5000 cm^{-1}) Optical-Depth Measurement. *Applied Optics* **36,** 5205–5216 (1997).
172. Muhammad, S. S., Flecker, B., Leitgeb, E. & Gebhart, M. Characterization of fog attenuation in terrestrial free space optical links. *Optical Engineering* **46,** 066001 (2007).
173. Tampieri, F. & Tomasi, C. Size distribution models of fog and cloud droplets in terms of the modified gamma function. *Tellus* **28,** 333–347 (1976).
174. Benayahu, Y., Ben-David, A., Fastig, S. & Cohen, A. Cloud-Droplet-Size Distribution From Lidar Multiple-Scattering Measurements. *Applied Optics,* 1569–1578 (1995).
175. Lather, J. & George, J. Improving Enzyme Catalytic Efficiency by Co-operative Vibrational Strong Coupling of Water. *The Journal of Physical Chemistry Letters* **12,** 379–384 (2020).
176. Imperatore, M. V., Asbury, J. B. & Giebink, N. C. Reproducibility of cavity-enhanced chemical reaction rates in the vibrational strong coupling regime. *The Journal of Chemical Physics* **154,** 191103 (2021).
177. Vergauwe, R. M. *et al.* Modification of enzyme activity by vibrational strong coupling of water. *Angewandte Chemie International Edition* **58,** 15324–15328 (2019).
178. Li, T. E., Subotnik, J. E. & Nitzan, A. Cavity molecular dynamics simulations of liquid water under vibrational ultrastrong coupling. *Proceedings of the National Academy of Sciences* **117,** 18324–18331 (2020).
179. Garcia-Vidal, F. J., Ciuti, C. & Ebbesen, T. W. Manipulating matter by strong coupling to vacuum fields. *Science* **373,** eabd0336 (2021).

180. Berghuis, A. M. *et al.* Controlling exciton propagation in organic crystals through strong coupling to plasmonic nanoparticle arrays. *ACS Photonics* **9,** 2263–2272 (2022).
181. Pandya, R. *et al.* Tuning the Coherent Propagation of Organic Exciton-Polaritons through Dark State Delocalization. *Advanced Science* **9,** 2105569 (2022).
182. Balasubrahmaniyam, M. *et al.* From enhanced diffusion to ultrafast ballistic motion of hybrid light–matter excitations. *Nature Materials* **22,** 338–344 (2023).
183. Feist, J. & Garcia-Vidal, F. J. Extraordinary exciton conductance induced by strong coupling. *Physical Review Letter* **114,** 196402 (2015).
184. Schachenmayer, J., Genes, C., Tignone, E. & Pupillo, G. Cavity-enhanced transport of excitons. *Physical Review Letter* **114,** 196403 (2015).
185. Orgiu, E. *et al.* Conductivity in organic semiconductors hybridized with the vacuum field. *Nat. Mater.* **14,** 1123–1129 (2015).
186. Kowalewski, M., Bennett, K. & Mukamel, S. Cavity femtochemistry: Manipulating nonadiabatic dynamics at avoided crossings. *The Journal of Physical Chemistry Letters* **7,** 2050–2054 (2016).
187. Thomas, A. *et al.* Tilting a ground-state reactivity landscape by vibrational strong coupling. *Science* **363,** 615–619 (2019).
188. Ahn, W., Triana, J. F., Recabal, F., Herrera, F. & Simpkins, B. S. Modification of ground-state chemical reactivity via light–matter coherence in infrared cavities. *Science* **380,** 1165–1168 (2023).
189. Kasprzak, J. *et al.* Bose–Einstein condensation of exciton polaritons. *Nature* **443,** 409–414 (2006).
190. Georgiou, K., Jayaprakash, R., Othonos, A. & Lidzey, D. G. Ultralong-Range Polariton-Assisted Energy Transfer in Organic Microcavities. *Angewandte Chemie* **133,** 16797–16803 (2021).
191. Dirnberger, F. *et al.* Magneto-optics in a van der Waals magnet tuned by self-hybridized polaritons. *Nature* **620,** 533–537 (2023).
192. Vurgaftman, I., Simpkins, B. S., Dunkelberger, A. D. & Owrutsky, J. C. Comparative analysis of polaritons in bulk, dielectric slabs, and planar cavities with implications for cavity-modified reactivity. *The Journal of Chemical Physics* **156** (2022).
193. Menghrajani, K. S. & Barnes, W. L. Strong coupling beyond the light-line. *ACS Photonics* **7,** 2448–2459 (2020).

194. Thomas, P. A., Tan, W. J., Kravets, V. G., Grigorenko, A. N. & Barnes, W. L. Non-polaritonic effects in cavity-modified photochemistry. *arXiv preprint arXiv:2306.05506* (2023).
195. Menghrajani, K. S., Vasista, A. B., Tan, W. J. & Barnes, W. L. Molecular strong coupling: an exploration employing open, half-and full planar cavities. *arXiv preprint arXiv:2211.08300* (2022).
196. Sauvan, C., Wu, T., Zarouf, R., Muljarov, E. A. & Lalanne, P. Normalization, orthogonality, and completeness of quasinormal modes of open systems: the case of electromagnetism. *Optics Express* **30,** 6846–6885 (2022).
197. Bai, Q., Perrin, M., Sauvan, C., Hugonin, J.-P. & Lalanne, P. Efficient and intuitive method for the analysis of light scattering by a resonant nanostructure. *Optics Express* **21,** 27371–27382 (2013).
198. Hecht, E. & Zajac, A. *Optics* (Addison Wesley San Francisco, 2002).
199. Castellanos-Gomez, A. *et al.* Deterministic transfer of two-dimensional materials by all-dry viscoelastic stamping. *2D Materials* **1,** 011002 (2014).
200. Munkhbat, B., Küçüköz, B., Baranov, D. G., Antosiewicz, T. J. & Shegai, T. O. Nanostructured transition metal dichalcogenide multilayers for advanced nanophotonics. *Laser & Photonics Reviews* **17,** 2200057 (2023).
201. Shegai, T., Brian, B., Miljkovic, V. D. & Käll, M. Angular distribution of surface-enhanced Raman scattering from individual Au nanoparticle aggregates. *ACS Nano* **5,** 2036–2041 (2011).
202. Lieb, M. A., Zavislan, J. M. & Novotny, L. Single-molecule orientations determined by direct emission pattern imaging. *Journal of the Optical Society of America B* **21,** 1210 (2004).
203. Lettieri, T. R., Jenkins, W. D. & Swyt, D. A. Sizing of individual optically levitated evaporating droplets by measurement of resonances in the polarization ratio. *Applied Optics* **20,** 2799–2805 (1981).